

**DOE-ER-0313/36
Distribution
Categories
UC-423, -424**

**FUSION MATERIALS
SEMIANNUAL PROGRESS REPORT
FOR THE PERIOD ENDING
June 30, 2004**

**Prepared for
DOE Office of Fusion Energy Sciences
(AT 60 20 10 0)**

DATE PUBLISHED: SEPTEMBER 2004

**Prepared for
OAK RIDGE NATIONAL LABORATORY
Oak Ridge, Tennessee 37831
Managed by
UT-Battelle, LLC
For the
U.S. DEPARTMENT OF ENERGY**

FOREWORD

This is the thirty-sixth in a series of semiannual technical progress reports on fusion materials science activities supported by the Fusion Energy Sciences Program of the U.S. Department of Energy. This report focuses on research addressing the effects on materials properties and performance from exposure to the neutronic, thermal, and chemical environments anticipated in the chambers of fusion experiments and energy systems. This research is a major element of the national effort to establish the materials knowledge base of an economically and environmentally attractive fusion energy source. Research activities on issues related to the interaction of materials with plasmas are reported separately.

The results reported are the product of a national effort involving a number of national laboratories and universities. A large fraction of this work, particularly in relation to fission reactor irradiations, is carried out collaboratively with partners in Japan, Russia, and the European Union. The purpose of this series of reports is to provide a working technical record for the use of program participants, and to provide a means of communicating the efforts of fusion materials scientists to the broader fusion community, both nationally and worldwide.

This report has been compiled and edited under the guidance of R. L. Klueh and Teresa Roe, Oak Ridge National Laboratory. Their efforts, and the efforts of the many persons who made technical contributions, are gratefully acknowledged.

G. R. Nardella
Research Division
Office of Fusion Energy Sciences

TABLE OF CONTENTS

1.0	VANADIUM ALLOYS	1
1.1	FURTHER MICROSTRUCTURAL EXAMINATIONS OF V-4Cr-4Ti PRESSURIZED CREEP TUBES —D. S. Gelles and R. J. Kurtz (Pacific Northwest National Laboratory)	2
	Pressurized thermal creep tubes of V-4Cr-4Ti have been examined following testing in the range 650 to 800°C for tests lasting $\sim 10^4$ h. Creep deformation was found to be controlled by climb-controlled dislocation glide at all temperatures below 800°C whereas at 800°C, sub-grain boundary structure predominated and represented the main obstacle for dislocation motion. At 650 and 700°C after $\sim 10^4$ h an increased density of (Ti,V) oxy-carbo-nitride precipitates near the outer surface extending inwards a distance of 30 and 70 μm , respectively, was found. At 800°C, enhanced (Ti,V) oxy-carbo-nitride precipitation was observed across the entire tube wall thickness and may have affected creep response. Also, evidence for internal precipitation associated with the dislocation structure could be identified. The discussion section addresses differences in the controlling creep mechanisms between grain boundary sliding, sub-grain boundary controlled dislocation climb and individual dislocation climb processes.	
1.2	ROOM TEMPERATURE COMPRESSION PROPERTIES OF TWO HEATS OF UNIRRADIATED V-4Cr-4Ti —M. B. Toloczko (Pacific Northwest National Laboratory) and R. J. Kurtz (Pacific Northwest National Laboratory)	13
	Cylindrical specimens fabricated from Heat 832665 (US Heat) of V-4Cr-4Ti and from Heat P8013 (NIFS-2 Heat) of V-4Cr-4Ti were tested in compression at room temperature on a screw-driven test frame. The average value of the yield strength was 344 MPa for the US Heat and 315 MPa for the NIFS-2 Heat. The average strain hardening exponent calculated from the first few percent of plastic strain was about 0.17 for both the US Heat and the NIFS-2 heat. As is common in a compression test, the specimens barreled somewhat during the tests.	
2.0	CERAMIC COMPOSITE MATERIALS	19
2.1	CHARACTERIZATION OF SILICON CARBIDE COMPOSITES PRODUCED BY POLYMER-IMPREGNATION AND HIGH TEMPERATURE PYROLYSIS PROCESS —Y. Katoh and T. Nozawa (Oak Ridge National Laboratory), K. Ozawa and A. Kohyama (Kyoto University)	20
	Near-stoichiometric SiC fiber composites with polymer-derived high-crystallinity SiC matrices were produced and were characterized their microstructures and mechanical properties. The material was produced through repeated polymer-impregnation and pyrolysis (PIP) cycles of Tyranno™-SA sintered SiC fibers, following pyrolytic carbon and SiC bi-layer interphase deposition. Co-polymer of polycarbosilane (PCS) and polymethylsilane (PMS) was used as the precursor for near-stoichiometric SiC matrix. The final heat treatment was performed at 1100 – 1800°C in flowing commercial-purity argon. The produced composites were dense in general with small macro-porosity. Transmission electron microscopy revealed that the matrix microstructures after heat treatment at $>1500^\circ\text{C}$ consisted of fine layers of SiC crystallites in amorphous SiC and carbon matrix. High temperature heat treatment promoted crystallization at the expense of porosity. No degradation of Tyranno-SA fiber was identified after heat treatment at 1800°C. PIP-composites with well-crystallized SiC matrices exhibited flexural fracture behavior very similar to that of chemically vapor infiltrated composites. The composites maintained ambient temperature strength up to 1000°C in air and to 1300°C in argon.	

2.2 A NEW APPROACH TO JOINING SiC/SiC COMPOSITES—C. H. Henager, Jr. (Pacific Northwest National Laboratory) 27

A new approach to joining SiC-based ceramics is described and evaluated for Fusion Energy systems. The joining method is based on pre-ceramic polymers filled with reactive and inert filler powders and is similar to other approaches that use such materials. This approach differs in the particular polymer system and in the details of the processing. A principal advantage of this approach relative to other, similar approaches is that the polymer system is easily handled in ambient air and can be processed in air. This makes the joining process simple and field repairable. The joining compound is a liquid that can be painted, sprayed, or applied by dip coating.

2.3 STRENGTH AND ELASTIC MODULUS OF NEUTRON-IRRADIATED CUBIC SILICON CARBIDE—Y. Katoh and L. L. Snead (Oak Ridge National Laboratory) 33

Mechanical properties of high purity polycrystalline cubic silicon carbide were characterized after neutron irradiation. The materials were irradiated in target position capsules in High Flux Isotope Reactor to nominal neutron fluence levels of up to 7.7 dpa at temperatures of 300, 500 and 800°C. Reduction in Young's modulus was observed after irradiation, and its irradiation temperature dependence agreed qualitatively with calculated modulus change due to point defect swelling. Irradiation caused very significant modification of statistical flexural strength but caused only minor increase in nano-indentation hardness. It was pointed out that the irradiation effect on fracture initiation through an enhanced cleavage resistance in large grains could be contributing to the major change in flexural strength properties.

2.4 MODELING THE TRANSVERSE THERMAL CONDUCTIVITY OF 3D-SiC_f/SiC COMPOSITES—G. E. Youngblood and R. H. Jones (Pacific Northwest National Laboratory) and Reiji Yamada (JAERI, Tokai-mura, JP) 44

Our previously developed hierarchical two-layer (H2L) model was modified to describe the effective transverse thermal conductivity (K_{eff}) of a three-dimensional (3D) SiC/SiC composite plate made with cross-layered and Z-stitched X:Y:Z uniaxial fiber tow sub-units. As before, the model describes K_{eff} in terms of constituent, microstructural and architectural properties that include the expected effects of fiber-matrix interfacial conductance, of high fiber packing fractions within individual tow sub-units and of the non-uniform porosity contents, shapes and orientations within these sub-units. Model predictions were obtained for two versions of a 3D-Tyranno SA™/PyC/ICVI-SiC composite that had similar fiber/matrix pyrocarbon (PyC) interfaces, relatively high bulk densities (~2.88 g/cc), and an X:Y configuration with fiber content ratios 1:1. The only major difference between the two versions was their Z-stitch fiber content where the relative fiber ratios were 0.1 and 1.2 in the Z sub-units.

2.5 FAST FRACTURE STRENGTH OF THIN PYROLYTIC CARBON INTERPHASE SILICON CARBIDE COMPOSITES—Y. Katoh, T. Nozawa, and L. L. Snead (Oak Ridge National Laboratory), T. Hinoki and A. Kohyama (Kyoto University, Japan), and W. Yang (National Institute for Materials Science, Japan) 52

The applicability of very thin pyrolytic carbon (PyC) interphase between fibers and matrices in silicon carbide (SiC) fiber-reinforced, chemically vapor-infiltrated SiC matrix composites was studied based on investigations on the effect of interphase thickness on fast fracture properties. It appears that the mechanical properties of near-stoichiometric high-crystallinity SiC fiber composites are not subject to strong interphase thickness

effect, which has been reported for non-stoichiometric SiC fiber composites. This difference was discussed from the viewpoints of thermal residual stress, process-induced damages, fiber surface features, and interfacial bonding and friction. A preliminary conclusion is drawn that a thin PyC interphase, as low as ~25nm, will be generally beneficial for both fast fracture and lifetime limiting properties in stoichiometric SiC-based composites.

3.0 FERRITIC/MARTENSITIC STEELS AND ODS STEELS 58

3.1 OXIDE DISPERSION-STRENGTHENED STEELS: A COMPARISON OF EXPERIMENTAL AND COMMERCIAL STEELS—R. L. Klueh, J. P. Shingledecker, R. W. Swindeman, and D. T. Hoelzer (Oak Ridge National Laboratory) 59

Oxide dispersion-strengthened (ODS) steels are being developed and investigated for nuclear fission and nuclear fusion applications in Japan, Europe, and the United States. In addition, commercial ODS products are available and have been used in niche applications. Microstructural and mechanical properties studies have been conducted at Oak Ridge National Laboratory and elsewhere on various commercial and experimental ODS steels. Tensile and creep properties have been obtained and collected from literature and commercial sources. These data are compared to show the differences and similarities of different ODS steels, and observations are explained in terms of the microstructures of the steels.

4.0 COPPER ALLOYS 72

No contributions

5.0 REFRACTORY METALS AND ALLOYS 73

No contributions

6.0 AUSTENITIC STAINLESS STEELS 74

No contributions

7.0 MHD INSULATORS, INSULATING CERAMICS, AND OPTICAL MATERIALS 75

7.1 STUDY OF THE LONG-TERM STABILITY OF MULTI-LAYER MHD COATINGS FOR FUSION REACTOR APPLICATIONS—B. A. Pint, P. F. Tortorelli, L. D. Chitwood, and H. M. Meyer (Oak Ridge National Laboratory, USA) and M. Fujiwara (Tohoku University, Japan) 76

Static lithium compatibility tests have been conducted on vanadium alloys at 800°C. Mass gains have been detected that are not consistent with prior static Li exposures of unalloyed vanadium and are difficult to interpret based on the impurity levels in the lithium specified by the manufacturer. A second test gave more reasonable results. Some of the mass gain could be attributed to N and C uptake from the Li but this should be countered by O loss from the alloy. Post exposure analysis of the specimens indicated a surface layer rich in O, C and Ca but no indication for the embrittlement observed.

- 7.2 EVALUATION OF THE CHEMICAL COMPATIBILITY OF Y_2O_3 AS AN ELECTRICALLY INSULATING COATING FOR A LIQUID LITHIUM BLANKET**—P. F. Tortorelli, B. A. Pint, and T. M. Besmann (Oak Ridge National Laboratory, USA) **81**
- Modeling of the chemical stability of Y_2O_3 in molten lithium was hampered by the lack of available thermochemical data for mixed oxides of Li-Y and Ti-Y. Nevertheless, this evaluation indicated that Y_2O_3 was not stable in a lithium environment at 600-1000°C. Furthermore, the results indicated that the experimental observations of Y-Ti oxides on Y_2O_3 after exposure to molten lithium in V-4Ti-4Cr capsules was likely due to formation of Li_2TiO_3 and $LiYO_2$.
- 7.3 HIGH DOSE NEUTRON IRRADIATION OF $MgAl_2O_4$ SPINEL: EFFECTS OF POST-IRRADIATION THERMAL ANNEALING ON EPR AND OPTICAL ABSORPTION**—A. Ibarra (CIEMAT. Inst. Investigación Básica), D. Bravo (Universidad Autonoma de Madrid), F. J. Lopez (Universidad Autonoma de Madrid), and F. A. Garner (Pacific Northwest National Laboratory) **84**
- Electron paramagnetic resonance (EPR) and optical absorption spectra were measured during thermal annealing for stoichiometric $MgAl_2O_4$ spinel that was previously irradiated in FFTF-MOTA at ~405°C to ~50 dpa. Both F and F+ centers are to persist up to very high temperatures (over 700°C), suggesting the operation of an annealing mechanism based on evaporation from extended defects. Using X-ray irradiation following the different annealing steps it was shown that the optical absorption band is related to a sharp EPR band at $g=2.0005$ and that the defect causing these effects is the F+ center.
- 8.0 BREEDING MATERIALS** **92**
- No contributions*
- 9.0 RADIATION EFFECTS, MECHANISTIC STUDIES, AND EXPERIMENTAL METHOD** **93**
- 9.1 MULTISCALE MODELING OF DEFECT GENERATION AND EVOLUTION IN METALLIC ALLOYS FOR FUSION POWER**—Jörg Rottler, David J. Srolovitz, and Roberto Car (Princeton Institute for the Science and Technology of Materials, Princeton University) **94**
- We perform an analysis of the time evolution of self-interstitial atom and vacancy (point defect) populations in pure bcc metals under constant irradiation flux conditions. Mean-field rate equations are developed in parallel to a kinetic Monte Carlo (kMC) model. When only considering the elementary processes of defect production, defect migration, recombination and absorption at sinks, the kMC model and rate equations are shown to be equivalent and the time evolution of the point defect populations is analyzed using simple scaling arguments. We show that the typically large mismatch of the rates of interstitial and vacancy migration in bcc metals can lead to a vacancy population that grows as the square root of time. The vacancy cluster size distribution under both irreversible and reversible attachment can be described by a simple exponential function. We also consider the effect of highly mobile interstitial clusters and apply the model with parameters appropriate for vanadium and iron.
- 9.2 IN-SITU TEM STUDY ON THE COLLAPSE PROCESS OF SFT DURING PLASTIC DEFORMATION**—Y. Matsukawa, Yu. N. Osetsky, R. E. Stoller, and S. J. Zinkle (Oak Ridge National Laboratory) **98**

Dynamic observation of the collapse process of SFTs during plastic deformation in quenched gold was carried out using a TEM. SFTs having perfect pyramid structure were

collapsed by direct interaction with gliding screw dislocations. Although Wirth et al. pointed out that truncation of SFT before interaction with gliding dislocations was an important factor for the SFT collapse [1], the present experimental results clearly showed that truncation of SFT was not a crucial factor for the collapse mechanism. An SFT collapsed in a unique way: only the base portion divided by the gliding plane of dislocation annihilated, while the apex portion remained intact. Judging from the fact that similar collapse process was observed in recent computer simulations using molecular dynamics codes [2], this collapse process is a major one. However, it is still unclear whether this is only one process for SFT collapse, because this collapse process leaves a small SFT as a remnant, whereas SFTs are completely swept out in the dislocation channels actually observed in the deformation microstructure of irradiated fcc metals [3-12]. Further research works will be required for fully understanding of dislocation channeling, which is believed to be a key for ductility reduction of irradiated metals [3].

9.3 VOID HARDENING IN BCC-IRON STUDIED BY ATOMIC-SCALE MODELLING—S. I. Golubov, Yu. N. Osetsky, and R. E. Stoller (Oak Ridge National Laboratory) 108

Atomic-scale modelling permits detailed simulation of the interactions between moving dislocations and particular obstacles. Such simulations should be of large enough scale to simulate a realistic dislocation density and obstacle spacing, and correctly treat long-range self-interaction between dislocation segments. Results obtained with a 2 nm void and two different atomic-scale techniques based on (1) a periodic array of dislocations (PAD) and (2) Green's function boundary conditions (GF) in α -Fe are presented. Static, zero temperature, simulations have been carried out with incrementally increasing strain until dislocation overcomes the obstacle. It is concluded that both techniques reproduce the same critical resolved shear stress (CRSS), and similar void and dislocation modifications are observed.

9.4 THE INTERACTION OF HELIUM ATOMS WITH EDGE DISLOCATIONS IN α -Fe—H. L. Heinisch, F. Gao, and R. J. Kurtz (Pacific Northwest National Laboratory) 112

Formation energies, binding energies, and the migration of interstitial He atoms at and near the center of an $a/2\langle 111 \rangle\{110\}$ edge dislocation in α -Fe are determined using molecular dynamics and conjugate gradient relaxation methods. Results are compared as a function of the distance of the interstitial He atoms from the center of the dislocation and the amount of excess volume around the dislocation. Interstitial He atoms have negative binding energy on the compression side of the dislocation and strong positive binding energy on the tension side. Even at low temperatures, interstitial He atoms in the vicinity of the dislocation easily migrate to positions near the center of the dislocation, where they form crowdion interstitials with binding energies in excess of 2 eV.

10.0 DOSIMETRY, DAMAGE PARAMETERS, AND ACTIVATION CALCULATIONS 117

No contributions

11.0 MATERIALS ENGINEERING AND DESIGN REQUIREMENTS 118

No contributions

- 12.0 IRRADIATION FACILITIES AND TEST MATRICES 119**
- 12.1 IRRADIATION START OF MFE-RB-17J EXPERIMENT—D. K. Felde, A. L. Qualls, K. R. Thoms, D. W. Heatherly, R. G. Sitterson, and R. L. Wallace (Oak Ridge National Laboratory) 120**
- The 17J experiment was installed in a europium-shielded RB* position of HFIR and irradiation began with cycle 400 on April 27, 2004. The capsule temperatures were maintained near the target values with the exception of the lower capsule. An apparent temperature-dependent blockage of the purge gas line limited operation of the lower capsule to ~ 425°C.
- 12.2 ASSEMBLY OF THE US-JAPAN JP-27 EXPERIMENT AND START OF IRRADIATION IN THE HFIR—D. K. Felde, K. R. Thoms, D. W. Heatherly, S. H. Kim, R. G. Sitterson, and R. E. Stoller (Oak Ridge National Laboratory) and H. Tanigawa (Japan Atomic Energy Research Institute, Tokai, Japan) 124**
- Specimen and capsule parts fabrication for JP-27 was completed. Loading of specimens into specimen holders and assembly of the capsule was completed. The experiment was installed in the target region of HFIR and irradiation began with cycle 400, starting April 27, 2004.

1.0 VANADIUM ALLOYS

FURTHER MICROSTRUCTURAL EXAMINATIONS OF V-4Cr-4Ti PRESSURIZED CREEP TUBES—

D. S. Gelles and R. J. Kurtz (Pacific Northwest National Laboratory)*

OBJECTIVE

The objective of this effort is to perform microstructural examinations of creep tubes to determine the deformation processes controlling thermal creep in vanadium alloys for comparison with creep response under irradiation.

SUMMARY

Pressurized thermal creep tubes of V-4Cr-4Ti have been examined following testing in the range 650 to 800°C for tests lasting $\sim 10^4$ h. Creep deformation was found to be controlled by climb-controlled dislocation glide at all temperatures below 800°C whereas at 800°C, sub-grain boundary structure predominated and represented the main obstacle for dislocation motion. At 650 and 700°C after $\sim 10^4$ h an increased density of (Ti,V) oxy-carbo-nitride precipitates near the outer surface extending inwards a distance of 30 and 70 μm , respectively, was found. At 800°C, enhanced (Ti,V) oxy-carbo-nitride precipitation was observed across the entire tube wall thickness and may have affected creep response. Also, evidence for internal precipitation associated with the dislocation structure could be identified. The discussion section addresses differences in the controlling creep mechanisms between grain boundary sliding, sub-grain boundary controlled dislocation climb and individual dislocation climb processes.

PROGRESS AND STATUS

Introduction

A series of pressurized V-4Cr-4Ti creep tubes have been tested under vacuum over the temperature range 650 to 800°C, [1-2] and selected failed specimens from those tests have previously been examined in order to identify operating creep and failure mechanisms [3-4]. It is now possible to examine specimens that have undergone testing up to $\sim 10^4$ hrs. This report provides microstructural examinations for tube specimens tested at 650°C to 200 and 250 MPa, at 700°C to 125 MPa, at 725°C to 150 MPa and at 800°C to 50 MPa.

Experimental Procedure

Specimens selected for examination are listed in Table 1. Detailed information on specimen preparation and testing procedures were reported previously [1,2]. Three of the tubes failed during testing, and therefore, the applied stress was removed while at temperature. The vacuum furnace was shut down immediately upon detecting a tube failure so the time at temperature in the unstressed condition was minimal. Two tubes did not fail and were allowed to cool while still under pressure.

Optical metallography was performed on all specimens using Murakami's etch (10 g. $\text{K}_3\text{Fe}(\text{CN})_6$, 10 g NaOH, 100 ml H_2O for ~ 10 sec). Specimen preparation for transmission electron microscopy (TEM) used standard punching, grinding and electropolishing procedures as described previously [4]. The punch was designed for tubular specimens with a radius of curvature of ~ 2.5 mm. Microscopy was performed on a Technai 30 TEM operating at 300 keV with the imaging procedures employed to provide Burgers vector anisotropy information [5]. Information on the direction of the principal stresses was retained during specimen preparation and examination.

*Pacific Northwest National Laboratory (PNNL) is operated for the U.S. Department of Energy by Battelle Memorial Institute under contract DE-AC06-76.

Table 1. Test conditions for specimens examined in this report

Specimen ID	Test temperature (°C)	Midwall effective stress (MPa)	Time to failure (h)	Effective mid-wall strain (%)	Comments on failure
AR02	650	200	10601	8.9	Burst
AR03	650	250	2733	4.4	Small hole
AR13	700	119	9663*	2.3	Did not fail
AR08	725	150	1506	5.0**	Burst
AR20	800	48	6052*	12.7	Did not fail

*Specimen did not fail. The time listed is the total time at temperature.

**Strain measured at 1221 h, since tube deformation associated with burst prevented an accurate strain measurement.

Table 2. Test conditions for specimens examined previously [4]

Specimen ID	Test temperature (°C)	Effective midwall stress (MPa)	Time to failure (h)	Effective mid-wall failure strain (%)
AR14	700	138.9	6667	14.8
AR15	700	158.8	2804	13.0
AR16	800	70.6	4029	51.9
AR17	800	92.6	864	13.6
AR18	800	117.7	578	24.1
AR19	800	136.8	242	14.7

Results

Metallography

Failure in specimens AR02 and AR08 resulted in large distortions so that the opening created by failure was about the size of the tube diameter (and described in Table 1 as a burst). Failure in specimen AR03 was more typical of that found previously in specimens AR14 and AR16 where only a small surface crack could be found [4]. Metallographic examinations revealed no major differences between creep conditions. Figure 1 provides optical metallographic examples of grain structure for different tubes tested at 650, 700 and 800°C. No change in grain size is evident for the different test temperatures.

Examination of the etched specimens demonstrated that the (Ti,V) oxy-carbo-nitride particles were observable and that an effect of the environment during testing could be seen. Examples of the microstructure near the outer surface of each specimen are shown in Fig. 2 with the outer diameter to the right in each case. From these images, a layer of enhanced precipitation extending ~30 µm into specimen AR02 was estimated. The enhanced precipitate layer extended ~70 µm into specimen AR13 and it probably extended all the way through specimen AR20. Therefore, creep tests at 650°C and 700°C were relatively unaffected by the testing environment, but tests at 800°C may have been affected by the environment.

Microscopy

All microstructures showed non-uniform grain structures, non-uniformly distributed coarse precipitation and low-to-moderate dislocation densities. Of concern was evidence in each specimen of dislocation rearrangement after specimen preparation such that near the perforation surface steps could be seen and long straight dislocations were present elsewhere in the microstructures. As a result, dislocation imaging was restricted to thicker areas where effects of dislocation rearrangement were much less evident. None-

the less, it is anticipated that all microstructures reported here have been affected by post-creep deformation.

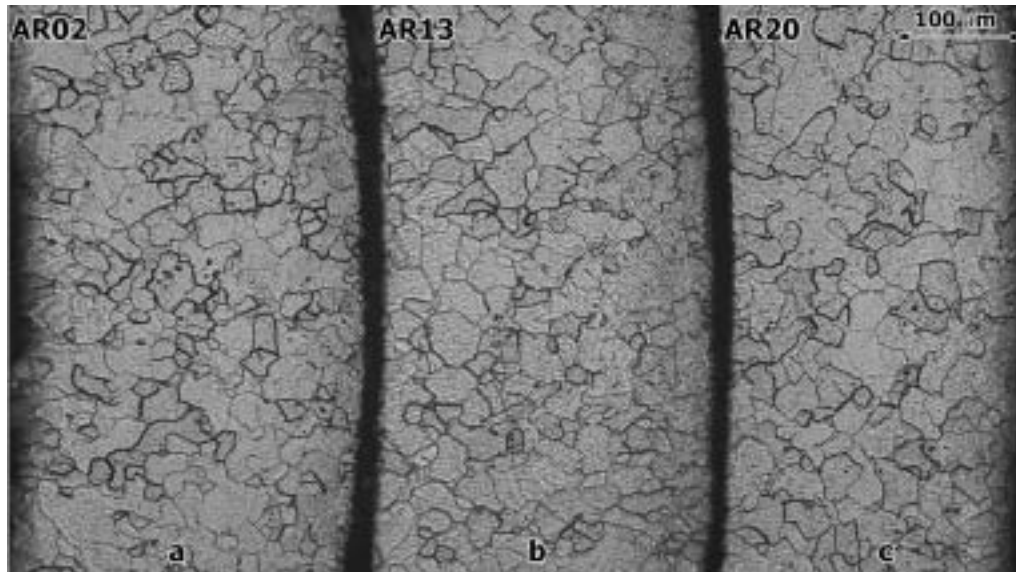


Fig. 1. Optical metallography of pressurized tube specimens a) AR02 tested at 650°C/200 MPa, b) AR13 tested at 700°C/119 MPa, and c) AR20 tested at 800°C/48 MPa.

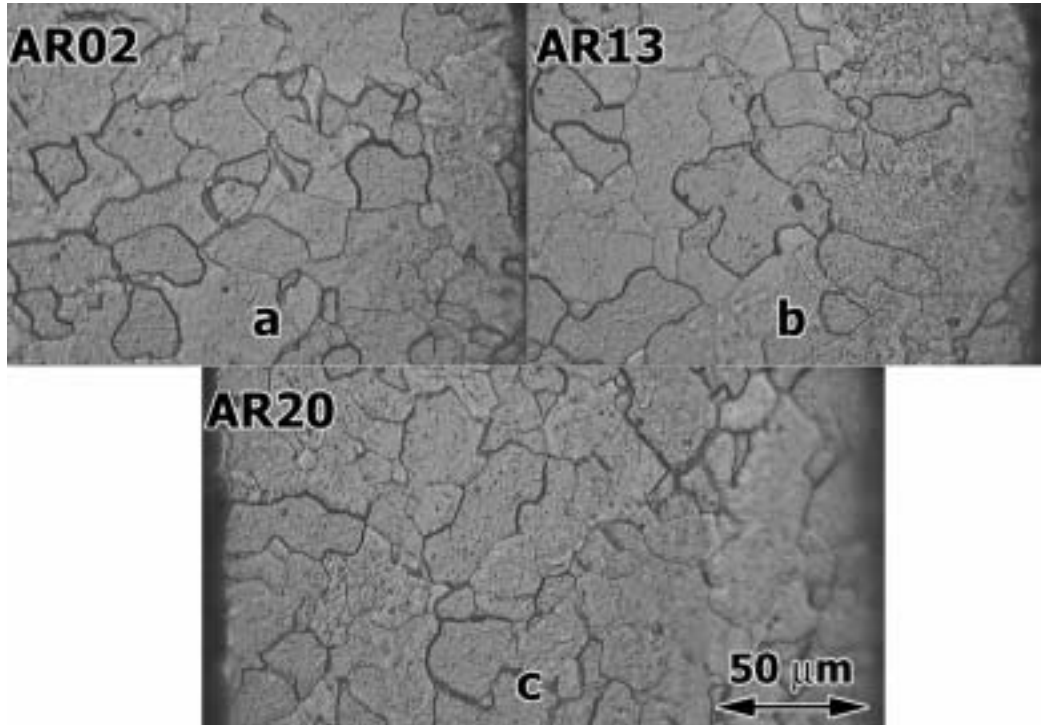


Fig. 2. Higher magnification optical metallography of pressurized tube specimens a) AR02 tested at 650°C/200 MPa, b) AR13 tested at 700°C/119 MPa, and c) AR20 tested at 800°C/48 MPa.

Lower magnification micrographs for the conditions examined are provided in Fig. 3 along with an example of the original tube structure to show dislocation and precipitate structures. Note that Fig. 3c of specimen AR03 is at a higher magnification than the rest. From Fig. 3, it can be demonstrated that moderately high dislocation densities are found for all conditions except AR20, 800°C/48 MPa, (Fig. 3f) where the dislocations tend to be confined to sub-grain boundaries. Precipitation of coarse (Ti,V) oxy-carbo-nitrides is non-uniform, but in the examples given in Fig. 3, the particle sizes are very similar and on the order of $\sim 0.3 \mu\text{m}$. It is apparent that these coarse precipitate particles were present prior to testing and did not change significantly during creep testing. However, Figs. 3c through 3f include examples of grain boundary structures where smaller precipitate particles can be seen and differences in particle size can be found. In fact, for condition AR20, the particles at grain boundaries have grown to about the same size as the rest of the particles. Such smaller particles on grain boundaries were present following the heat treatment of the tubing, [6] and therefore this size range is sensitive to coarsening on a time scale of $\sim 10^4$ hrs in the temperature range 650 to 800°C.

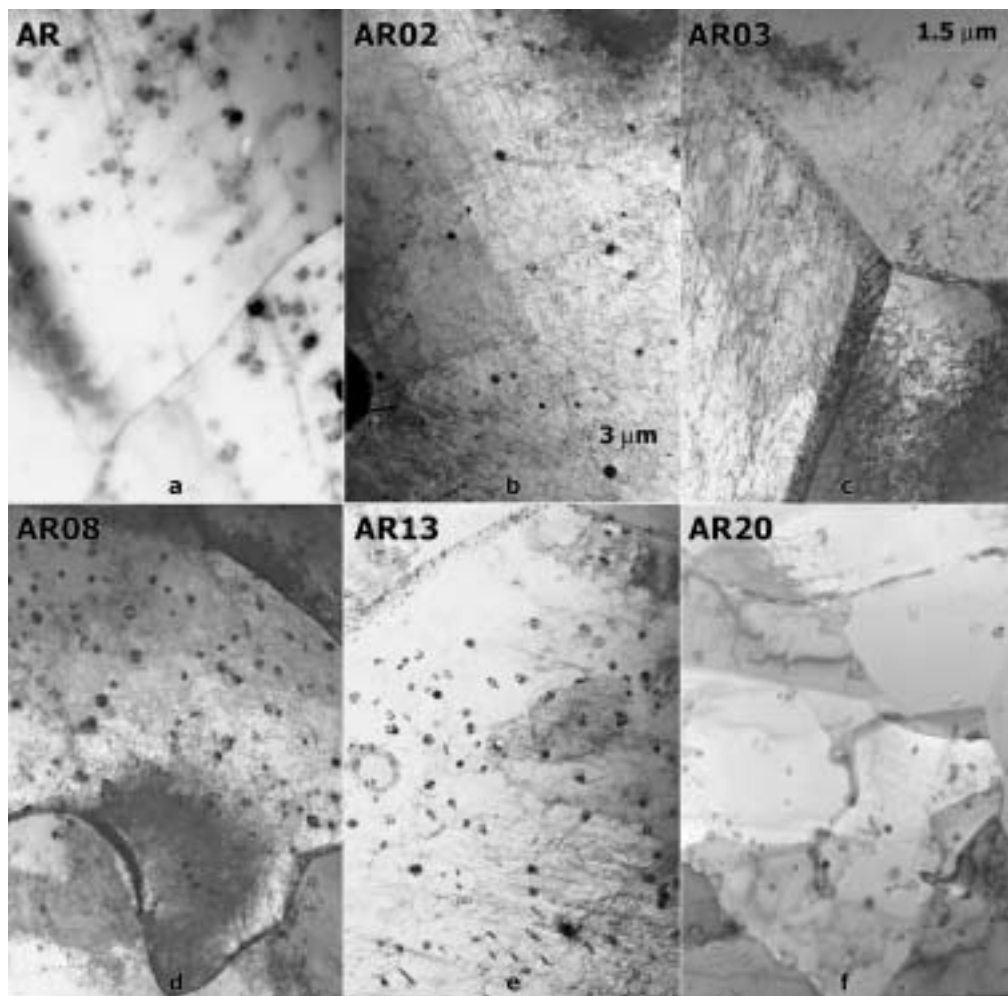


Fig. 3. TEM microstructures of pressurized tube specimens a) as heat treated, b) AR02 tested at 650°C/200 MPa, c) AR03 tested at 650°C/250 MPa, d) AR08 tested at 725°C/150 MPa, e) AR13 tested at 700°C/119 MPa, and f) AR20 tested at 800°C/48 MPa.

Examples of the dislocation structures found in each specimen are given in Figs. 4-8. In each case three views are provided with $\bar{g}=01\bar{1}$ and 200 always and either $\bar{1}10$ or $\bar{1}01$ depending on foil orientation. Also, as noted in reference [5], all $\frac{1}{2}\langle 111 \rangle$ Burgers vectors should be visible in 200 imaging, whereas only

half the possibilities are present in $01\bar{1}$, $\bar{1}10$ or $\bar{1}01$. By comparison of the three images that are provided, it should be possible to identify each of the four Burgers vectors present. Figure 4 gives an example of specimen AR02 tested at 650°C and 200 MPa, revealing a complex dislocation tangle. Two features denoting heterogeneous precipitation can be identified. Below the large precipitate at the upper left is an elongated feature that can only be seen in Figs. 4a and 4c and can be described as a linear precipitate array. Also, throughout the figure are small equiaxed dark features often associated with dislocations. It is anticipated that these are small precipitates that affect creep response.

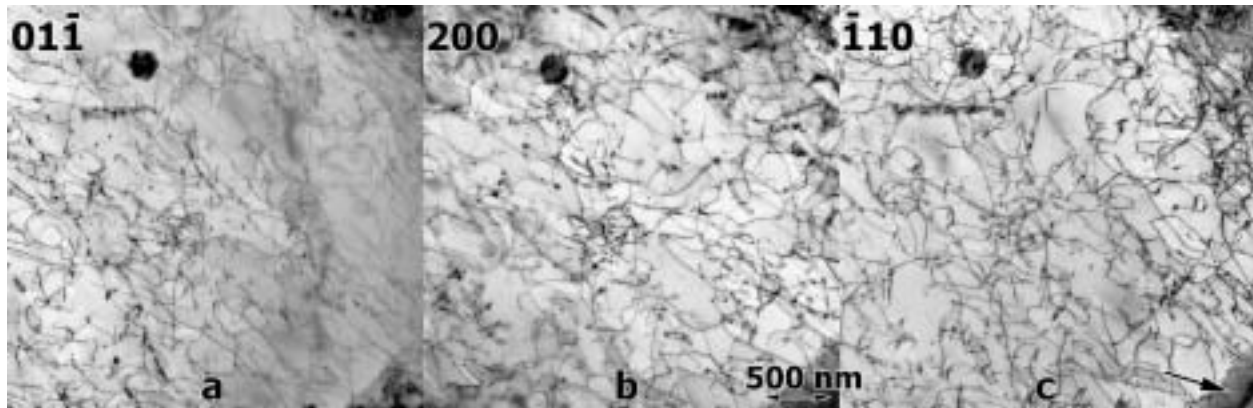


Fig. 4. Dislocation imaging for specimen AR02 ($650^\circ\text{C}/200$ MPa) with $\bar{g}=\bar{1}10$ horizontal in a), $\bar{g}=200$ vertical in b), and $\bar{g}=\bar{1}10$ as indicated in c).

Figure 5 shows similar features in specimen AR03, tested at the same temperature as for AR02, but at higher stress and for a shorter time. In this case more of the planar precipitate arrays can be identified, and the dislocation density is non-uniform, enhanced near larger $0.3\ \mu\text{m}$ precipitate particles.

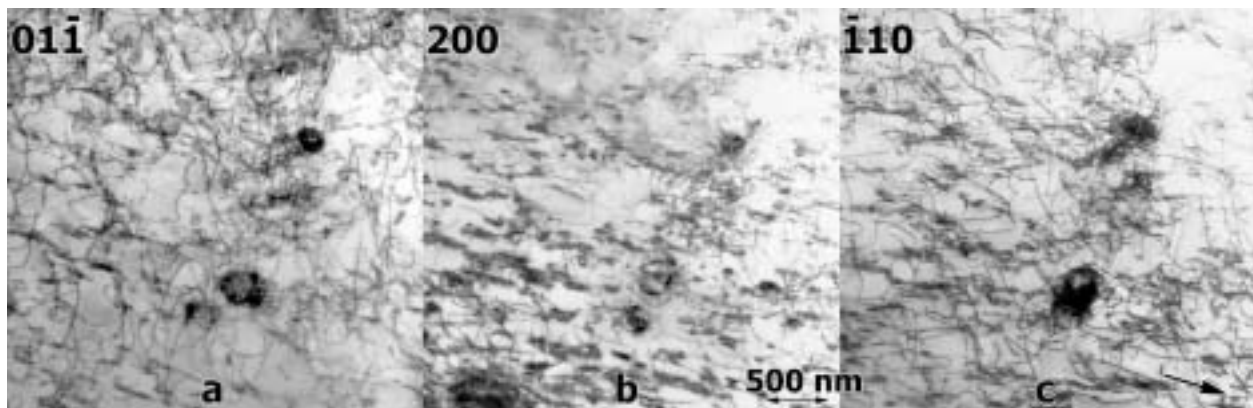


Fig. 5. Dislocation imaging for specimen AR03 ($650^\circ\text{C}/250$ MPa) with $\bar{g}=\bar{1}10$ horizontal in a), $\bar{g}=200$ vertical in b), and $\bar{g}=\bar{1}10$ as indicated in c).

Figure 6 provides similar views of specimen AR13 tested at 700°C . Again, equiaxed fine precipitation can be identified, and the dislocation density is non-uniform. In fact, the dislocation array in the center of each micrograph consists of a network, with only some of the line segments showing in 6a and 6c.

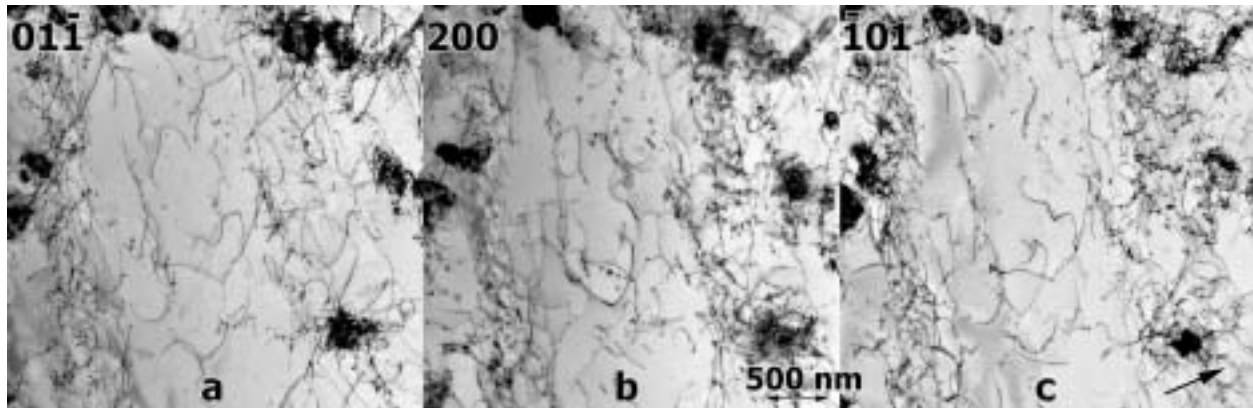


Fig. 6. Dislocation imaging for specimen AR13 (700°C/119 MPa) with $\bar{g}=\bar{1}10$ horizontal in a), $\bar{g}=200$ vertical in b), and $\bar{g}=\bar{1}01$ as indicated in c).

Figure 7 shows specimen AR08 tested at 725°C. Again, fine precipitation is present and examples of coarser precipitation in planar arrays can be identified. A higher density of straight dislocations can be seen in this view, which may be an example of post-creep testing deformation. Note that these straight dislocations running from upper right to lower left are only observable in Figs. 7a and 7b, indicating that they have Burgers vector $\frac{a}{2}[\bar{1}\bar{1}1]$ as can be demonstrated from information in reference [6], and as can be shown are primarily edge in character. As post-creep deformation is expected to leave dislocations of screw character, these longer straight dislocations were probably generated by climb during the creep process.

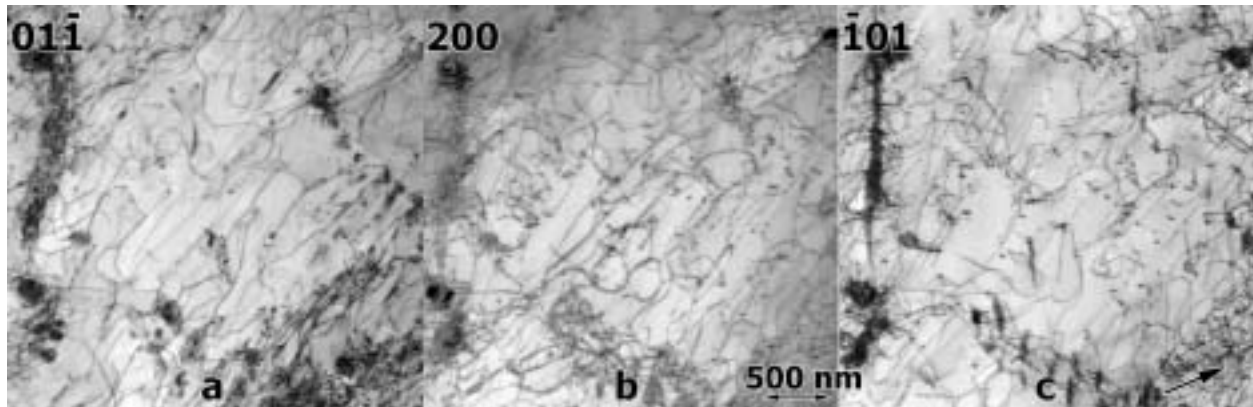


Fig. 7. Dislocation imaging for specimen AR08 (725°C/150 MPa) with $\bar{g}=\bar{1}10$ horizontal in a), $g=200$ vertical in b), and $g=\bar{1}01$ as indicated in c).

Figure 8 shows sub-grain boundary structure in specimen AR20, tested at 800°C. The area is unusual because a small sub-grain about 2 μm in diameter is seen. Most sub-grains are much larger. The upper boundary for this sub-grain is probably a simple array of dislocations of only one Burgers vector and examples can be identified where dislocations in this array are interacting with other dislocations and are being pulled into or out of the sub-grain. Also, an array of dislocations can be seen towards the lower part of the sub-grain that could be an example of post-creep deformation, but in fact, these dislocations form a network, visible in Figs. 8a and c and therefore, the sub-grain is sub-divided. (The fact that this complete network cannot be seen in Fig. 8b either means that the imaging in this area is not really controlled by $\bar{g}=200$ or that a different Burgers vector such as $a[200]$ is present.) Finally, the dislocation arrays typical of sub-grain boundary structure defining the lower right side of the sub-grain (and the one

defining the lower left) are complex arrays with several Burgers vectors present at a high dislocation density. This is indicated by the cross-hatched nature to the boundary imaging. Such boundaries have incorporated many dislocations with at least two Burgers vectors represented as the dislocation structure has relaxed into this lower energy state.

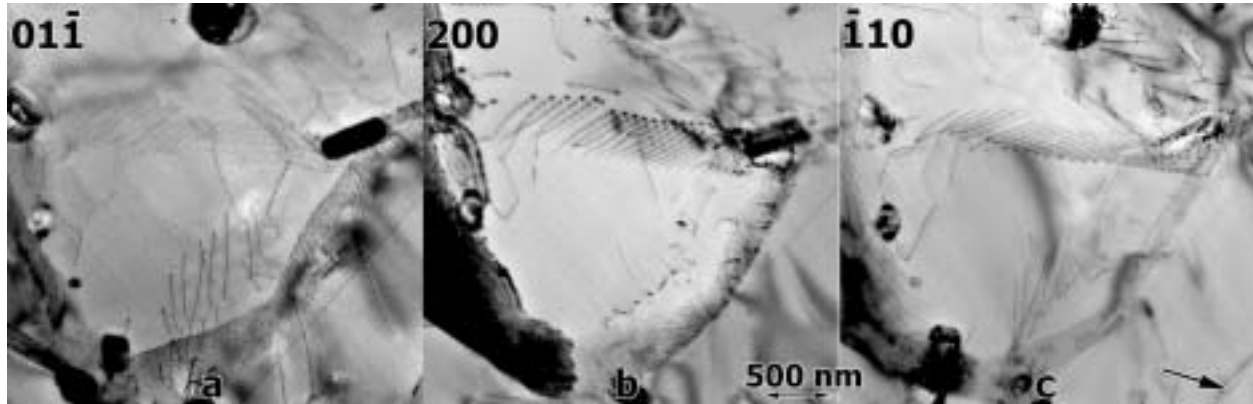


Fig. 8. Dislocation imaging for specimen AR20 (800°C/48 MPa) with $\bar{g}=\bar{1}10$ horizontal in a), $\bar{g}=200$ vertical in b), and $\bar{g}=\bar{1}10$ as indicated in c).

It can be noted that an interesting sub-grain boundary was identified in specimen AR13 tested at 700°C and shown in Fig. 9. The array of dislocations forming the sub-grain boundary happens to be close to a grain boundary on the lower left, but the orientation is almost orthogonal. The dislocation array in the boundary is simple, with one burgers vector predominating. (As the sub-boundary can be seen in both 200 and $\bar{1}01$ views, the Burgers vector should be $\frac{a}{2}[\bar{1}11]$ and of predominantly edge character, similar to the example described for Fig. 7.)

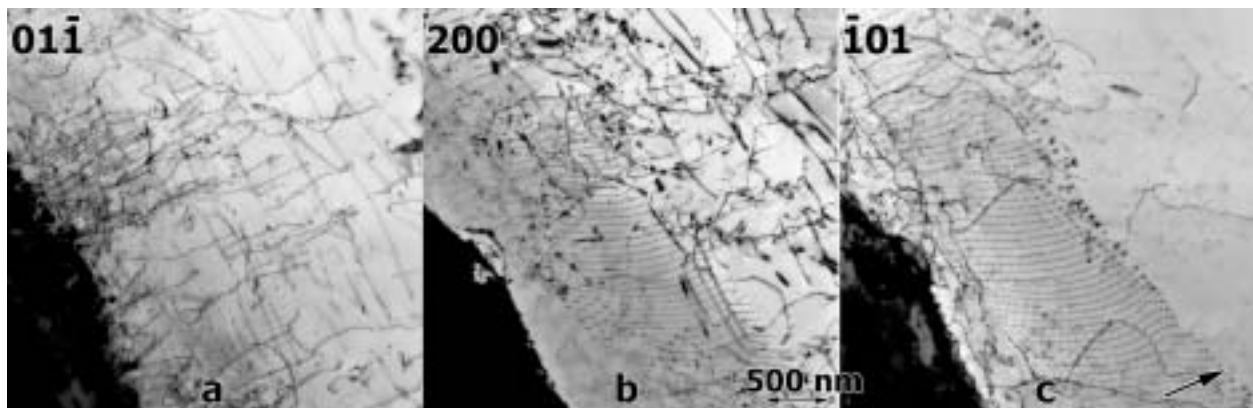


Fig. 9. Dislocation imaging for specimen AR13 showing a sub-grain boundary with $\bar{g}=\bar{1}10$ horizontal in a), $\bar{g}=200$ vertical in b), and $\bar{g}=\bar{1}01$ as indicated in c).

Discussion

The metallographic results shown in Fig. 2 indicate that impurity pickup from the vacuum has produced enhanced precipitation near the surface for tests at 650 and 700°C to $\sim 10^4$ hr. An estimate of the amount of impurity pickup can be obtained from the oxygen and nitrogen partial pressures in the vacuum furnace. Each test specimen was wrapped in Ti foil and the total vacuum pressure was $\leq 10^{-7}$ torr during high-temperature testing. Residual gas analysis at 800°C indicates that the oxygen and nitrogen partial pressures were about 2×10^{-10} torr (2.7×10^{-8} Pa). Pint and DiStefano [7] have developed an oxidation

model for V-4Cr-4Ti that gives the rate of oxygen pickup in mg/cm²h at a given oxygen partial pressure and temperature. Their model is pertinent to the test conditions employed here. The equation fit to their data is:

$$r = 4.7 \times 10^2 e^{-82/T} p(O_2) \quad (1)$$

where $p(O_2)$ is the oxygen partial pressure in Pa and T is the temperature in Kelvin. The surface area of a creep tube is about 3.65 cm² so at a temperature of 650°C the amount of oxygen picked up in ~10⁴ h is 0.19 mg. At 800°C the amount of oxygen picked up is 0.22 mg. In terms of wppm the estimated oxygen pickup ranges from 360 to 415 wppm. Similar estimates of oxygen pickup can be obtained from the flux of oxygen atoms impinging on the surface of the specimen during the course of the experiment. From the kinetic theory of gases the flux of oxygen atoms, J , is:

$$J = \frac{P}{(2\pi mkT)^{1/2}} \quad (2)$$

where P is the oxygen partial pressure, m is the mass of an oxygen atom, k is Boltzmann's constant and T is the absolute temperature. At 800°C the amount of oxygen picked up after ~10⁴ h of exposure predicted by Equation 2 is 0.20 mg. The estimated levels of oxygen gain during our creep experiments compare favorably with actual experimental measurements. Kurtz and Hamilton [1] measured the oxygen pickup after 5142 h at 800°C at 345 wppm. The measured pickup of nitrogen was much less, only 15 wppm.

At 650 and 700°C the thickness of enhanced precipitation layers are about ~13 and 30% of the creep tube wall thickness, respectively. Therefore, for specimen AR13 tested at 700°C, about 70% of the specimen was deforming towards the end of the test in a manner typical of the starting interstitial content. However, it is interesting to note that for specimen AR20, although interstitial pick-up occurred all the way through the tube, the net consequence was only a modest increase in precipitate particle number density, because coarsening in this specimen produced precipitates comparable in size with the original distribution, at only a modest increase in number density. [The distribution of particles appears similar throughout Fig. 2c in comparison with the distribution away from the surface affected regions in Figs. 2a and b.] It should be noted that interstitial pickup did not play a significant role in our determination of secondary creep rates (see below) since calculation of the secondary creep rate were based on data gathered very early in the test when interstitial impurity pickup was negligible.

To put these observations into perspective, we have calculated the effective diffusion of oxygen and nitrogen through the wall of a pressurized tube. Two estimates were found for diffusion of oxygen in relevant vanadium alloys, V-5Ti [8] and V-5Cr-5Ti [9]. Data on nitrogen diffusion in V-5Cr-5Ti were not available so its diffusivity was estimated from information on oxygen and nitrogen diffusion in pure vanadium. The diffusivity of nitrogen in pure vanadium is about 15 times lower than oxygen at 650°C and about 10 times lower at 800°C [10]. Assuming the diffusion of nitrogen in V-5Cr-5Ti is lower than oxygen by an amount equal to the ratio of the nitrogen-to-oxygen diffusivity in pure vanadium an estimate of the effective diffusion distance for nitrogen in the alloy can be obtained. The results are summarized in Table 3. From these results, it is apparent that oxygen can diffuse through a pressurized tube with a wall thickness of 0.254 mm several times during the course of a creep test, even at 650°C. The diffusion distance of nitrogen is estimated to be much smaller than oxygen and may account for the observed precipitate distributions. Chemical analysis of the near surface precipitates will be performed to see if this hypothesis can be confirmed.

Table 3. Calculations for the effective diffusion distance of oxygen and nitrogen under conditions relevant to pressurized V-4Cr-4Ti creep tubes

Alloy	D_0 (m ² /sec)	Q (kJ/mol)	Temp (°C)	D (m ² /sec)	$x=\sqrt{Dt}$ (mm)
Oxygen					
V-5Ti [8]	3.1×10^{-4}	172	650	5.88×10^{-14}	1.5
V-5Cr-5Ti [9]	1.3×10^{-7}	120	650	2.05×10^{-14}	0.9
V-5Ti [8]	3.1×10^{-4}	172	800	1.34×10^{-12}	5.4
V-5Cr-5Ti [9]	1.3×10^{-7}	120	800	1.83×10^{-13}	2.0
Nitrogen					
V-5Cr-5Ti			650	1.37×10^{-15}	0.2
V-5Cr-5Ti			800	1.83×10^{-14}	0.6

In our previous work [3,4], two types of deformation microstructures were found. The first type exhibits the characteristics of the microstructures presented here in Figs. 4-7 and the second type is similar to the microstructure shown in Fig. 8. Figure 10 provides a plot of the stress dependence for creep with the data points corresponding to microstructural examinations labeled. The microstructures of specimens AR16 and AR20 show well-developed sub-grains, whereas all other specimens exhibit dislocation tangles and poorly defined sub-grains. From Fig. 10, it is clear that specimen AR20 is creeping with a lower stress dependence of ~0.8 in comparison with the other conditions examined where the stress dependence is ~4. Specimen AR16 appears to be in a transition region and this may explain why the dislocation density within sub-grains in this specimen was moderate, in contrast to observations in specimen AR20 shown in Fig. 3e where dislocation structures were almost entirely in sub-grain boundaries. The microstructural differences clearly correspond to changes in creep mechanism. Previously, [1,2] we attributed the creep response in the high-stress exponent regime to some form of dislocation climb controlled process and in the low-stress exponent region to processes involving grain boundary sliding, Coble creep, or some combination of the two. The culmination of our microstructural observations indicates that creep in the high-stress exponent region is due to a viscous glide rather than a climb controlled mechanism. Such a conclusion is consistent with many of our observations. As noted by Mohamed and Langdon, [11], creep of solid solution alloys controlled by a dislocation climb mechanism should be similar to that of pure metals, namely, 1) the stress exponent is close to 5, 2) an instantaneous strain occurs on application of the load, 3) the creep curve exhibits normal primary creep, 4) the steady-state creep rate is dependent on the stacking fault energy of the alloy, and 5) a regular array of sub-grains is formed during creep. When creep of solid solution alloys is controlled by a viscous glide process features different from those observed in pure metals are found, namely, 1) the stress exponent is close to 3, 2) there is little or no instantaneous strain on application of the load, 3) the creep curve enters the steady-state region almost immediately, 4) the steady-state creep rate appears to be independent of the stacking fault energy of the alloy, and 5) sub-grains are not generally formed during creep or, if formed, are less extensive than in pure metals. Mohamed and Langdon, [11], developed a simple criterion to determine under what conditions a solid solution alloy would favor glide-controlled creep over climb-controlled creep. The criterion for viscous glide controlled creep is:

$$\frac{B\sigma^2}{k^2(1-\nu)} \left(\frac{\gamma}{Gb} \right)^3 > \frac{T^2}{e^2cb^6} \quad (3)$$

where $B \sim 8 \times 10^{12}$, σ is the stress, k is Boltzmann's constant, ν is Poisson's ratio, γ is the stacking fault energy, G is the shear modulus, b is the Burgers vector, T is the temperature, e is the solute-solvent size difference and c is the solute concentration. Assuming that Ti is the solute controlling viscous glide, taking the stacking fault energy for V-4Cr-4Ti to be 0.2 J/m² [12], using a stress of 100 MPa at a temperature of 1000 K one obtains a prediction that creep of V-4Cr-4Ti in the high stress regime should

be predominantly viscous glide controlled since the left hand side of Eq. 3 gives a value of $\sim 5 \times 10^{57}$ compared to the right hand side, which is $\sim 10^{55}$.

Finally, it should be noted that at low stresses, if the stress exponent for creep approaches 1, as shown in Fig. 10, then a change in creep mechanism to grain boundary sliding or Coble creep is expected [13,14]. If creep is controlled by the stress-directed flow of vacancies, with diffusion along grain boundaries (Coble), then Langdon [14] notes that such creep can be identified by examining the microstructure for grain elongations, with denuded zones at boundaries in tension and associated precipitate pile-ups at boundaries in compression. Specimen AR20 provides a test, given 12.7% diametral strain. If diffusion creep is significant, then the metallographic images in Figs. 1c and 2c should reveal grain elongation in tangential directions and precipitate pile-ups on grain boundaries parallel to the tangential direction. Careful examinations reveal no precipitate pile-ups suggesting that creep in the low-stress regime is controlled by grain boundary sliding processes possibly accommodated by lattice or grain boundary diffusion. A further test of this hypothesis would be to determine grain aspect ratios before and after creep testing. No change in grain aspect ratios should occur if grain boundary sliding is the predominant creep mechanism at low stresses. Furthermore, observation of well-defined subgrains is indicative of significant dislocation motion and rearrangement during creep, not expected for grain boundary sliding or Coble creep. In future work, we intend to consider the possibility of Harper-Dorn creep [15] controlling this behavior despite the lower temperature regime.

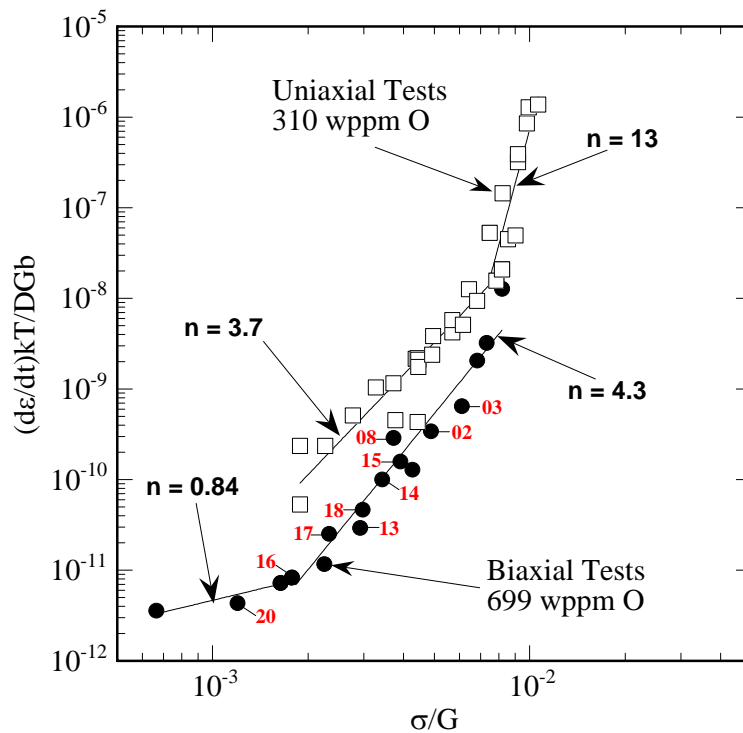


Fig. 10. Stress dependence of the normalized effective mid-wall creep strain for unirradiated vanadium alloys, with pressurized tube specimens chosen for microstructural examination identified by number.

Results

Five pressurized tubes of V-4Cr-4Ti have been examined following thermal creep testing to $\sim 10^4$ hr in the temperature range 650-800°C in order to understand the mechanisms controlling creep. It is found in all

cases that creep is controlled by dislocation motion. But the mechanism changes with increasing temperature from one controlled by the climb and interaction of individual dislocations, to one controlled by sub-grain boundary structure that is created by relaxation of the interacting dislocations to a lower energy planar array.

Evidence for an increased density of (Ti,V) oxy-carbo-nitride precipitates near the outer surface extending inwards a distance of 30 and 70 μm , respectively, was found after 650 and 700°C after $\sim 10^4$ h. At 800°C, enhanced (Ti,V) oxy-carbo-nitride precipitation was observed across the entire tube wall thickness and may have affected creep response. Calculations provide prediction that nitrogen contamination may be responsible. Also, evidence for internal precipitation associated with the dislocation structure could be identified.

The mechanism controlling creep behavior at higher stresses/lower temperatures is shown to most likely be viscous glide controlled creep arising from the presence of Ti and Cr solid solution hardening. The mechanism controlling behavior at lower stresses/higher temperatures should be grain boundary sliding or Coble creep, but given evidence for extensive dislocation production and rearrangement, consideration is being given to the alternate explanation of Harper-Dorn creep.

Future Work

The effort will be continued as opportunities become available.

References

- [1] R. J. Kurtz and M. L. Hamilton, DOE/ER-0313/25 (1999) 7.
- [2] R. J. Kurtz, A. M. Ermi, and H. Matsui, DOE/ER-0313/31 (2002) 7.
- [3] D. S. Gelles, M. L. Hamilton, and R. J. Kurtz, DOE/ER-0313/26 (1999) 11.
- [4] D. S. Gelles, DOE/ER-0313/31 (2001) 12.
- [5] D. S. Gelles, A. Kimura, and R. J. Puigh, DOE/ER-0313/12 (1992) 123.
- [6] D. S. Gelles and H. Li, DOE/ER-0313/19 (1996) 22.
- [7] B. A. Pint and J. R. DiStefano, J. Nucl. Mater. 307-311 (2002) 560.
- [8] H. Nakajima, S. Nagata, H. Matsui, and S. Yamaguchi, Phil. Mag. A67 (1993) 557.
- [9] M. Uz, K. Natesan, and V. B. Hang, J. Nucl. Mater. 245 (1997) 191.
- [10] F. A. Schmidt and J. C. Warner, J. Less-Common Metals 26 (1972) 325.
- [11] F. A. Mohamed and T. G. Langdon, Acta Mater. 22 (1974) 779.
- [12] M. S. Duesbury and V. Vitek, Acta Mater. 46 (1998) 1481.
- [13] R. L. Coble, J. Appl. Phys. 34 (1963) 1679.
- [14] T. G. Langdon, in Creep Deformation: Fundamentals and Applications, Eds., R. S. Mishra, J. C. Earthman, and S. V. Raj, TMS, Warrendale Pa. (2002) 41.
- [15] J. Harper and J. E. Dorn, Acta Met. 5 (1957) 654.

ROOM TEMPERATURE COMPRESSION PROPERTIES OF TWO HEATS OF UNIRRADIATED V-4Cr-4Ti—M. B. Toloczko (Pacific Northwest National Laboratory)* and R. J. Kurtz (Pacific Northwest National Laboratory)*

OBJECTIVE

Cylindrical specimens fabricated from Heat 832665 (US Heat) of V-4Cr-4Ti and from Heat P8013 (NIFS-2 Heat) of V-4Cr-4Ti were tested in compression at room temperature on a screw-driven test frame. The average value of the yield strength was 344 MPa for the US Heat and 315 MPa for the NIFS-2 Heat. The average strain hardening exponent calculated from the first few percent of plastic strain was about 0.17 for both the US Heat and the NIFS-2 heat. As is common in a compression test, the specimens barreled somewhat during the tests.

PROGRESS AND STATUS

Introduction

Vanadium alloys are of interest to the Fusion program as potential first wall structural materials. The expected irradiation conditions for the first wall structural material include a range of temperatures where very high hardening caused by a high density of small, but shearable defect clusters results in a type of deformation called "localized deformation". At the onset of yield in a tensile test, a dislocation may move through a grain shearing the obstacles and clearing out a channel. Subsequent dislocations may easily pass through this channel. As the test progresses, more channels form. In the early stages of deformation, it is thought that the plastic deformation is confined to these channels. One important macroscopic result of this deformation behavior is rapid onset of necking in a tensile test and very low uniform elongation. As a means to help understand the range of stress states where localized deformation may adversely affect macroscopic ductility in vanadium alloys, compression test specimens fabricated from two heats of V-4Cr-4Ti are currently under irradiation in the High Flux Isotope Reactor (HFIR). The results of room temperature compression tests on the unirradiated control materials are presented here and compared with uniaxial tensile values from the literature.

Experimental Procedure

Heat 832665 (US Heat), and Heat P8013 (NIFS-2 Heat) were utilized. The US Heat was received in the form of thirty 3.0 mm diameter by 6.6 mm long cylinders electro-spark machined (EDM'ed) from a 40% cold-worked plate (called the R-plate). The NIFS-2 Heat was received in the form of a ~4 mm thick plate in a 98% cold-rolled condition. 3.0 mm diameter by 3.5 mm long specimens were EDM'ed from the plate. A limitation of the EDM process is that a small ridge is left running down the length of the specimens. This ridge was machined off. The US specimens were reduced in length to 3.5 mm, and the ridge on these samples was also removed. Specimen IDs were then laser engraved. After machining and engraving, the compression specimens were ultrasonically cleaned in methanol followed by ethanol, and then the specimens were loosely wrapped in tantalum and then titanium foil. (Foil packets were also cleaned in methanol and ethanol.) The foil packets were placed in a vacuum furnace and heat treated at 1000°C for 2 h at better than 1×10^{-6} torr.

*Pacific Northwest National Laboratory (PNNL) is operated for the U.S. Department of Energy by Battelle Memorial Institute under contract DE-AC06-76RLO-1830.

Compression tests were performed in a 10,000 lb screw-driven Instron test frame with a 1000 lb load cell. A special compression test fixture, as shown in Fig. 1, was constructed for the testing. The upper and lower loading surfaces of the fixture are made from a high modulus tungsten carbide composite with a polished surface. The upper loading surface is in the form of a piston which is guided by a cylinder made from a machineable carbide composite. A tight tolerance was maintained between the piston and cylinder to limit axial misalignment between the upper and lower loading surfaces. For these room temperature tests, the upper and lower loading surfaces were lubricated with a thin later of a light machine oil. (Tests performed without lubricant resulted in significantly greater specimen barreling.) Tests were run at an initial strain rate of $5 \times 10^{-4} \text{ sec}^{-1}$. Specimen displacement was monitored with a capacitance-type displacement transducer with a resolution better than 0.0002 mm (better than 0.006% strain). The transducer directly monitors the displacement between the upper and lower loading surfaces. Data were recorded electronically. Yield strength (YS) measurement and curve fits to the plastic strain data were done by hand. Three tests each were done on the two heats.

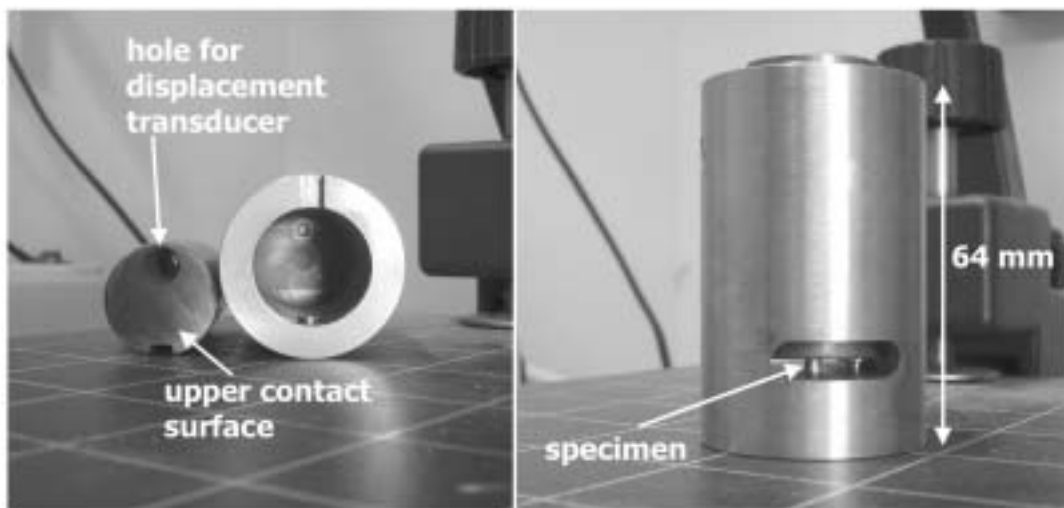


Fig. 1. Picture of the compression test fixture used for the tests.

Results and Discussion

The specimens deformed predictably with some amount of barreling occurring as shown in Fig. 2. Typical engineering stress versus engineering strain plots for the US Heat and the NIFS-2 Heat are shown in Fig. 3. The Young's modulus of vanadium is around 130 GPa. The slope of the linear loading region varied from 37 GPa to 48 GPa indicating some load train elasticity is present in the displacement measurement. Both heats show a smooth transition into plastic deformation, and upper/lower yield point behavior is apparent. The 0.2% strain offset line almost exactly intersected the upper yield point, so the two stress values are equivalent here. Yield strength values are shown in Table 1. For each heat, the YS values are consistent, with a spread in the three tests of no greater than 10 MPa (3% of the YS value). Strain hardening exponents were also measured. Examples of curve fits to the true stress versus true plastic strain plots are shown in Fig. 4. From these curve fits, strain hardening exponents were calculated assuming the material obeys power law strain hardening (PLSH) behavior ($\sigma = k\varepsilon^n$). Because of barreling, these are not exact true stress and true plastic strain values, but the curves nevertheless serve as a means to estimate the strain hardening coefficient. Curve fits were done either in the range of 1% to 2% true plastic strain, 4% to 6% true plastic strain, or 6% to 11% true plastic strain. The curve fits were confined to ranges of plastic strain (rather than the entire curve) because the true stress versus true strain curves do not obey the PLSH equation over the entire range. The strain hardening exponents calculated from these curve fits are shown in Table 1. As with the YS measurements, the strain hardening exponents over any particular range of strain had a low spread.

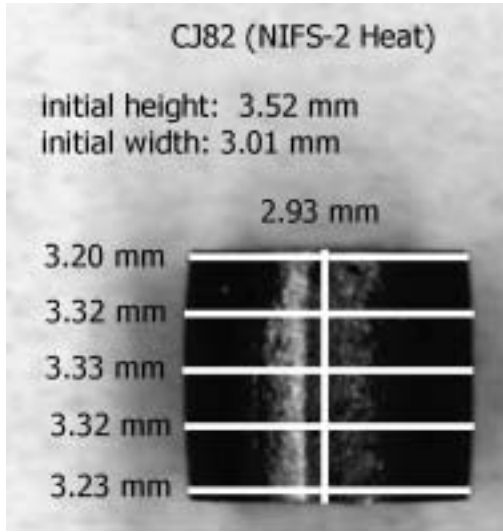


Fig. 2. Image of a specimen tested to 16% engineering strain. Some barreling is evident.

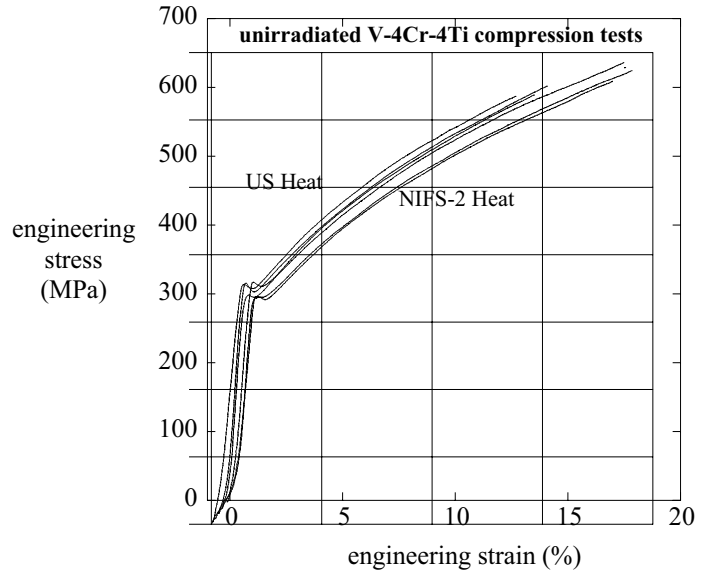


Fig. 3. Engineering stress versus strain plots for room Temperature compression tests of the US Heat and the NIFS-2 Heat of V-4Cr-4Ti in the unirradiated condition.

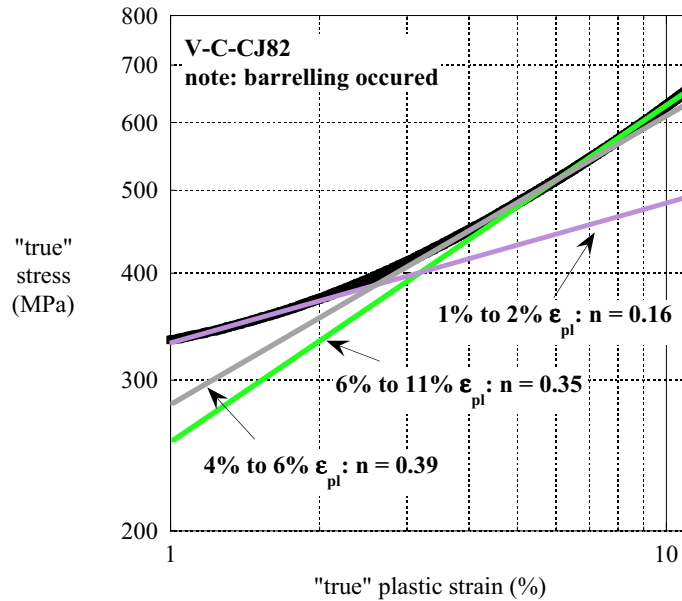


Fig. 4. Example of PLSH fits to the true stress versus true plastic strain compression test plots. Because of barreling, these are not exact true stress and true plastic strain values. The reader should note the logarithmic scales in this plot.

Table 1 -- Yield stress and strain hardening exponents found from the compression test curves

ID code	Yield stress (MPa)			Ratio of US/Japan	Strain hardening coefficient		
	0.2% Offset strain	Upper yield point	Average		$1\% \leq \epsilon_{pl} \leq 2\%$	$4\% \leq \epsilon_{pl} \leq 6\%$	$6\% \leq \epsilon_{pl} \leq 11\%$
CA19*	340	340	344	1.09	0.17	0.34	0.40
CA25	348	348			0.17	0.34	0.40
CA28	344	344			0.16	0.33	0.40
CJ82†	320	320	315		0.16	0.34	0.39
CJ88	310	310			0.16	0.35	0.41
CJ99	315	315			0.17	0.37	0.42

* CA## = US Heat

† CJ## = NIFS-2 Heat

Uniaxial tensile data at 25°C from the literature shows a YS of about 315-355 MPa for the US Heat [1-3] and about 300 MPa for the NIFS-2 Heat [4]. The YS of the US Heat is stronger most likely because of the greater amount of oxygen in this material [5]. These tensile specimens received the same final heat treat that the compression specimens received. The YS values measured in compression are very close to the values measured in tension. The similarity between tension and compression is not unexpected because ductile polycrystalline materials with random grain orientation usually have an isotropic von Mises yield surface. If there were a significant difference between the tension and compression values, it would have likely been due to some difference in grain size or shape or orientation between the tensile and compression specimens.

For compression tests, it is useful to extract some measure of ductility that can be compared to ductility parameters from other tests. There is no uniform elongation in a compression test, but the strain hardening exponent can be measured (assuming the material obeys PLSH). In a tensile test, if the material obeys PLSH, then the strain hardening exponent will equal the true uniform elongation (TUE). This relationship can be used to compare the strain hardening exponent from compression tests to the TUE from tensile tests. Uniform elongation (UE) values in the literature for the US Heat are in the range of 16-18% [1-3]. Values for NIFS-2 Heat are not readily available, but values for NIFS-1 Heat are in the range of 18% [6]. These UE values from the literature are probably engineering values. TUE can be found from

$$\epsilon_u = \ln(1 + e_u) \quad (1)$$

where e_u is the engineering value. A UE of 18% is equivalent to a TUE of about 16.5%. From Table 1, it can be seen that for the compression tests, the strain hardening exponent found from the range of 1% to 2% true plastic strain in the compression tests matches up well with the TUE obtained from the literature data on tensile properties. For strain hardening exponents measured by the authors on tensile data from a variety of materials [7] the best match between tensile strain hardening exponent and true uniform elongation (from the same tensile specimen) has occurred when the strain hardening exponent was measured at relatively high values of plastic strain. The situation is the exact opposite for the compression specimens. It is thought that barreling of the compression specimens affected the apparent true stress and true plastic strain behavior with the low range of plastic strain being the least affected, and thus, providing the strain hardening exponent that matches best with the true uniform elongation found from tensile data.

Barreling of the specimens was assessed by measuring radial displacement at regularly spaced intervals along the length of a tested sample and comparing these values to the radial displacement that would have occurred if the specimen had not barreled. The axial displacement and the volume of the sample can be used to find the "ideal" radius after deformation if the sample had not barreled:

$$r_{\text{ideal}} = \sqrt{\frac{V}{\pi h_f}} \quad (2)$$

where V is the volume of the specimen, and h_f is the final height of the tested specimen. The radial strain values at five positions along the length of one tested specimen are compared to the ideal radial displacement in Table 2. There is a several percent radial strain difference between the ends and the middle of the specimen. However, in the mid-region of the sample, the variation in radial strain is small, showing that the majority of the barreling occurred outside the middle section of the samples.

Table 2. Measured radius at positions along the length of one NIFS-2 sample after a compression test
Measurement points are shown in Fig. 2.

Specimen CJ82		
Item	Radius (mm)	Strain (%)
<i>calculated</i> radius from measured axial strain and sample volume	3.29	9.2
<i>measured</i> radius at top of specimen	3.20	6.7
<i>measured</i> radius in top half of specimen	3.32	10.6
<i>measured</i> radius at mid-point of specimen	3.33	10.9
<i>measured</i> radius in bottom half of specimen	3.32	10.6
<i>measured</i> radius at bottom of specimen	3.23	7.7
<i>average of the five measured values</i>	3.28	9.3

The observed values of between 37 GPa and 48 GPa for the elastic loading slope was much lower than expected. It was thought that the position of the displacement measurement transducer in the compression test fixture would have eliminated any load train elasticity from the measurement. The cause of the low values will be investigated in the future.

The smooth curvature of the compression test traces around the upper/lower yield area is different from tensile tests on these materials. In the tensile tests, the initial yield point at room temperature is typically sharp. This is followed by a relatively small yield drop and propagation of a Lüders band at constant load. Consideration was first given to the possibility that a soft load train may have smoothed the appearance of the upper/lower yield point behavior in compression, but a review of the effects of machine stiffness on observed yield point behavior suggests that a soft load train would not cause this [8]. So, further consideration was given to the yield point phenomenon in compression and in tension. Presumably, during a tension test, yielding initiates at a stress concentration in the gauge section, and a sharp yield drop occurs as dislocations break free from their Cottrell atmosphere. Plastic deformation occurs in the vicinity of the stress concentration until the material hardens. During a compression test, a stress concentration may still form, but geometric hardening of the material due to plastic deformation in the region of the stress concentration may more rapidly strengthen this region and promote more homogeneous deformation throughout the sample.

Two heats of unirradiated V-4Cr-4Ti were tested in compression at room temperature. The yield strength in compression matched up well with the values for the same materials in tension, and the strain hardening exponent calculated from the first few percent of plastic strain matches up well with the uniform

elongation values from tensile tests. Barreling, which typically occurs in a compression specimen, was observed in the vanadium samples.

Overall, the material behaved predictably, and these tests will serve as a reference for tests to be conducted in the future on irradiated vanadium compression specimens. The combined data from tensile and compression (and perhaps other test geometries) will be useful in determining the deformation behavior of vanadium under more complex loading conditions.

Future Work

Elevated temperature tests will be performed on unirradiated vanadium compression specimens. Compression tests will also be performed on the irradiated specimens when they become available.

References

- [1] A. F. Rowcliffe, S. J. Zinkle, and D. T. Hoelzer, Effect of strain rate on the tensile properties of unirradiated and irradiated V-4Cr-4Ti, *J. Nucl. Mater.* 283-287 (2000) 508-512.
- [2] M. C. Billone, Revised ANL-reported tensile data for unirradiated and irradiated (FFTF, HFIR) V-Ti and V-Cr-Ti Alloys, Fusion Materials Semi-annual Progress Report, DOE/ER-0313/23, December 1997, pp. 3-61.
- [3] D. J. Alexander, L. L. Snead, S. J. Zinkle, A. N. Gubbi, A. F. Rowcliffe, and E. E. Bloom, Effects of irradiation at low temperature on V-4Cr-4Ti, Fusion Materials Semi-annual Progress Report, DOE/ER-0313/20, June 1996, pp. 87-95.
- [4] A. Nishimura, T. Nagasaka, and T. Muroga, Fracture properties of high-purity V-4Cr-4Ti alloy (NIFS-HEAT-2) at room temperature, *J. Nucl. Mater.* 307-311 (2002) 571-575.
- [5] D. L. Harrod and R. E. Gold, Mechanical properties of vanadium and vanadium-based alloys, *International Metals Reviews* No. 4 (1980) 163-221.
- [6] K. Fukumoto, T. Yamamoto, N. Nakao, S. Takahashi, and H. Matsui, High temperature performance of highly purified V-4Cr-4Ti alloy, NIFS-Heat 1, *J. Nucl. Mater.* 307-311 (2002) 610-614.
- [7] M. B. Toloczko, M. L. Hamilton, and G. E. Lucas, Ductility correlations between shear punch and uniaxial tensile test data, *J. Nucl. Mater.* 283-287 (2000) 98-991.
- [8] M. A. Meyers and K. K. Chawla, Mechanical Metallurgy, Principles and Applications, Prentice-Hall, Inc., 1984, pp. 575-577.

2.0 CERAMIC COMPOSITE MATERIALS

CHARACTERIZATION OF SILICON CARBIDE COMPOSITES PRODUCED BY POLYMER-IMPREGNATION AND HIGH TEMPERATURE PYROLYSIS PROCESS—Y. Katoh and T. Nozawa (Oak Ridge National Laboratory), K. Ozawa and A. Kohyama (Kyoto University)

OBJECTIVE

The objective of this task is preliminary assessment of polymer-impregnation and pyrolysis (PIP) process that incorporates near-stoichiometric SiC matrix and/or very high temperature treatment as a potential processing technique for SiC/SiC structural ceramic composite for fusion blanket applications. The present work focuses on characterization of microstructures and flexural properties of high temperature-treated PIP SiC/SiC composites with near-stoichiometric SiC fiber reinforcement and pyrolytic carbon / SiC bi-layered interphase.

SUMMARY

Near-stoichiometric SiC fiber composites with polymer-derived high-crystallinity SiC matrices were produced and were characterized their microstructures and mechanical properties. The material was produced through repeated polymer-impregnation and pyrolysis (PIP) cycles of Tyranno™-SA sintered SiC fibers, following pyrolytic carbon and SiC bi-layer interphase deposition. Co-polymer of polycarbosilane (PCS) and polymethylsilane (PMS) was used as the precursor for near-stoichiometric SiC matrix. The final heat treatment was performed at 1100 – 1800°C in flowing commercial-purity argon. The produced composites were dense in general with small macro-porosity. Transmission electron microscopy revealed that the matrix microstructures after heat treatment at >1500°C consisted of fine layers of SiC crystallites in amorphous SiC and carbon matrix. High temperature heat treatment promoted crystallization at the expense of porosity. No degradation of Tyranno-SA fiber was identified after heat treatment at 1800°C. PIP-composites with well-crystallized SiC matrices exhibited flexural fracture behavior very similar to that of chemically vapor infiltrated composites. The composites maintained ambient temperature strength up to 1000°C in air and to 1300°C in argon.

PROGRESS AND STATUS

Introduction

SiC continuous fiber-reinforced SiC-matrix composites (SiC/SiC composites) are an advanced option for structural materials in nuclear fusion and gas-cooled fission systems [1,2]. Nuclear applications of SiC/SiC composites require crystallinity and stoichiometry to both fibers and matrices in order for achieving acceptable tolerance against neutron-induced damage [3]. Among several industrially available matrix densification techniques, chemical vapor infiltration (CVI) best meets such requirements. On the other hand, CVI composites generally contain macroscopic inter-fiber bundle pores which hamper several important properties related with composite rigidity and transport properties [4]. Incorporating polymer impregnation and pyrolysis (PIP) process for the purpose of filling the macropores is one of the potential concepts of process hybridization oriented for complementing the known drawbacks of CVI products. PIP-produced matrices are generally carbon-rich, oxygen containing, and amorphous to nano-crystalline and therefore extremely susceptible to neutron damage [5]. However, it has been demonstrated that the irradiation resistance of PIP-matrices would be improved through pyrolysis and/or heat treatment in

conditions where enhanced crystallization occurs [6]. In this work, near-stoichiometric SiC fiber composites with pyrolytic carbon (PyC) / SiC bi-layered interphase were produced by pyrolysis and/or heat-treatment at temperatures of $<1800^{\circ}\text{C}$ and characterized for microstructures and mechanical properties.

Experimental Procedure

The fabricated composites and their processing conditions are summarized in Table 1. SiC fiber used was Tyranno™-SA near-stoichiometric sintered SiC fiber except for the case of TyTE-S6/PCS-1100°C, which was studied as a commercial standard PIP composite. For the interphase between fibers and matrices, bi-layers of 200nm-thick PyC and 500nm-thick SiC were deposited on the fiber fabric by CVI. The inner PyC layer provides compliant interlayer that easily debonds, while the outer SiC layer helps filling fine inter-fiber openings, adds rigidity to composites, and provides protection to the PyC layer. The preceramic polymers used were polycarbosilane (PCS), polyvinylsilane (PVS) [7], and co-polymer of polymethylsilane and PCS (PMS/PCS) [8]. The PMS/PCS co-polymer was designed so that near-stoichiometric SiC to be produced by setting a mixing ratio of $\text{PMS}/(\text{PMS}+\text{PCS}) = 0.7$. The PIP cycles were repeated typically for 10 times until composite mass density of $>2.2\text{g}/\text{cm}^3$ was achieved.

Microstructural examination was performed by scanning electron microscopy (SEM) on polished cross-sections for all the materials and by transmission electron microscopy (TEM) on thin films produced by focused ion-beam micro-processing for selected samples. Mechanical property was evaluated primarily by three-point flexural testing at ambient temperature in air and at 1300°C and 1500°C in a flow of commercial purity argon.

Table 1. Summary of processing conditions and properties of composites studied

Material ID	TyTE-S6 /PCS-1100C	TySA /PVS-1800C	TySA/(PyC/SiC) /PCS-1750C	TySA/(PyC/SiC) /PCS-1700C	TySA/(PyC/SiC) /(PMS/PCS)- 1200C	TySA/(PyC/SiC) /(PMS/PCS)- 1500C	TySA/(PyC/SiC) /(PMS/PCS)- 1700C
Fiber	Tyranno-TE-S6	Tyranno-SA	Tyranno-SA	Tyranno-SA	Tyranno-SA	Tyranno-SA	Tyranno-SA
Architecture	2D-PW	Unidirectional	2D-PW	2D-PW	3D(1:1:0.2)	3D(1:1:0.2)	3D(1:1:0.2)
Interphase(s)	Carbonized	(none)	PyC ^{200nm} /SiC ^{500nm}				
Precursor	PCS	PVS	PCS	PCS	PMS/PCS	PMS/PCS	PMS/PCS
Pyrolysis/HT temperature	1100C	1800C	1750C	1700C	1200C	1500C	1700C
Particulate loading	None	First cycle	None	None	None	None	None
V _f	~40%	~40%	34%	32%	~35%	~35%	~35%
Mass density	2.10g/cm ³	2.48g/cm ³	2.29g/cm ³	2.58g/cm ³	2.24g/cm ³	2.29g/cm ³	2.27g/cm ³
Porosity	15.7%	19.2%	25.4%	17.1%	Not measured		
Flexural properties							
Modulus	76GPa	128GPa	98GPa	132GPa	63GPa	60GPa	55GPa
Prop. Limit	76MPa	216MPa	153MPa	252MPa	153MPa	154MPa	148MPa
Ultimate	124MPa	237MPa	170MPa	258MPa	302MPa	282MPa	198MPa
ε at Load Max	1.17%	0.19%	0.19%	0.24%	0.96%	0.74%	0.42%

Results and Discussion

The SEM microstructures of polished fiber bundle cross-sections are presented in Fig. 1. It was confirmed that the bi-layered interphases were deposited as designed in all the composites. Appearance of the matrices were similar in TyTE-S6/PCS-1100°C and TySA/(PyC/SiC)/(PMS/PCS)- 1200°C, both with very small microporosity within their fiber-bundle regions. Neither deformation of Tyranno-SA fibers nor structural instability of the bi-layered interphase was noticed after heat treatment at 1500 – 1750°C. Heat treatment at 1500°C slightly added micropores in the PMS/PCS-derived matrix, and that at 1700 and 1750°C resulted in rather severe microporosity in the PCS and PMS/PCS matrices due probably to volume shrinkage associated with crystallization and carbothermal reduction. There was a significant difference in appearance of heat-treated matrices; the PCS- and PVS-derived matrices shrunk into blocky grains leaving intergranular openings, while the PMS/PCS-derived matrix shrunk toward the fiber surfaces leaving pores amid inter-fibers.

Figure 2 shows TEM images of the matrix regions in selected materials. The PCS-1100°C matrix comprises nanocrystallites of cubic SiC (crystallites imaged by reflection at partial $\langle 111 \rangle$ ring as the tiny bright spots are indicated by arrows in Fig. 2-a) embedded in amorphous siliconoxycarbide, which is typical for conventional PCS-derived products [9]. The PCS-1700°C and -1750°C matrices were polycrystalline cubic SiC of typical grain size of 100 – 500nm with small amount of graphitic pockets located at multi-grain boundaries. The PVS-1800°C matrix was very similar to the lower temperature matrices with slightly larger grain sizes of SiC. Therefore, microstructural evolution in the PCS-derived matrices during heat treatment is probably isotropic growth of SiC crystallites accompanied by emission of gaseous oxides and

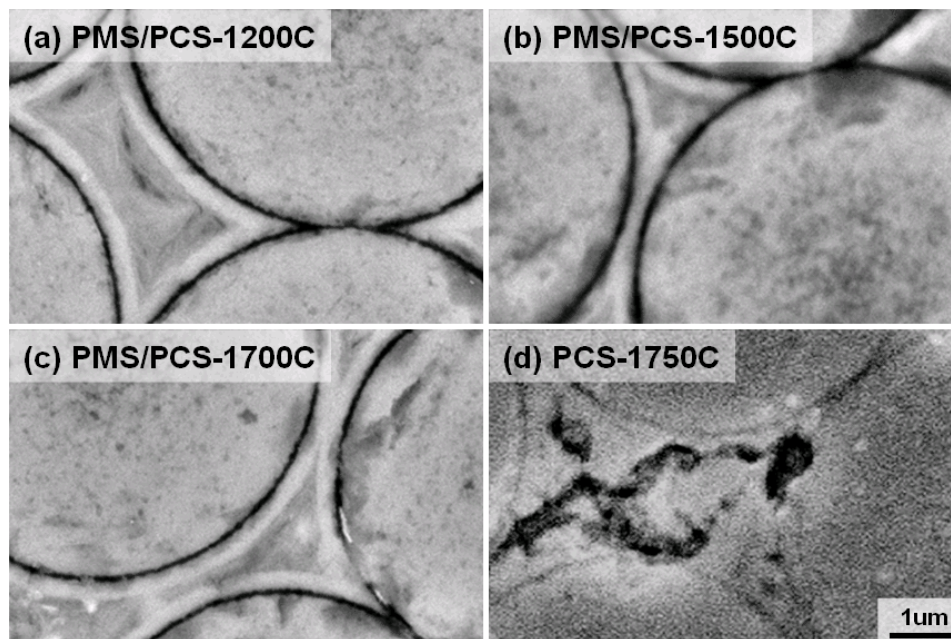


Fig. 1. Scanning electron micrographs of polished cross-sections of PCS- and PMS/PCS-derived matrix composites. Note that only micrograph (d) is a secondary electron image while the others are backscattered electron images.

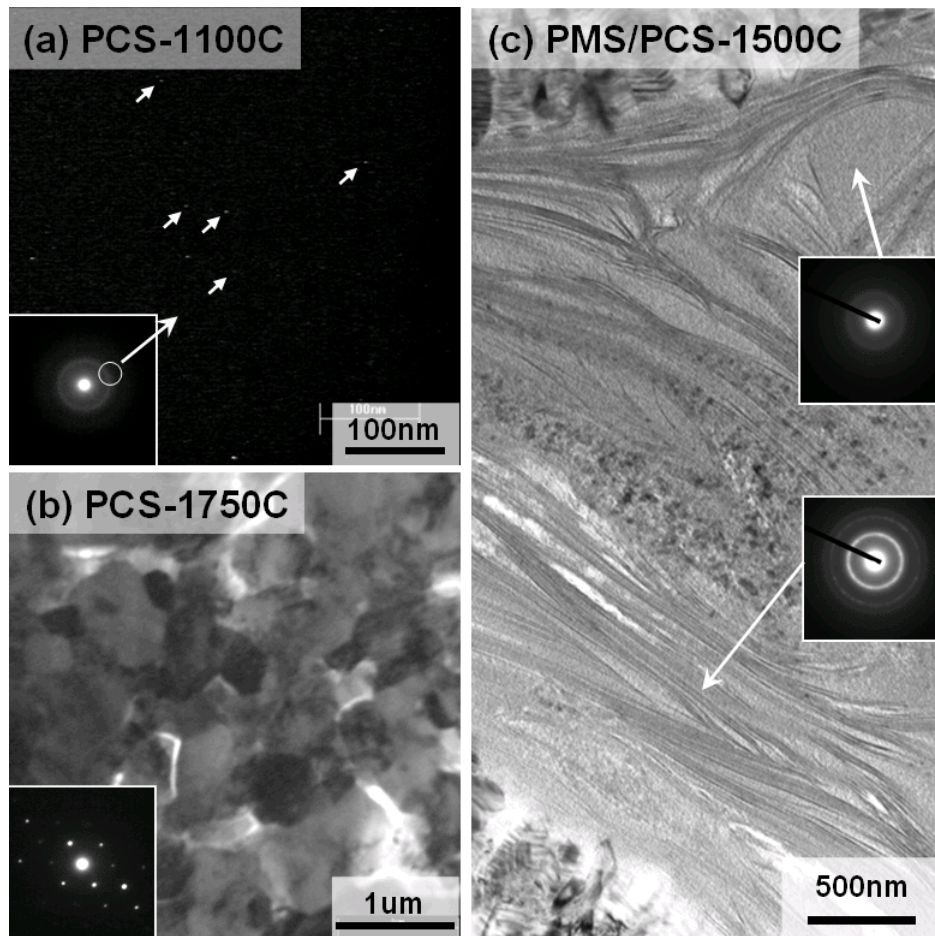


Fig. 2. Transmission electron images of polymer-derived matrices; (a) PCS-derived matrix pyrolyzed at 1100°C, (b) PCS-derived matrix heat-treated at 1750°C, and (c) PMS/PCS-derived matrix heat-treated at 1500°C.

graphitization of the residual carbon.

The microstructures of PMS/PCS-derived matrices were unique. They consisted of numerous numbers of very thin layers (~10nm in thickness) of polycrystalline SiC in an amorphous 'matrix', as shown in Fig. 2-c. The appearance in TEM did not undergo noticeable change by heat treatment at 1500°C. This suggests superior thermal stability of the near-stoichiometric PIP matrix over that of conventional PCS-derived matrices. However, heat treatment at 1700°C caused significant coarsening of the laminar structures of SiC, thin (10 – 100nm) planar openings between SiC layers, and a loss of amorphous phase. The lack of mass loss by the heat treatment (Table 1) suggests that significant outgassing did not take place during the enhanced crystallization.

It is worth noting that Tyranno™-SA Grade-3 fibers used in this study did not undergo significant change by the heat treatment at <1800°C. As shown in Fig. 3, the carbon-rich core region and the more stoichiometric near surface region were both microstructurally stable without noticeable grain growth during the heat treatment. Fiber deformation did not take place, no change in the fiber fracture surfaces

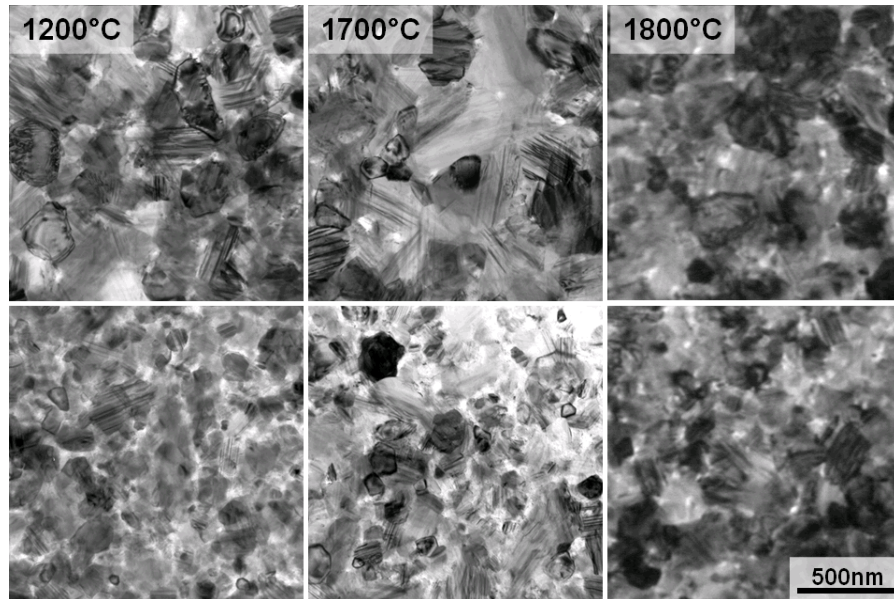


Fig. 3. Transmission electron micrographs showing microstructural stability of near-surface (upper) and core (lower) regions in Tyranno-SA fibers. Heat treatment temperature is indicated at the top left corners.

was noticed after heat treatment at $<1800^{\circ}\text{C}$, either [10]. This is in contrast to the reported slight grain growth in the same fiber after pressure sintering at 1780°C [11], where it is believed that the pressure of 20MPa was playing a major role.

Ambient temperature stress-strain behavior during flexural testing is compared in Fig. 4. Although the enhanced matrix crystallization makes composites' fracture behavior apparently more brittle, it actually accompanies a major transition of fracture mode from primarily interlaminar failure, often initiated by compressive failure, to trans-thickness fracture initiated on the tension side. The high temperature heat-treated composites still exhibit load increase beyond their proportional limit stresses. CVI composites with TyrannoTM-SA or Hi-NicalonTM Type-S exhibit similar flexural fracture behavior [12]. All the TyrannoTM-SA composites except the one pyrolyzed at 1800°C exhibited fiber pull-out with pull-out lengths comparable to those for CVI composites with the same fiber. Therefore, the apparently more brittle fracture observed does not actually mean problematic nature of the high temperature PIP composites. Interestingly, the initial flexural modulus was not significantly altered by the heat treatment. This is probably because the enhanced matrix crystallization compensated the effect of porosity increase on the composite modulus. At 1000°C and 1300°C in argon, ultimate flexural strength for all of the TySA/(PyC/SiC)/(PMS/PCS)- 1200°C , 1500°C and 1700°C composites were almost the same as that obtained at ambient temperature. Proportional limit stresses at elevated temperatures were by 10 – 20% higher than at ambient, possibly due to reduction of residual stress. Apparent flexural moduli at elevated temperatures decreased to 50 – 70% of the values at ambient temperature for all the composites [13]. The reason for this modulus reduction is uncertain.

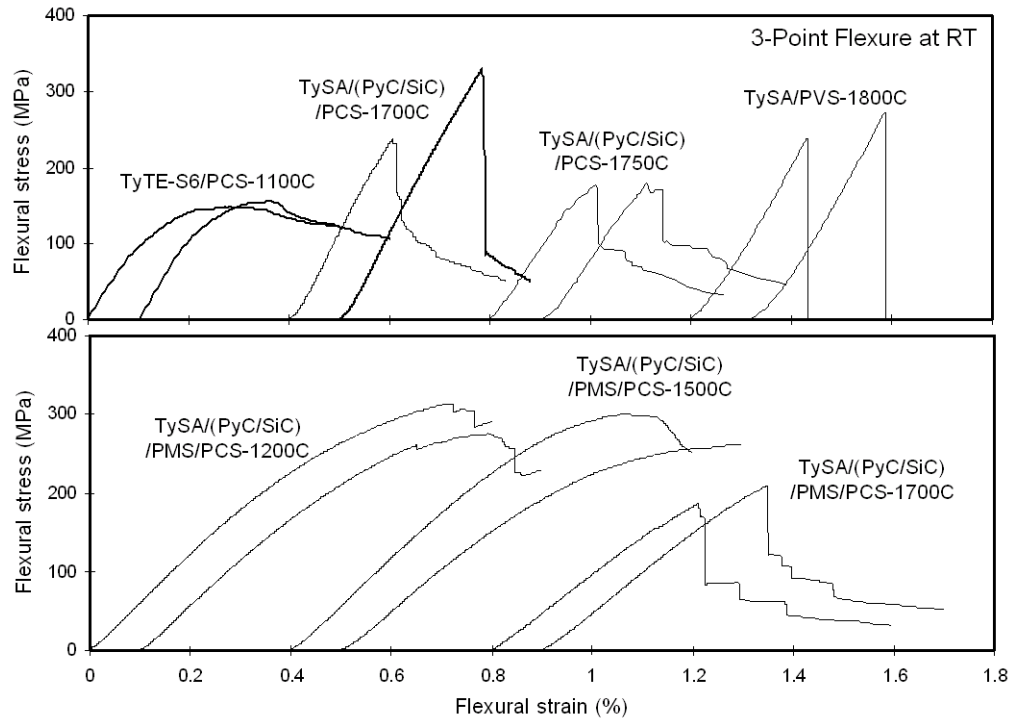


Fig. 4. Apparent stress – strain relationships of the composites during three-point flexural testing at ambient temperature.

Future Work

SiC/SiC composites made with Tyranno™-SA SiC fibers, PyC/SiC bi-layered interphase, and SiC-based matrices derived from PMS/PCS near-stoichiometric SiC precursor will be examined after neutron irradiation at 1,000°C for two HFIR cycles in a static rabbit irradiation capsule. Determination of irradiated tensile strength, proportional limit stress and tangential modulus, and microstructural examination are planned.

References

- [1] B. Riccardi, L. Giancarli, A. Hasegawa, Y. Katoh, A. Kohyama, R. H. Jones, and L. L. Snead, *J. Nucl. Mater.*, in press, available online.
- [2] R. H. Jones, *Advanced Ceramic Composites for High-Temperature Fission Reactors*, Nuclear Energy Research Initiative Final Report, Project No. 99-281, U.S. Department of Energy, 2002.
- [3] Y. Katoh, A. Kohyama, T. Hinoki, and L. L. Snead, *Fusion Science Tech.* 44 (2003) 155-162.
- [4] R. Naslain, *Composites Science and Technology* 64 (2004) 155-170.
- [5] L. L. Snead and O. J. Schwarz, *J. Nucl. Mater.* 219 (1995) 3-14.
- [6] Y. Katoh, M. Kotani, H. Kishimoto, W. Yang, and A. Kohyama, *J. Nucl. Mater.* 289 (2001) 42-47.

- [7] M. Itoh, K. Iwata, M. Kobayashi, R. Takeuchi, and T. Kabeya, *Macromolecules* 31 (1998) 5609–5615.
- [8] M. Narisawa, M. Nishioka, K. Okamura, K. Oka, and T. Dohmaru, *Ceramic Transactions* 144 (2002) 173-180.
- [9] S. Yajima, K. Okamura, T. Matsuzawa, Y. Hasegawa, and T. Shishido, *Nature* 279 (1979) 706-707.
- [10] T. Ishikawa, Y. Kohtoku, K. Kumagawa, T. Yamamura, and T. Nagasawa, *Nature* 391 (1998) 773-775.
- [11] Y. Katoh, A. Kohyama, S. M. Dong, T. Hinoki, and J-J. Kai, *Ceramic Engineering and Science Proceedings* 23, Issue 3 (2002) 363-370.
- [12] R. Yamada, T. Taguchi, and N. Igawa, *J. Nucl. Mater.* 283-287 (2000) 574-578.
- [13] T. Nozawa, K. Ozawa, Y. Katoh, and A. Kohyama, *Mater. Trans.* 45 (2004) 307-310.

A NEW APPROACH TO JOINING SiC/SiC COMPOSITES—C. H. Henager, Jr. (Pacific Northwest National Laboratory)¹

OBJECTIVE

The objective of this task is to develop a suitable joining method for SiC/SiC composites that retains the strength and toughness of the composite material, is low-activation, is easily applied, and can be used in the field for repairs, if required.

SUMMARY

A new approach to joining SiC-based ceramics is described and evaluated for Fusion Energy systems. The joining method is based on pre-ceramic polymers filled with reactive and inert filler powders and is similar to other approaches that use such materials. This approach differs in the particular polymer system and in the details of the processing. A principal advantage of this approach relative to other, similar approaches is that the polymer system is easily handled in ambient air and can be processed in air. This makes the joining process simple and field repairable. The joining compound is a liquid that can be painted, sprayed, or applied by dip coating.

PROGRESS AND STATUS

Introduction

Prior to this new approach, ceramic joining of SiC composites at PNNL either made use of solid state displacement reactions [1,2] or pre-ceramic polymers based mainly on polycarbosilane [3-7]. Both of these approaches were used to make strong joints between monolithic SiC, with joining of SiC/SiC composites being more problematic due to surface morphology considerations. However, both of these approaches suffer from requiring inert environments for handling and/or processing, which is less desirable compared to air handling. Thus, a new polymer system was found so that joining could be performed in air. Others have also attempted this, with varying success [8,9].

A polysiloxane polymer, polyhydridosiloxane (PHMS), from Gelest, Corp. is used as the pre-ceramic polymer for this work [10]. It converts to SiO₂ starting at 600 C and is completely converted at 1200 C in air. The backbone Si is bonded to hydrogen and a methyl group, in addition to the Si-O bonds that form the polymer chain. The hydrogen is readily removed and can be substituted with OH or with any number of organic groups, such as an ethoxy group or larger hydrocarbon groups. Doing so adds carbon to the resulting pyrolysis product so that a Si-O-C glass forms. The oxygen-carbon ratio is also sensitive to the processing environment and pyrolysis in nitrogen or argon results in higher carbon retention. At higher temperatures, SiO₂ and SiC are formed as crystalline phases and the SiO₂:SiC ratio can also be manipulated. Thus, this polymer is an attractive joining candidate for SiC-composites.

However, approximately 5% mass loss accompanies the pyrolysis and glass phase formation. This results in several percent linear shrinkage of the polymer on pyrolysis, which will either cause high residual tensile stresses in the joint or, more likely, will fracture the joint during pyrolysis and cool-down. To offset these shrinkage stresses, Greil [11] understood that reactive filler powders could expand enough on conversion in air or nitrogen to accommodate these shrinkages and, thus, form near-net shape ceramics using pre-ceramic polymers. We follow this route, partly, and make use of Al, alumina, and silicon carbide powders to make ceramic joints. The use of Al is not as desirable as SiC due to activation concerns but Al promotes the formation of SiC in the joint, which can help adhesion.

¹Pacific Northwest National Laboratory (PNNL) is operated for the U.S. Department of Energy by Battelle Memorial Institute under contract DE-AC06-76RLO-1830.

Experimental Procedure

Powder slurries for joining were prepared by mixing powders, cyclohexane, and PHMS polymer in a standard roller mill. Approximately 50 v/o of the various powders were used to prepare the slurries. The Al powders are flake aluminum powders from AAE, the alumina powders are 2-micron size from Cerac, and the SiC powders are 0.7-micron size from Pred Materials.

The slurries were applied to monolithic Hexaloy SiC blocks that were 20 mm x 6 mm x 3 mm in size. Two blocks were joined using the slurry such that a 2 mm overhang at either end was present so that a simple shear test specimen was fabricated. The specimen and joint are shown schematically in Fig. 1. Enough slurry compound was applied so that as the blocks were pressed together it formed a uniform layer of joining compound.

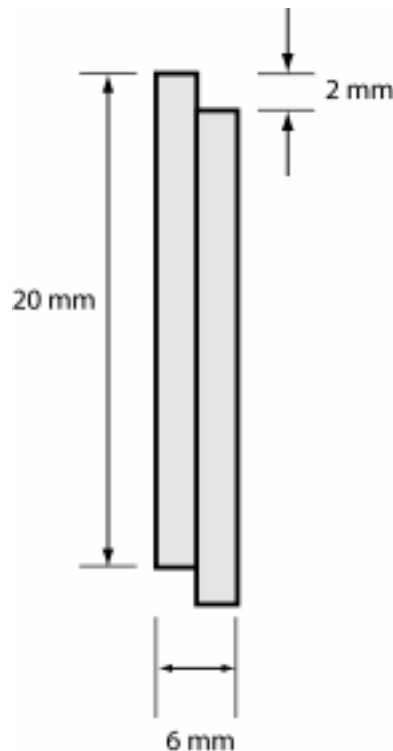


Fig. 1. Schematic of simple shear-lap joint using Hexaloy SiC blocks. The joining compound is applied all along the shared surface of the blocks.

The joints were processed by drying and curing the polymer-powder slurry at 150 C in moist air, which serves to crosslink the polymer. The joined blocks were then pressed normal to the joint at approximately 1 MPa pressure and heated to 1200 C in air for 1 hour. The joints were examined with an SEM. They were then tested at room temperature for shear strength as an indication of joint strength.

Results

Figure 2 shows the joint strength as a function of joint composition and processing conditions. Joints made with SiC powders and processed at 1200 C had the highest strength, 22 MPa in shear. The Al/SiC-filled joint also exhibited good strength at 14.5 MPa. The Al/Al₂O₃-filled joint had a lower strength and the joint processed without applied pressure during pyrolysis was very weak.

The SEM photos of this joint show in Fig. 3 that densification was good and that only minimal pressure is required to achieve a relatively dense joint. Figure 4 shows that without applied pressure that the joint density is low. Note the porosity of the Al/SiC joint processed without applied pressure.

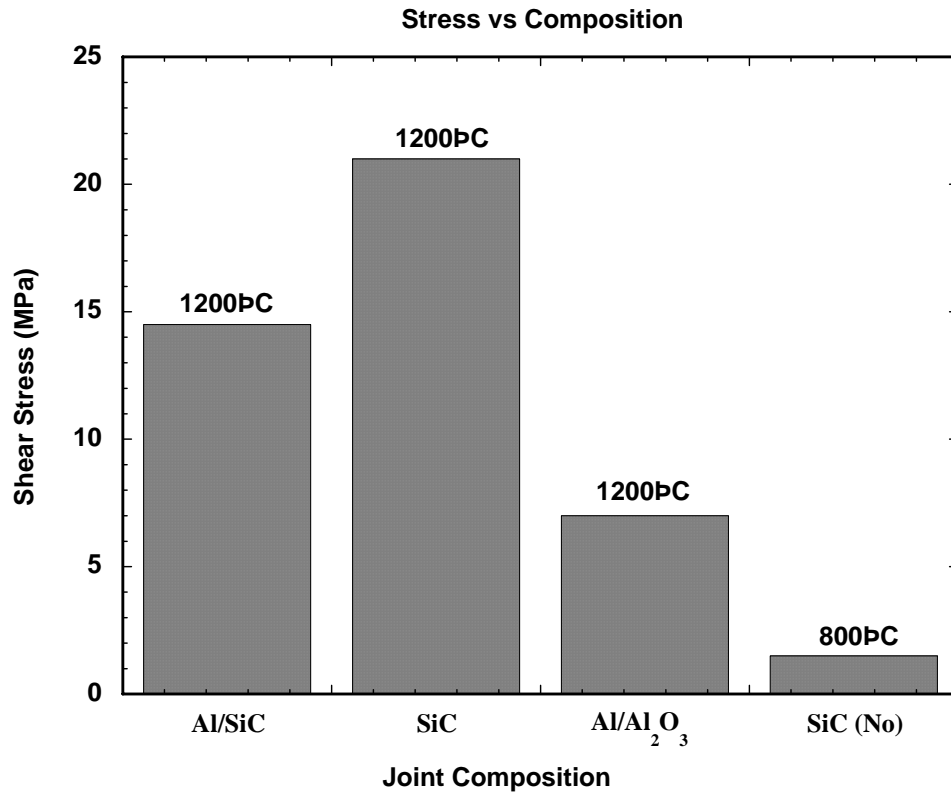
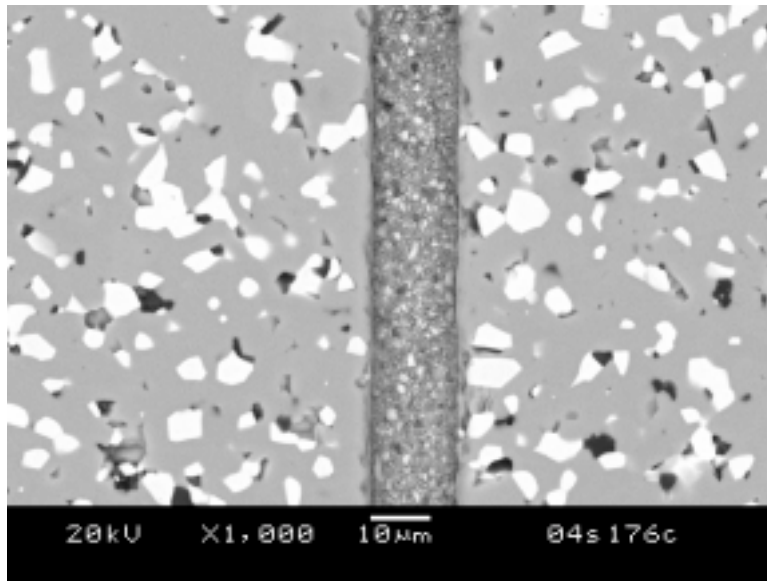
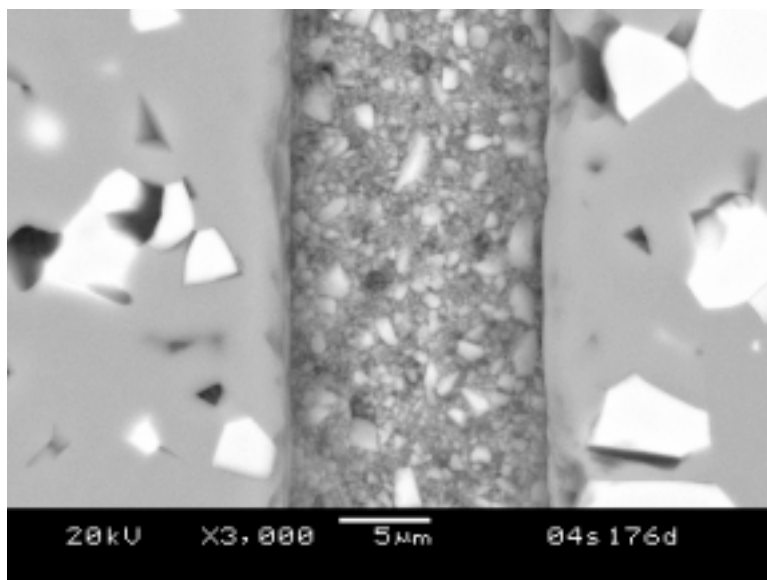


Fig. 2. Shear strength results for joints prepared at 1200 C with minimal pressure and one joint prepared at 800 C with no applied pressure.



(a)



(b)

Fig. 3. SEM photos of SiC-filled preceramic polymer joint at two different magnifications.

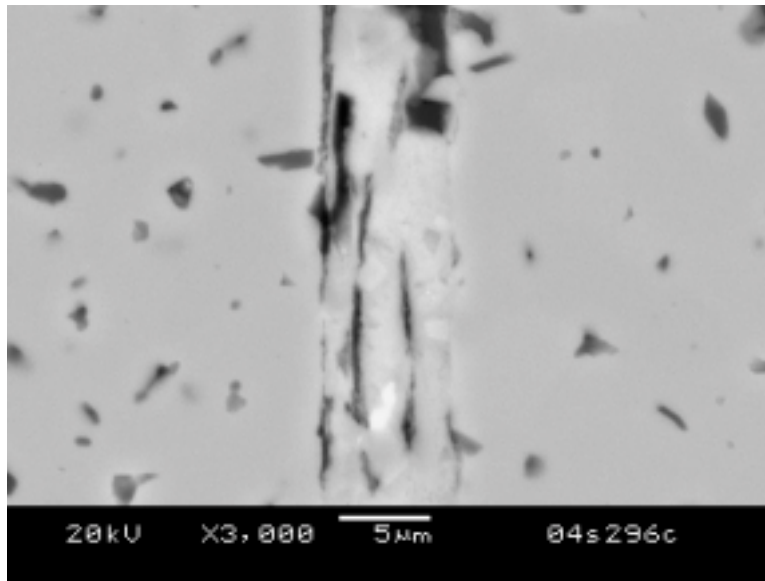


Fig. 4. SEM photo of Al/SiC-filled preceramic polymer joint.

Discussion

This work demonstrates a new approach to joining SiC-based materials for Fusion by emphasizing low-cost processing in air. While others have joined SiC using similar polymers, this is the first use of PHMS and the first to use processing in air. The advantages of PHMS are that we can control the Si-O-C ratios in the final pyrolysis product and that SiC is produced during pyrolysis. The use of Al powders assists in the production of SiC by reducing the Si-O during pyrolysis. However, the formation of Al_2O_3 is not helpful in joining SiC since the two materials are not very reactive. The best results in the present, limited study were obtained using SiC powders in the PHMS polymer. However, strengths were low compared to what have been reported by others. Apparently, the use of applied stress during processing is important and may be required for obtaining strong joints. However, Colombo et al. [12] report that reasonable joints can be obtained with unfilled siloxane polymers at 1200 C. The use of filler powders, which is required to provide shrinkage control, may make the application of pressure necessary.

Future Work

Since advanced ceramic fibers can withstand temperatures higher than 1200 C we plan to explore higher temperature joint processing to take full advantage of the filler powders and interface bonding characteristics of the polymer. Other combinations of filler powders will also be explored.

References

- [1] C. H. Henager, Jr., and R. H. Jones, Joining SiC ceramics using displacement reactions, *Ceram. Trans.* 77 (1997) 117.
- [2] C. Toy, E. Savrun, C. Lewinsohn, and C. Henager, Novel joining compounds in Ti-Si-C system, *Ceram. Trans.* 103 (2000) 561.
- [3] C. A. Lewinsohn and R. H. Jones, Fusion Materials Semiannual Progress Report for the Period Ending June 30, 1998, DOE/ER (1998).
- [4] C. A. Lewinsohn, R. H. Jones, M. Singh, T. Shibayama, T. Hinoki, M. Ando, and A. Kohyama, Methods for joining silicon carbide composites for high-temperature structural applications, *Ceramic Engineering and Science Proceedings* 20 (1999) 119.

- [5] C. A. Lewinsohn, M. Singh, T. Shibayama, T. Hinoki, M. Ando, Y. Katoh, and A. Kohyama, Joining of silicon carbide composites for fusion energy applications, *J. Nucl. Mater.* 283-287, (2000) 1258.
- [6] C. A. Lewinsohn, R. H. Jones, T. Nozawa, M. Kotani, Y. Katoh, A. Kohyama, and M. Singh, Silicon carbide based joining materials for fusion energy and other high-temperature structural applications, *Ceramic Engineering and Science Proceedings* 22 (2001) 621.
- [7] P. Colombo, A. Donato, B. Riccardi, J. Woltersdorf, E. Pippel, R. Silberglitt, G. Danko, C. Lewinsohn, and R. Jones, Joining SiC-based ceramics and composites with preceramic polymers, *Ceramic Transactions* 144 (2002) 323.
- [8] I. E. Anderson, S. Ijadi-Maghsoodi, O. Unal, M. Nosrati, and W. E. Bustamante, Development of a compound for low temperature joining of SiC ceramics and CFCC composites, *Ceram. Trans.* 77 (1997) 25.
- [9] O. Unal, I. E. Anderson, M. Nosrati, S. Ijadi-Maghsoodi, T. J. Barton, and F. C. Laabs, *Ceramic Joining*, eds. I. E. Reimanis, C. H. Henager, and A. P. Tomsia, The American Ceramic Society, Westerville, Ohio, USA. 85 (1997).
- [10] Y. D. Blum, H. P. Chen, D. B. Macqueen, and S. M. Johnson, Modifications of preceramic polymers suitable for corrosion resistant and high temperature coatings, *Materials Research Society Symposium Proceedings* 576 (1999) 281.
- [11] P. Greil, Active-filler-controlled pyrolysis of preceramic polymers, *J. Amer. Ceram. Soc.* 78 (1995) 835.
- [12] P. Colombo, V. Sglavo, E. Pippel, and J. Woltersdorf, Joining of reaction-bonded silicon carbide using a preceramic polymer, *J. Mater. Sci.* 33 (1998) 2405.

STRENGTH AND ELASTIC MODULUS OF NEUTRON-IRRADIATED CUBIC SILICON CARBIDE

—Y. Katoh and L. L. Snead (Oak Ridge National Laboratory)

OBJECTIVE

The objective of this task is to determine the influences of neutron irradiation on fracture strength parameters, including apparent strength, indentation hardness, fracture toughness and elastic modulus, of high-purity chemically vapor-deposited cubic silicon carbide.

SUMMARY

Mechanical properties of high purity polycrystalline cubic silicon carbide were characterized after neutron irradiation. The materials were irradiated in target position capsules in High Flux Isotope Reactor to nominal neutron fluence levels of up to 7.7 dpa at temperatures of 300, 500 and 800°C. Reduction in Young's modulus was observed after irradiation, and its irradiation temperature dependence agreed qualitatively with calculated modulus change due to point defect swelling. Irradiation caused very significant modification of statistical flexural strength but caused only minor increase in nano-indentation hardness. It was pointed out that the irradiation effect on fracture initiation through an enhanced cleavage resistance in large grains could be contributing to the major change in flexural strength properties.

PROGRESS AND STATUS

Introduction

Cubic silicon carbide (SiC), or beta-phase of SiC, is the primary constituent of advanced SiC fiber-reinforced SiC-matrix ceramic composites (SiC/SiC composites) which are considered for use in fusion blanket / first wall structures [1] and other advanced gas-cooled nuclear reactors [2]. For example, both the matrices and the reinforcing fibers comprise of polycrystalline cubic SiC in so-called advanced fiber CVI (chemically vapor-infiltrated) SiC/SiC composites, which are reference materials for fusion- and nuclear-grade SiC-based composites [1]. Matrices of these composites are essentially chemically vapor deposited (CVD) cubic SiC, since the CVI process for matrix densification is in principle a low temperature (deposition temperature of 950~1200°C) CVD of SiC on fiber surfaces as the substrates [3]. The matrix of developmental NITE (nano-infiltration and transient eutectic-phase process) SiC/SiC composite is primarily cubic SiC, because the matrix phase is liquid phase-sintered SiC reprecipitated at below 1800°C [4]. The advanced near-stoichiometric SiC fibers also consist of cubic SiC crystal grains along with a few mass percents of excess carbon, which presents as graphitic pockets at multi-junctions of SiC grains. Such fibers are represented by Tyranno™-SA (Ube Industries, Ltd., Ube, Japan) [5] and Hi-Nicalon™ Type-S (Nippon Carbon Co., Tokyo, Japan) [6], both commercially available.

SiC has long been proposed for use in coated fuel particles for gas-cooled thermal reactors. In the TRISO coating system [7], the SiC layer provides primary ability to contain the high pressure generated in the kernel regions by nuclear fission. In the standard TRISO coating condition at Oak Ridge National Laboratory, SiC-CVD in a fluidized bed at a deposition temperature of ~1500°C produces cubic SiC with typical grain size of ~10 microns at the outside surface.

In all of the above-mentioned application, understanding the effect of neutron irradiation on mechanical properties of cubic SiC is of crucial importance. The matrix micro-cracking stress for SiC/SiC composites, which roughly corresponds to both static and dynamic fatigue limits [8], can be subject to irradiation effect through modification of fracture energy and elastic moduli of the composites' constituents [9]. Statistical fracture strength of monolithic SiC is directly relevant to statistical probability of coating failure for fuel particles [10]. Limited amount of data on irradiated fracture strength support that little or no strength degradation occurs in CVD-produced SiC during neutron irradiation [11-13]. However, some of the published data are contradictory [14], probably because of that the strength of brittle ceramics can be sensitively affected by irradiation behavior of very small amount of second phases and modification of surface conditions during irradiation. Additionally, quality of data could have been sacrificed by the limitation in number and size of specimens accommodated in irradiation capsules, due to the inherently statistical nature of fracture behavior of ceramics and the limited applicability of conventional test techniques. Therefore, in the present work, the influences of irradiation at temperatures of 300 – 800°C on fracture strength parameters, including strength, hardness and elastic modulus, were evaluated exclusively for identical material.

Experimental Details

Material used was CVD-SiC produced by Roam and Haas Advanced Materials Co. (formerly Morton International, Woburn, MA, 'R&H' hereafter). The R&H CVD-SiC is a single-phase cubic SiC with manufacturer-claimed purity of >99.9995%. Typical concentrations of trace element impurities are provided elsewhere [15]. The amount of nitrogen has not been published, although it can be the impurity with highest concentration. The crystal grains of CVD-SiC are highly elongated along the growth direction and have a bi-modal size distribution of large (10~50 μm in column width) and small (typically 1~several μm) grains. Typical examples of optical micrographs of polished and etched cross-sections are found in reference [16]. The crystal grains are heavily faulted and have a preferred crystallographic orientation of <111> direction in parallel to the CVD-growth direction but randomly oriented in the normal plane. All the flexural specimens were machined so that the longitudinal directions are normal to the growth direction. Slight difference in average flexural strength for specimens with longitudinal directions parallel and normal to the growth direction has been reported for the identical material [17].

Neutron irradiation was carried out in the flux trap of the High Flux Isotope Reactor (HFIR) at Oak Ridge National Laboratory (ORNL) for 8 operation cycles. The neutron fluence and temperatures were $6.0 \times 10^{25} \text{ n/m}^2$ ($E > 0.1 \text{ MeV}$) at 300 and 500°C and $7.7 \times 10^{25} \text{ n/m}^2$ ($E > 0.1 \text{ MeV}$) at 800°C. The target temperature was maintained within $\pm 10^\circ\text{C}$ of the designated temperature for the most time. A neutron fluence of $1 \times 10^{25} \text{ n/m}^2$ ($E > 0.1 \text{ MeV}$) will be assumed equivalent to 1dpa in SiC hereafter.

Elastic modulus and hardness were evaluated by means of ultra-low load depth-sensing indentation, on diamond-finished surfaces, using Nano-Indenter™ XP (MTS Systems Corp., Minneapolis, MN) equipped with a Berkovich diamond tip. Elastic modulus and hardness for individual indentation were obtained by averaging slightly depth-dependent indentation modulus and contact pressure measured in a continuous stiffness measurement (CSM) mode [18] over the contact depth range of 500 – 1000nm. Indentation was made at 20 different locations on each sample, which were randomly selected and separated at least 100 μm each other.

Flexural test was performed using rectangular beam specimens with dimensions of 1x1x25 (width x height x length in millimeter) in a four point - 1/3 point configuration, defined in ASTM Standard C1341-00, with support / loading spans of 20 / 6.67mm, respectively, and in otherwise following general guideline of ASTM Standard C1161-02C. Details of the flexural test procedure are found elsewhere [13]. Fracture origins were located by optical microscopy and the fracture surfaces were examined by scanning electron microscopy for selected specimens.

Results and Discussion

(1) Elastic Modulus

The dynamic nano-indentation elastic modulus profiles measured for samples irradiated at 300, 500 and 800°C are plotted in Fig. 1 (A) against contact depth after averaging. Unrealistically high apparent moduli at contact depth smaller than ~200nm approached to literature value of ~460GPa for unirradiated SiC at contact depth of 1000nm. In all the measurements, elastic moduli seemed to be approaching to asymptotic values as the contact depth increased but never reached them at 1000nm. Such behavior is believed to be related with the non-homothetic progressive crack extension during nano-indentation and the influence of indenter tip shape. Park, et al., reports that major median cracks are produced in CVD-SiC by nano-indentation with a Berkovich indenter before the contact depth reaches a few hundreds of nanometers [19].

The influence of neutron irradiation was not very significant but obvious. The measured nano-indentation properties are summarized in Table 1. Swelling data were added from reference [13]. The irradiation at 300°C caused the most significant modulus decrease, while the irradiation at 500 and 800°C resulted in similar and smaller modulus decrease. The difference between 500 and 800°C irradiation was not statistically significant, due probably to relatively large data scatter at 500°C for unknown reasons. Upon

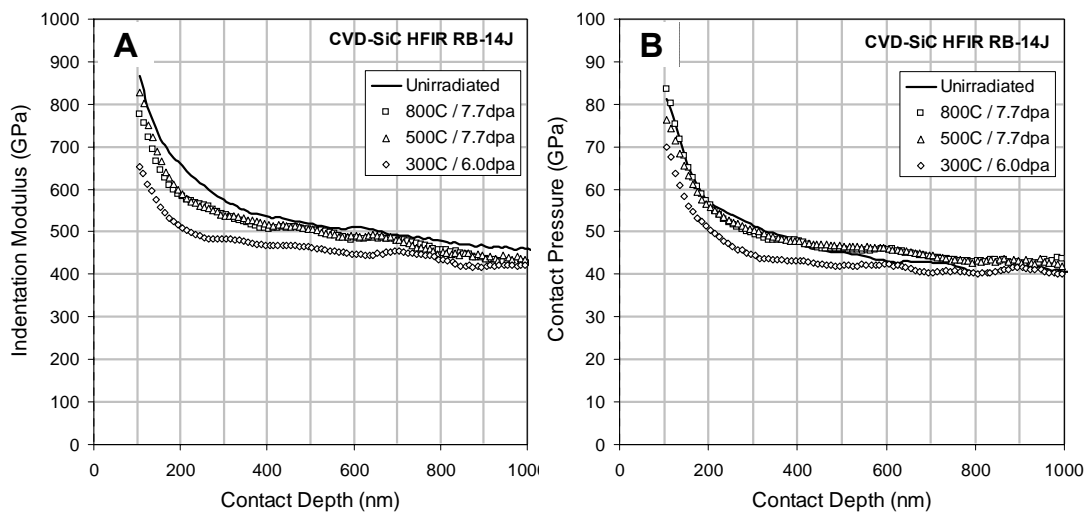


Fig. 1. Depth-profiles of Young's modulus-equivalent dynamic indentation modulus (A) and nano-indentation hardness (B) of unirradiated and irradiated CVD-SiC.

Table 1. Summary of nano-indentation properties

	Elastic modulus (GPa)			Hardness (GPa)			Linear swelling
	Average	Std. dev.	% Change	Average	Std. dev.	% Change	
Unirradiated	456.5	10.4	-	40.6	1.1	-	-
300C, 6.0dpa	416.6	11.9	- 8.7%	40.4	1.0	- 0.5%	0.67%
500C, 6.0dpa	428.5	19.6	- 6.1%	41.7	1.6	+ 2.7%	0.55%
800C, 7.7dpa	426.1	10.8	- 6.7%	42.6	1.4	+4.9%	0.27%

conversion of indentation modulus to Young's modulus, Poisson's ratio of 0.18 was assumed and the potential effect of irradiation on Poisson's ratio was not considered. The influence of minor modification in Poisson's ratio (ν) should be small, as the converted Young's modulus is proportional to $(1-\nu^2)$ [18].

In Fig. 2, irradiation temperature dependence of Young's modulus change is plotted along with published data [11,12,20]. All the modulus data in Fig. 2 were taken by nano-indentation on R&H CVD-SiC samples irradiated to 0.15 – 7.7 dpa. Irradiation generally reduces modulus and the extent of reduction is more significant at a lower irradiation temperature. The modulus reduction becomes negligible when irradiation temperature reaches or exceeds $\sim 1000^\circ\text{C}$. There seems to be an indistinct stage between 800 and 1000°C .

These features in the temperature dependency have been observed for 'point defect swelling' of SiC [21].

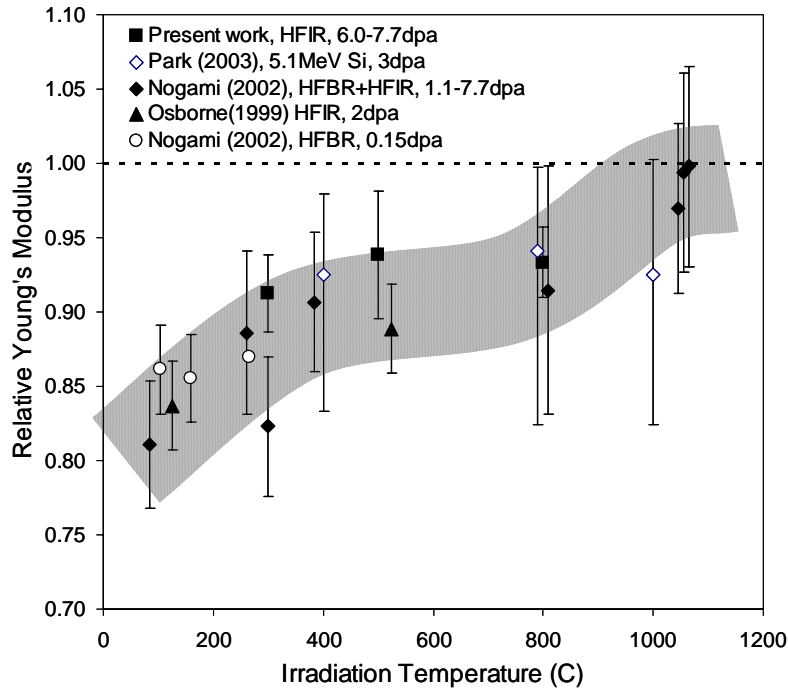


Fig. 2. Irradiation temperature dependence of irradiated Young's modulus of CVD-SiC, at ambient temperature, normalized to unirradiated values. The error bars are showing standard deviations for all the neutron data points and ranges of data scatter for the ion data points.

Point defect swelling is an isotropic volume expansion that is believed to occur by lattice relaxation due to accumulated isolated point defects and small point defect clusters during irradiation at temperatures where vacancies are not readily mobile. In SiC which underwent point defect swelling, a very good agreement of dimensional expansion with lattice spacing has been confirmed by X-ray diffractometry studies [22].

An estimation of the influence of lattice relaxation on Young's modulus was attempted by a calculation using Tersoff potential [23]. The result predicted, as shown in Fig. 3, that linear lattice swelling of 1% causes approximately 10% reduction in Young's modulus. The predicted Young's modulus change could be varied up to tens of percents depending on a selection of interatomic potential, and Tersoff potential gives relatively high sensitivity of modulus to the interatomic distance. Therefore, measured elastic modulus changes observed in this experiment are generally greater than the theoretical prediction. Quantitative reliability of either the nano-indentation modulus or the potential function used is not sufficient for further discussion. Nonetheless, it could be concluded that the lattice expansion is a major cause of the irradiation-induced elastic modulus reduction in SiC.

(2) Hardness and Flexural Strength

The averaged profiles of dynamic indentation hardness are presented in Fig. 1 (B). Similar to the elastic modulus profiles seen in Fig. 1 (A), initially high contact pressures when the contact depth being smaller than ~200nm, they reduces to commonly reported range of 40 – 45 GPa as the contact depth exceeds ~500nm. This contact depth-dependent evolution of apparent hardness could again be attributed to the non-homothetic progressive cracking during indentation and the indenter tip shape effect. The effect of

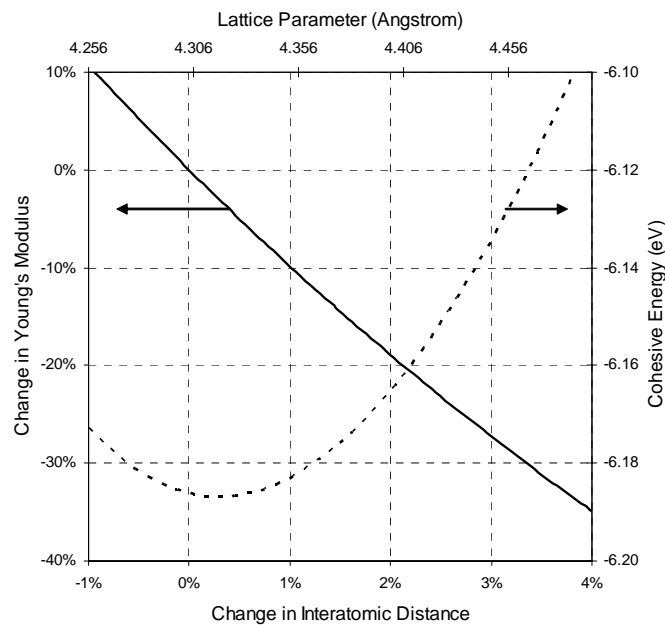


Fig. 3. The influences of interatomic distance change on Young's modulus and cohesive energy of 3C-SiC calculated using Tersoff potential. The cohesive energy is for average of SiC₄ and Si₄C unit tetrahedra.

irradiation on indentation hardness is apparently minor when the hardness is compared at contact depth of ~1000nm. However, as shown in Tab. 1, hardening is statistically significant after irradiation at 500 and 800°C while a potential slight hardness reduction could be observed at 300°C.

Similar but more pronounced trend was observed in the irradiated flexural strength, for which the data are summarized in Table 2. Neutron irradiation at 300°C did not significantly alter the average flexural strength of CVD-SiC, while at 500 and 800°C strengthened by approximately 45 – 50%. Like other brittle ceramics, SiC is believed to obey the Griffith fracture criterion;

$$\sigma_f = (2E\gamma_0/\pi c)^{1/2} \quad (1)$$

where σ_f is fracture stress, E is Young's modulus, γ_0 is effective fracture surface energy, and c is the crack length. According to Eq. (1) and data shown in Tabs.1 and 2, neutron irradiation at 500 and 800°C apparently caused substantial increase of the fracture energy, while at 300°C it may have caused a minor increase of the fracture energy. On the other hand, for brittle ceramics, indentation hardness is generally observed to be proportional to the fracture stress, thus

$$H = n\sigma_f \quad (2)$$

where n typically falls in a range of 20 – 50. This equation gives only a rough trend of common features for ceramics, but the relationship seems reasonable to some extent because both the indentation hardness and the averaged fracture stress are determined primarily by Mode-I fracture toughness. If we assume such a relationship, Eqs. (1) and (2) and data in Tab. 1 gives 8 – 18% irradiation-induced fracture energy enhancement. In this case, the degree of enhancement is positively correlated with the irradiation temperature.

Present and published data regarding the irradiation effects on flexural strength, nano-indentation hardness, and indentation fracture toughness of R&H CVD-SiC in a fluence range of 0.15 – 18.7 dpa are compiled in Fig. 4. The general trend is that the irradiation-induced strengthening or toughening seems to be significant at 300 – 1000°C, in spite of the significant decrease in Young's modulus, which confirms the increase in fracture energy by irradiation.

It is interesting to note that, in Fig. 4, the nano-indentation hardness exhibits relatively small and positive irradiation effect that is insensitive to the irradiation temperature. The width of data band for nano-

Table 2. Summary of flexural strength properties

	Average strength (MPa)	Std. dev. (MPa)	% Change	Weibull modulus	Number of samples
Unirradiated	402	41	-	9.9	25
300C, 6.0dpa	419	85	+4	5.5	10
500C, 6.0dpa	606	66	+51	10.8	20
800C, 7.7dpa	578	85	+44	7.9	29

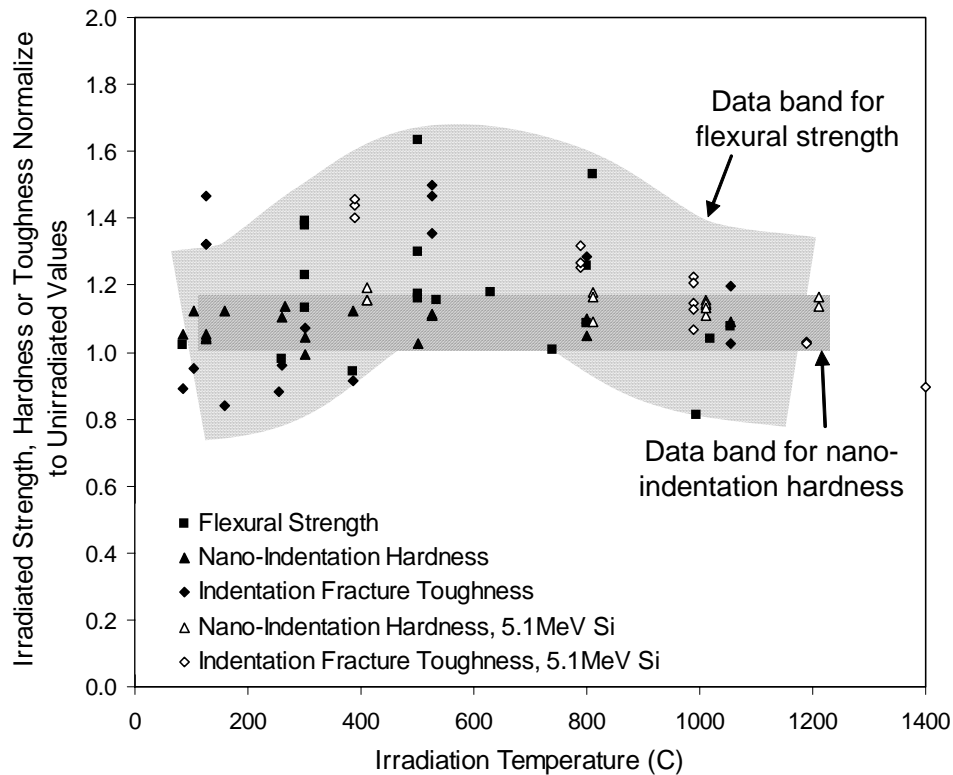


Fig. 4. Plots of fracture strength parameters (flexural strength, nano-indentation hardness and indentation fracture toughness) of CVD-SiC at ambient temperature as a function of irradiation temperature.

indentation hardness is also small, as well as the individual data point represents a set of data which have a small scatter, too. This observation is contrasting to that both the flexural strength and the indentation fracture toughness data indicate a broad peak at an intermediate temperature while accompanying a large scatter.

The large scatter in flexural strength of brittle ceramics is inevitable, since the fracture strength is determined by the effective fracture toughness and morphology and characteristics of the flaw that caused the fracture. Irradiation possibly modifies both the flaw characteristics and the fracture toughness, through potential surface modification, relaxation of the machining-induced local stress, modifications of elastic properties and fracture energy. Because of such a complex nature of the apparent fracture strength, flexural strength measurement may not be an appropriate experimental technique for irradiation effect studies of ceramics for purposes other than engineering data generation. On the other hand, nano-indentation hardness is not affected by potential modification to the surfaces and surface features, because the indentation is usually performed to surfaces polished after irradiation. Nano-indentation hardness is determined primarily by the dynamic crack extension resistance mostly in bulk, though near surface, and therefore should be more relevant to fracture toughness. The disadvantage is in that the irradiation effect can possibly be deemphasized due to the residual stress in subsurface introduced during

polishing, in addition to the difficulty in relating the hardness with more commonly accepted strength parameters.

The scatter for indentation fracture toughness plots is caused probably by both the surface effect and the lack of standard experimental procedure. The indentation should be applied on sufficiently polished surfaces, but conditions of polishing are not always provided in literature [12,20]. Crack length measurement is done in either an optical microscope, a conventional SEM or a field emission SEM, all of which gives very different crack visibility. In addition, a few different models have been used for derivation of fracture toughness. As a conclusion, indentation fracture toughness measurement is an efficient technique for estimation of irradiation-induced toughness modifications, however, validation of the results requires very careful practice and flawless reporting of the experimental details.

Statistical Strength and Fracture Surfaces

In Fig. 5, Weibull statistical plots of the flexural strength of unirradiated and irradiated samples are presented. By irradiation at 500 and 800°C, Weibull modulus slightly decreased and at the same time the fitted line shifted toward the higher fracture stress direction. The horizontal shift indicates a simple toughening, or an increase in fracture toughness alone [24]. After irradiation at 300°C, Weibull modulus reduction and slight embrittlement, or a decrease in fracture toughness, were observed.

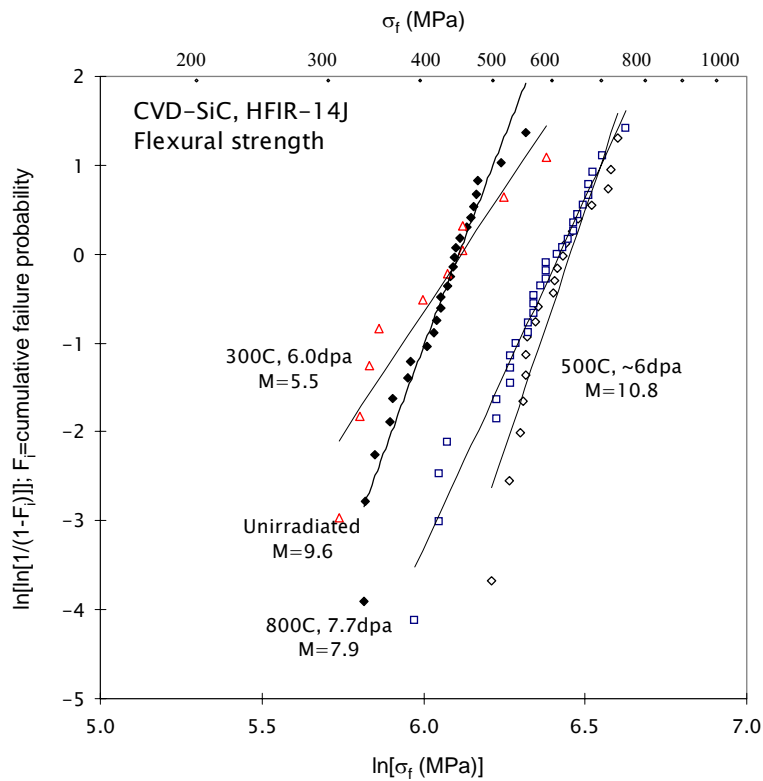


Fig. 5. Weibull plot of flexural strength of unirradiated and irradiated CVD-SiC.

Weibull modulus reduction for fracture strength due to neutron irradiation has been reported for various ceramics. Dienst tried to attribute it to the intrinsic nature of irradiation-produced defect structures, which substitute for the role of flaws responsible for unirradiated fracture, and flaw blunting by local stress relaxation in the high strength domain [14]. The former mechanism could not operate in the present case, because the irradiation produces homogeneously distributed nano-sized defect structures, while the typical flaw sizes which caused fracture in the present experiment are estimated to be 50~100 μm when semicircular surface flaw and K_{Ic} of $\sim 3\text{MPa}\cdot\text{m}^{-1/2}$ are assumed. The flaw blunting is a possible mechanism for the apparent toughening, however, further study is necessary to examine the flaw size-dependence of the blunting efficiency.

For the case of unirradiated CVD-SiC, fracture origin was always at or very close to surface on the tension side. Although the crack initiation site could not always be identified, in 12 of the 13 observed

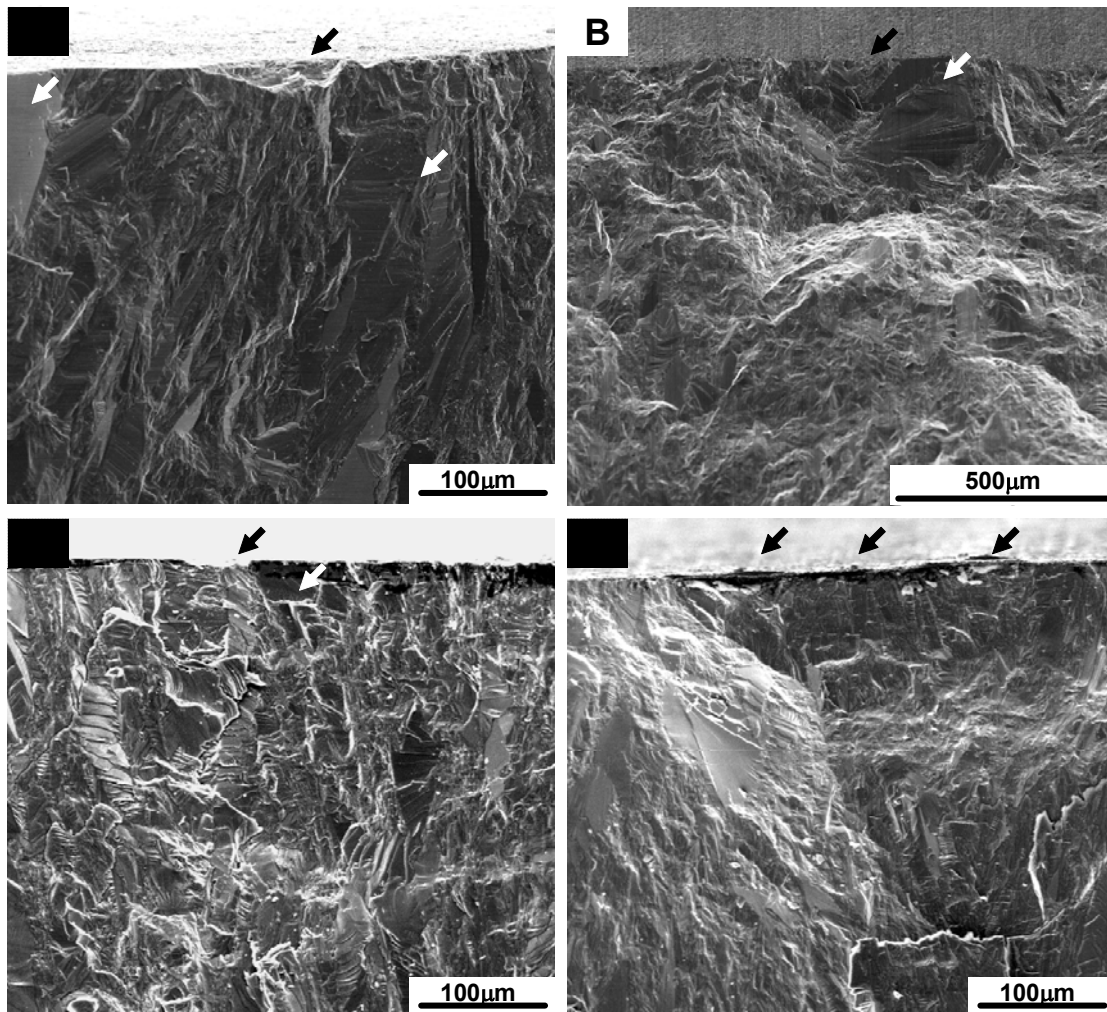


Fig. 6. Fracture origins of flexural tested CVD-SiC samples. (A) unirradiated, $\sigma_f = 480\text{MPa}$, (B) unirradiated, $\sigma_f = 430\text{MPa}$, (C) irradiated to 7.7dpa at 800C, $\sigma_f = 700\text{MPa}$, and (D) irradiated to 7.7dpa at 800C, $\sigma_f = 480\text{MPa}$. Surface flaws and large grains are indicated by arrows in black and white, respectively.

specimens, it was likely to be a combination of a large grain (or large grains) and a machining-induced surface flaw (1 specimen fractured from a large surface flaw). This interpretation is based on observation that the surface flaw found at the fracture origin itself was too small to explain the measured strength and cleavage of a large grain adjacent to the surface flaw was apparent, as shown in Figs. 6 (A) and (B). Fracture initiation at a large grain in R&H CVD-SiC is reported by Vern Cockeram [17]. It is also reported that Coors CVD-SiC, which is free from large grains, exhibits substantially higher fracture strength than R&H CVD-SiC when machining condition is identical [17]. Clean and plain cleavage of large grains frequently observed in the fracture surfaces, as seen in Fig. 7 (A), indicates low fracture energy on preferred crystallographic planes in cubic SiC. Therefore, it is generally supported that the presence of large grains is influencing the strength of R&H CVD-SiC.

For the case of samples irradiated at 800°C, as shown in Fig. 7 (B), cleavage of large grains is not as marked as in unirradiated fracture surfaces. This is because the irradiated transgranular fracture of large grains did not leave surfaces as clean and plane as for the case of unirradiated grains, and hence indicating the increased transgranular fracture energy. It could contribute to increased resistance against both fracture initiation and crack propagation and thus increase fracture strength and indentation hardness. In Fig. 6 (C), which shows a fracture surface of the specimen exhibited high strength ($\sigma_f = \sim 700\text{MPa}$), the probable fracture origins are relatively small surface flaw and the adjacent large grain. In this case, fracture energy increase in the large grain should have increased the fracture stress significantly. On the other hand, when large flaw was nearly exclusively responsible for the fracture as shown in Fig. 6 (D) ($\sigma_f = \sim 480\text{MPa}$), the irradiation effect on fracture stress should have not been very significant. The Weibull modulus reduction by irradiation can thus be accounted by the reduced contribution of large grains when fracture strength is controlled by the combined effect of surface flaw and large grains.

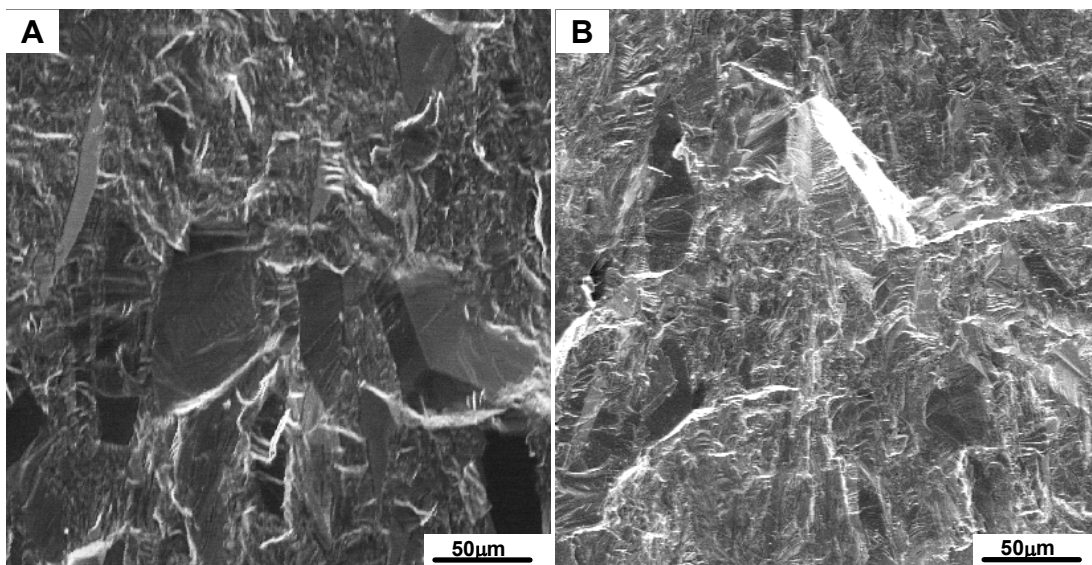


Fig. 7. Fracture surfaces showing the typical differences in cleavage surface fraction and appearance between unirradiated (A) and 800°C-irradiated specimens.

Future Work

This work will be continued in order to better understand the effects on neutron irradiation on fundamental mechanical and physical properties of SiC. Young's modulus of neutron-irradiated CVD SiC will be determined with improved accuracy by impulse excitation and vibration method. Statistical fracture strength experiment will be carried out in near future irradiation opportunity. Determination of irradiated fracture toughness of CVD SiC is also planned employing dedicated notched beam specimens.

References

- [1] Y. Katoh, A. Kohyama, T. Hinoki, and L. L. Snead, *Fus. Science Tech.* 44 (2003) 155-162.
- [2] A. Kohyama and Y. Katoh, presented at the 27th Annual Cocoa Beach Conference on Advanced Ceramics and Composites, January 26-31, 2003, Cocoa Beach, Fla.
- [3] K. J. Probst, T. M. Besmann, D. P. Stinton, R. A. Lowden, T. J. Anderson, and T. L. Starr, *Surface and Coating Technology* 120-121 (1999) 250-258.
- [4] Y. Katoh, S. M. Dong, and A. Kohyama, *Ceram. Trans.* 144 (2002) 77-86.
- [5] T. Ishikawa, Y. Kohtoku, K. Kumagawa, T. Yamamura, and T. Nagasawa, *Nature* 391 (1998) 773-775.
- [6] M. Takeda, J. Sakamoto, A. Saeki, and H. Ichikawa, *Ceramic Engineering and Science Proceedings* 17, No. 4 (1996) 35-42.
- [7] R. J. Price, *Nucl. Tech.* 35 (1977) 320-336.
- [8] S. Zhu, M. Mizuno, Y. Kagawa, and Y. Mutoh, *Comp. Science Tech.* 59 (1999) 833-851.
- [9] W. A. Curtin, *J. Amer. Ceram. Soc.* 74 (1991) 2837-2845.
- [10] G. K. Miller and D. C. Eadsworth, *Nucl. Tech.* 110 (1995) 396-406.
- [11] M. C. Osborne, J. C. Hay, L. L. Snead, and D. Steiner, *J. Amer. Ceram. Soc.* 82 (1999) 2490-2496.
- [12] S. Nogami, A. Hasegawa, and L. L. Snead, *J. Nucl. Mater.* 307-311 (2002) 1163-1167.
- [13] L. L. Snead, T. Hinoki, and Y. Katoh, *Fusion Materials*, DOE/ER-0313/33 (2002) 49-57.
- [14] W. Dienst, *J. Nucl. Mater.* 211 (1994) 186-193.
- [15] <http://www.cvdmaterials.com/silicon.htm>
- [16] <http://www.udri.udayton.edu/DLCM>
- [17] B. Vern Cockeram, *J. Amer. Ceram. Soc.* 85 (2002) 603-610.
- [18] W. C. Oliver, and G. M. Pharr, *J. Mater. Res.* 7 (1992) 1564-1583.
- [19] K. H. Park, Y. Katoh, and A. Kohyama, *Journal of Nuclear Materials*, submitted.
- [20] K. H. Park, Dissertation, Kyoto University, 2004.
- [21] Y. Katoh, H. Kishimoto, and A. Kohyama, *J. Nucl. Mater.* 307-311 (2002) 1221-1226.
- [22] Y. Pramono, M. Imai, and T. Yano, *J. Nucl. Science Tech.* 40 (2003) 531-536.
- [23] J. Tersoff, *Physical Review B* 39 (1989) 5566-5568.
- [24] K. Kendall, N. McN. Alford, S. R. Tan, and J. D. Birchall, *J. Mater. Res.* 1 (1986) 120-123.

MODELING THE TRANSVERSE THERMAL CONDUCTIVITY OF 3D-SiC_f/SiC COMPOSITES—G. E. Youngblood and R. H. Jones (Pacific Northwest National Laboratory)* and Reiji Yamada (JAERI, Tokaimura, JP)

OBJECTIVE

The primary objective of this task is to assess the thermal conductivity of SiC/SiC composites made from SiC fibers (with various SiC-type matrices, fiber coatings and architectures) before and after irradiation and to develop analytic models that describe the transverse and in-plane thermal conductivity of these composites as a function of constituent properties and geometry as well as temperature and dose.

SUMMARY

Our previously developed hierarchical two-layer (H2L) model was modified to describe the effective transverse thermal conductivity (K_{eff}) of a three-dimensional (3D) SiC/SiC composite plate made with cross-layered and Z-stitched X:Y:Z uniaxial fiber tow sub-units. As before, the model describes K_{eff} in terms of constituent, microstructural and architectural properties that include the expected effects of fiber-matrix interfacial conductance, of high fiber packing fractions within individual tow sub-units and of the non-uniform porosity contents, shapes and orientations within these sub-units. Model predictions were obtained for two versions of a 3D-Tyranno SATM/PyC/ICVI-SiC composite that had similar fiber/matrix pyrocarbon (PyC) interfaces, relatively high bulk densities (~2.88 g/cc), and an X:Y configuration with fiber content ratios 1:1. The only major difference between the two versions was their Z-stitch fiber content where the relative fiber ratios were 0.1 and 1.2 in the Z sub-units.

PROGRESS AND STATUS

Introduction

In previous work, the hierarchical two-layer (H2L) model for the effective transverse thermal conductivity (K_{eff}) of 2D-SiC/SiC was used to predict K_{eff} for various composites made with Hi-NicalonTM, Hi-NicalonTM type S or TyrannoTM SA fabric layers and CVI-SiC matrix components [1]. The model included the effects of the interfacial conductance, which in a composite with numerous fiber/matrix (f/m) interfaces can have a profound influence on K_{eff} . In particular, the f/m interface in a 2D-SiC/SiC composite, especially if it is pyrocarbon (PyC), might be vulnerable to radiation degradation. In this case, the fibers could be thermally decoupled from the matrix, and K_{eff} likely would be decreased, perhaps severely. The H2L-model also included the effects of porosity content, shape and orientation, which are not expected to be affected by irradiation.

In this work, the H2L-model was modified to describe $K_{\text{eff}}(T)$ for a 3D-SiC/SiC. A 3D-SiC/SiC is envisioned as having numerous fibers aligned in the direction of the heat conduction, say the Z-direction, which could provide a “heat pipe” effect to increase K_{eff} . Furthermore, K_{eff} for a 3D-composite with a major portion of the heat conduction determined by fiber “heat pipes” might not be so susceptible to radiation degradation.

The Hierarchical Model Approach

In Fig. 1, a schematic diagram depicts the unit cell for a 3D-SiC/SiC composite plate made with cross-layered and Z-stitched X:Y:Z uniaxial fiber tow sub-units used for this study.

*Pacific Northwest National Laboratory (PNNL) is operated for the U.S. Department of Energy by Battelle Memorial Institute under contract DE-AC06-76RLO-1830.

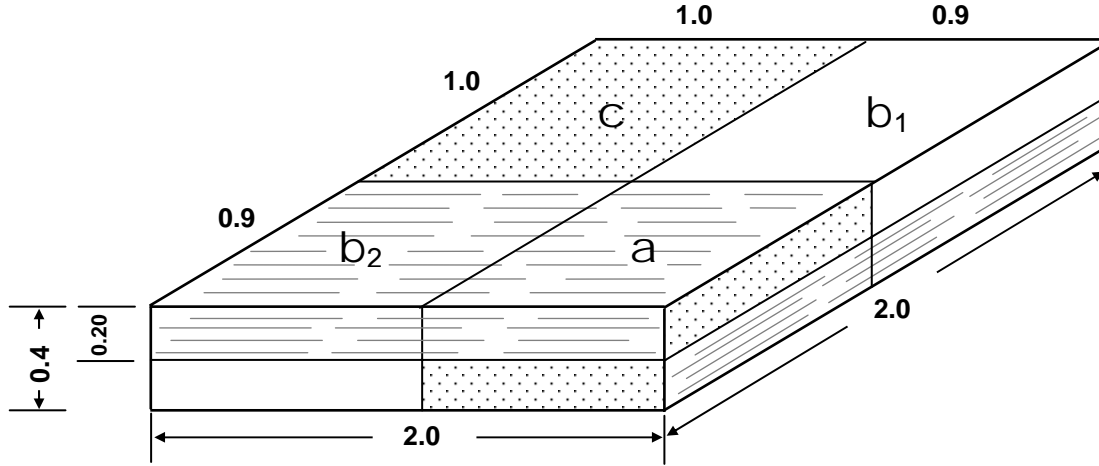


Fig. 1. Schematic of layered and Z-stitched 3D-SiC/SiC unit cell.

A unit cell for this configuration consists of three sub-units: sub-unit “a” contains two identical bars, one on top of another with uniaxial aligned fibers in alternate X:Y directions in a SiC matrix; sub-unit “b” also contains two bars one on top of another but with alternate bars containing either uniaxial aligned fibers in a matrix or no fibers (all matrix material); and sub-unit “c” contains only fibers in the Z-direction within a SiC matrix. There are two equivalent sub-unit “b” cells (b_1 and b_2) per unit cell. A simple parallel heat flow model then approximately describes K_{eff} of such a unit cell, which is made up of three parallel heat paths through sub-unit cells “a, b and c” with transverse area ratios f_a , f_b and f_c and effective thermal conductivities K_a , K_b and K_c , respectively. Thus,

$$K_{eff} = f_a K_a + f_b K_b + f_c K_c \quad (1),$$

within the limits of assuming adjoining parallel, non-interacting 1D conduction paths. The thermal conductivities of the three sub-unit cells are given by:

$$K_a = K_m [(1 - P_a)/(1 + \beta_a P_a)] f_a (HJ) \quad (2),$$

$$1/K_b = 0.5/K_a + 0.5/K_{b'} \quad (\text{series heat flow through adjoining layered bars}) \quad (3),$$

$$K_c = f_{Fc} K_f + f_{Mc} K_m \quad (\text{parallel heat flow through fiber and SiC matrix}) \quad (4).$$

In Eq. (2), the term in brackets is the Maxwell-Eucken thermal conductivity porosity correction where P_a and β_a are the volume fraction of pores and the pore shape and orientation factors in sub-unit “a” and also in one of the layered bars in sub-unit “b”, respectively [2]. Also in Eq. (2), $f_a(HJ)$ is the Hasselman-Johnson expression[#] for treating the effect of the f/m interfacial thermal conductance on K_a , or on K_b in the other layered bar in sub-unit “b”. In Eq. (3), $K_{b'}$ is the thermal conductivity of the layered bar with all SiC matrix and only a single, fairly large flat pore oriented with its flat surface perpendicular to the heat flow direction and located approximately in the middle of the bar. This pore remains after CVI deposits a SiC layer onto the surrounding fiber tows, but leaves a central gap between SiC surfaces advancing from all directions. Thus, $K_{b'} = K_m [(1 - P')/(1 + \beta' P')]$, where P' is the volume fraction of the single flat pore and β' is its shape and orientation factor. In Eq. (4), f_{Fc} and f_{Mc} are the volume fractions of Fiber

[#] $f_a(HJ) = [1 - (A/B)f_p][1 + (A/B)f_p]^{-1}$ with $A = 1 + K_f/ah + K_f/K_m$ and $B = 1 + K_f/ah - K_f/K_m$ where ah is the product of the fiber radius a and the f/m interfacial conductance h [2].

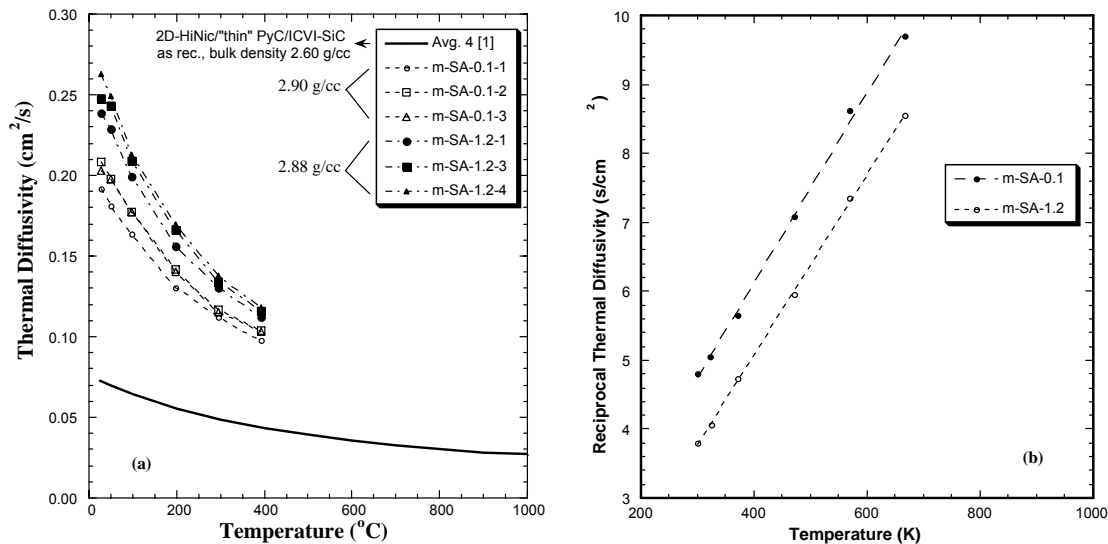
and Matrix in sub-unit “c”, respectively. Importantly, for the analysis of the 3D-SiC/SiC composite considered here, f_{Fc} and f_{Mc} are the only two parameters that differ between the two versions.

Specimens Tested

Disc-shaped 3D-SiC/SiC specimens (nominally 10-mm diameter x 3-mm thick) were provided by Reiji Yamada and made with X:Y:Z fiber contents 1:1:0.09, 1:1:0.2, 1:1:0.45, and 1:1:1.23, respectively. The fibers were Tyranno™ SA, and the SiC matrix was made by isothermal CVI. A thin PyC coating was applied to the SA-preforms prior to CVI. A full description of preparation and measured thermal diffusivity and conductivity values from RT up to 1000°C for a similar set of samples is given in Ref. [3]. From this set of samples, six discs, three with Z-stitch contents 0.09 and three with contents 1.23, were selected for detailed microstructural and additional thermal analysis. Using the laser flash technique, thermal diffusivity measurements were performed on all six discs in air from RT up to 400°C by methods described previously [4].

Results and Discussion

In Fig. 2(a), the thermal diffusivity values measured at PNNL are presented for the six selected 3D-SiC/SiC specimens made with layered and Z-stitched Tyranno™ SA fiber tow and ICVI-SiC matrix sub-units. For comparison, the average thermal diffusivity determined for a 2D-SiC/ICVI-SiC made with woven Hi-Nicalon™ fabric layers (thin PyC interface) also is shown [5]. In Fig. 2(b), the average reciprocal thermal diffusivity values for the two versions of 3D-SiC/SiC are given as a function of temperature based on the data shown in Fig. 2(a).

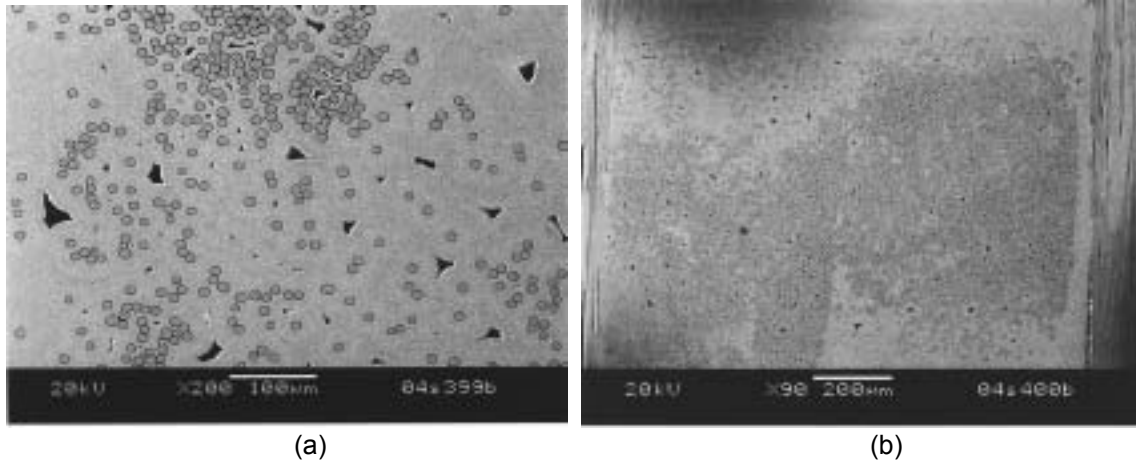


Figs. 2(a-b). (a) Thermal diffusivity of 3D-Tyranno SA/ICVI-SiC composites with X:Y = 1:1 and Z ~ 0.1 or 1.2, and (b) average reciprocal thermal diffusivity values for each version.

The thermal diffusivity values measured at PNNL over the RT-400°C temperature range match within a few % the values measured and reported previously by Yamada for similar composite compositions [3]. Furthermore, the diffusivity values are about x3 greater than values measured for the 2D-SiC/SiC made with Hi-Nicalon™ fibers [5]. The higher diffusivity values found for the 3D-SiC/SiC composites reflect both the Tyranno™ SA fibers having higher thermal conductivity than the Hi-Nicalon™ fibers and also the “heat pipe” effect of the Z-stitched fibers. A very good linear least squares fit ($R^2 > 0.997$) was made to the Fig. 2(b) data and was used to estimate average values of thermal diffusivity by extrapolation

for temperatures up to 1000°C as previously shown to be fairly reliable [4]. The transverse thermal conductivity $K_{\text{eff}}(T)$ was then determined from the thermal diffusivity data, the measured bulk density values, and the specific heat values of SiC.

In Figs. 3(a-b), typical SEM micrographs show the fiber and pore distribution in a plane perpendicular to sub-unit “c” for the two versions of 3D-SiC/SiC with actual Z-fiber content ratios 0.09 and 1.23, respectively. Note the extremely full infiltration of the SiC matrix within and around the fiber bundles for both versions. Views of other sub-units exhibited similar, uniformly full matrix infiltration.



Figs. 3(a-b). SEM micrographs (backscatter electron mode) of polished cross-sections of the “c” sub-unit cell regions showing the relative fiber packing and SiC matrix infiltration for the (a) X:Y:Z ~ 1:1:0.1 and (b) 1:1:1.23 versions of the 3D-Tyranno SA/ICVI-SiC composites.

In Table 1, dimensional, density and microstructural data determined from several SEM and optical micrographs for the two versions of 3D-SiC/SiC are given.

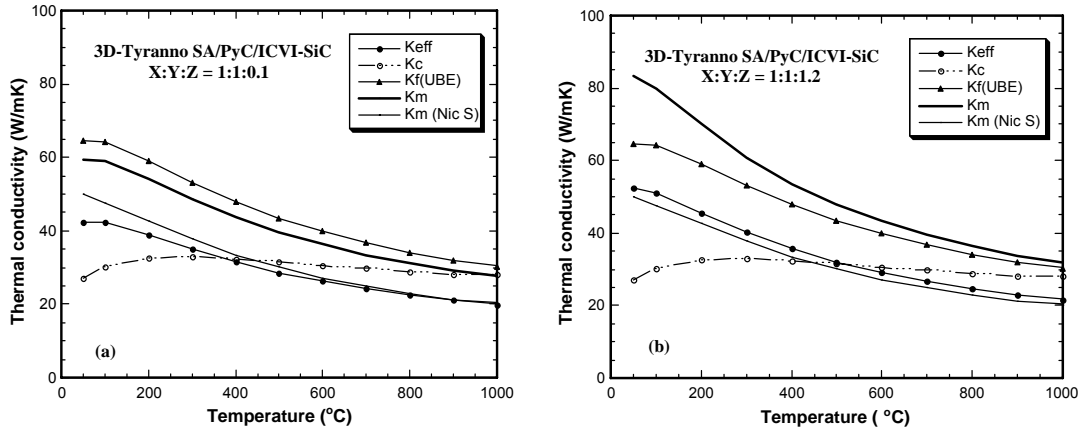
Table 1. Bulk density (ρ_b), dimensional and microstructural data for the 3D-Tyranno™ SA/ICVI-SiC with relative fiber contents X:Y:Z = 1:1:0.09 and 1:1:1.23.

Version	ρ_b (g/cc)	t (μm)	a (μm)	P_a	P'	β_b	f_p	f_{Fc}	f_{Mc}
1:1:0.09	2.88	0.20	5.00	0.090	0.21	5.6	0.52	0.059	0.936
1:1:1.23	2.88	same	same	same	same	same	same	0.513	0.440
Range	± 0.02	± 0.05	± 0.6	± 0.015	± 0.09	± 0.6	± 0.02	± 0.02	± 0.02

In Table 1, because the X:Y structures are the same between the two versions, the only parameters that differ are the fractions of fiber and matrix in the “c” sub-units. Likewise, the Hasselman-Johnson factor for treating the effect of the f/m interfacial conductance is assumed the same for both versions. In Eq. (2), $\beta_a \sim 1$ for the “needle-like” pores parallel to the fibers and perpendicular to the transverse thermal conduction.

In Figs. 4 (a-b), the thermal conductivity values, $K_{\text{eff}}(T)$, $K_c(T)$, and $K_f(T)$, which are input data for our 3D-H2L model, are presented for the two examined SiC/SiC versions with Z ~ 0.1 or Z ~ 1.2, respectively. The model prediction for $K_m(T)$ is then shown as a bolded continuous solid line. For comparison, $K_m(T)$ for a 2D-Nicalon™ type S/PyC/ICVI-SiC composite also is shown [1]. In both these figures, the values of $K_{\text{eff}}(T)$ were calculated from the measured thermal diffusivity data given in

Figs. 2(a-b), the values of $K_c(T)$ taken from Ref. [2], and the values of $K_f(T)$ estimated from data provided by UBE for the Tyranno™ SA fiber.



Figs. 4(a-b). 3D-H2L model predictions for K_m based on measured values of K_{eff} and $K_f(UBE)$, and on values of K_c from Ref. [2] for 3D-Tyranno SA/PyC/ICVI-SiC with (a) X:Y:Z ~ 1:1:0.1 and (b) X:Y:Z ~ 1:1:1.2, respectively. For comparison, K_m for a 2D-Nicalon type S/PyC/ICVI-SiC composite also is shown.

For these two similar composites with X:Y:Z configurations ~ 1:1:0.1 and 1:1:1.2, $K_{eff}(T)$ -values ranged from 42 and 52 W/mK at 50°C down to about 20 and 22 W/mK at 1000°C, respectively. These values of K_{eff} for this 3D-SiC/SiC composite exceed by 25% or more the highest K_{eff} -values reported for 2D-SiC/SiC made by any CVI-process.

The predicted values of $K_m(T)$ were derived by iteration until the model predictions for $K_{eff}(T)$ converged onto the measured $K_{eff}(T)$ -values. It is noted that the $K_{eff}(T)$ -values are rather insensitive to the $K_c(T)$ -values used for these thermally well-coupled composites, so $K_c(T)$ -values obtained previously for well-coupled 2D-SiC/ICVI-SiC composites were used. The predicted $K_m(T)$ -values ranged from 60 W/mK at 50°C down to 28 W/mK at 1000°C for the Z ~ 0.1 version; and from ~80 W/mK at 50°C down to 32 W/mK at 1000°C for the Z ~ 1.2 version. However, the $K_m(T)$ -values should not differ for these two versions with similar ICVI-SiC matrix infiltration. Furthermore, the predicted $K_m(T)$ -values should approximately match the $K_m(T)$ -values determined for the Nicalon™ type S composite with a similar SiC matrix. Finally, if K_{eff} increases with increasing Z-fiber content, K_f should be greater than K_m . Although K_f is slightly larger than K_m for the composite with Z ~ 0.1 fiber content, this definitely is not the case for the composite with Z ~ 1.2 fiber content. The latter case suggests that the $K_f(T)$ -values used in the previous model predictions were too low.

To examine this possibility further, model predictions were repeated by performing iterations while allowing both K_m and K_f to vary until predicted K_{eff} -values matched measured K_{eff} -values, but with the restriction that the K_m and K_f variables must be the same for both composite versions. Such an iteration scheme might be compared to solving two equations with two unknowns in algebra. The results are shown in Fig. 5.

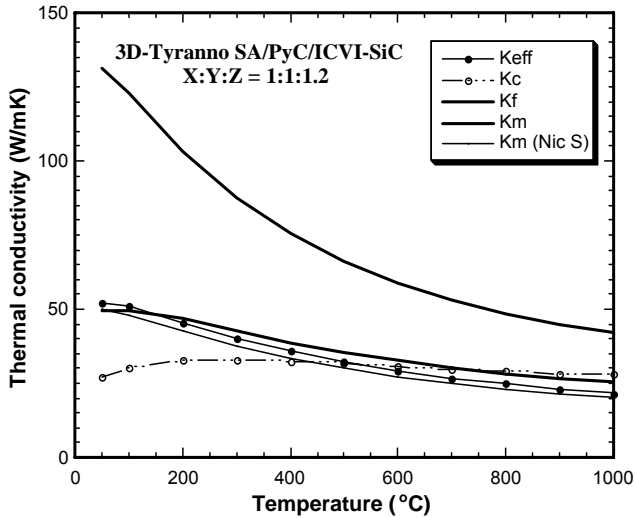


Fig. 5. 3D-H2L model predictions of K_m and K_f based on measured values of K_{eff} and K_c for each version of 3D-Tyranno SA/PyC/ICVI-SiC with $X:Y:Z \sim 1:1:0.1$ or $1:1:1.2$ (only the data for $Z \sim 1.2$ are shown). The iteration scheme required that K_f and K_m have the same values for each version. Again, for comparison $K_m(T)$ -values for a 2D-Nicalon™ type S SiC/SiC composite also are shown.

The predicted $K_m(T)$ -values now range from 50 W/mK at 50°C down to 26 W/mK at 1000°C for both versions (only the data for the $Z \sim 1.2$ case are shown in the figure). Furthermore, the predicted $K_m(T)$ -values now approximately match (within ~ 5 -10%) the $K_m(T)$ -values predicted for the 2D-Nicalon™ type S composite. These two observations strongly suggest that the $K_f(T)$ -values used for the Tyranno™ SA fiber in these two versions of 3D-composite actually have much higher values than the stated $K_f(T)$ -values for bare fiber given by UBE. If this is the case, the thermal conductivity of the Tyranno™ SA fiber in these composites ranges from about 130 W/mK at 50°C down to 42 W/mK at 1000°C, values about twice as high as values for bare fiber.

The thermal conductivity of the sintered Tyranno™ SA fiber has previously been shown to depend quite sensitively on the final heat treatment temperature, which is expected to affect the fiber grain size and the surface roughness [6]. Possibly, the surface roughness is modified by the deposition of a well-bonded CVI-SiC matrix and the effective K_f -value in the composite is increased over that of the bare fiber. This possibility needs to be examined further, as one of the major goals in the SiC/SiC development for fusion applications is to improve K_{eff} . Increasing K_f during composite processing is one way to do that for composite with thermally well-coupled f/m components.

In Table II, according to the 3D-hierarchical model, the relative sensitivity of K_{eff} is given for a 20% change in each parameter listed in Table 1 taken one at a time while the values of the other parameters are held constant.

According to Table II, increasing (or decreasing) K_m - or K_f -values is most important for affecting a change in K_{eff} . Absolute K_m - or K_f -values are quite high for these composites; so increasing these values further would be quite difficult. However, decreasing these values is a distinct possibility in service due to the accumulation of irradiation-induced point defects. In addition, a decrease in h by orders of magnitude can occur because of f/m debonding due to irradiation-induced differential f/m swelling/shrinkage, in which case a relatively large decrease in K_{eff} would be expected. Nevertheless, the “c” sub-units for these 3D-composites with Z-fiber “heat-pipes” would not be subject to the f/m debonding form of thermal conductivity degradation. Therefore, it is reasonable to expect somewhat less degradation in overall K_{eff} for these 3D-composites compared to 2D-composites.

Table 2. Relative sensitivity of K_{eff} at 600° C for 20% change in each listed parameter

Parameter	Value at 600°C	Percent Effect
K_f (W/mK)	58.90	8.7 %
K_m (W/mK)	32.71	10.6 %
K_c (W/mK)	30.60	<0.2 %
t or a	See Table I	<0.2 %
f_p	0.52	1.8 %
P_a	0.090	1.2 %
P_b	0.210	3.6 %
β_b	5.6	2.3 %
f_{M_c} and f_{F_c}	0.440 and 0.513	3.5 %

Experimental Procedures

1. The thermal conductivity K_{eff} determined for a layered and Z-stitched 3D-Tyranno™ SA/PyC/ICVI-SiC composite was about x3 the K_{eff} -value for a conventional 2D-SiC/ICVI-SiC composite made with Hi-Nicalon™ fabric layers. In particular, for the 3D-composites with fiber content ratios X:Y:Z ~ 1:1:1.2, $K_{\text{eff}}(T)$ -values ranged from 52 W/mK at 50°C down to about 22 W/mK at 1000°C.
2. 3D-H2L model predictions suggested that $K_f(T)$ -values for the Tyranno™ SA fibers within an ICVI-SiC matrix are much higher than values observed for bare fiber. In the two composite versions examined here, $K_f(T)$ -values appeared to range from about 130 W/mK at 50°C down to 42 W/mK at 1000°C.
3. 3D-H2L model predictions for $K_m(T)$ ranged from 50 W/mK at 50°C down to 26 W/mK at 1000°C for both versions of 3D-SiC/ICVI-SiC. These values agree with $K_m(T)$ -values predicted for the ICVI-SiC matrix for a 2D-Nicalon™ type S/PyC/ICVI-SiC composite within 5-10%.
4. Because the Z-stitch fiber “heat pipes” in a 3D-SiC/SiC composite are not subject to degradation of K_{eff} due to f/m debonding (thermal decoupling), it is reasonable to expect less susceptibility to radiation degradation of K_{eff} in 3D-composites compared to 2D-SiC/SiC composites.

Results

Model predictions will be carried out for 3D-Tyranno SA/ICVI-SiC composites after irradiation in the HFIR reactor at ORNL as part of the JUPITER 18J test series. Further analyses will be carried out to examine the possibility that for the Tyranno™ SA fiber K_f can effectively have higher values in a CVI-SiC composite than as a bare fiber.

References

- [1] G. E. Youngblood, David J. Senior, and R. H. Jones, Modeling the transverse thermal conductivity of 2-D SiC_f/SiC composites made with woven fabric, *Fus. Sci. Tech.* 45 (2004) 583.
- [2] G. E. Youngblood, D. J. Senior, and R. H. Jones, Optimizing the transverse thermal conductivity of 2D-SiC_f/SiC composites I. Modeling, *J. Nucl. Mat.* 307-311 (2002) 1112.
- [3] R. Yamada, N. Igawa, and T. Taguchi, Thermal diffusivity/conductivity of Tyranno SA fiber- and Hi-Nicalon type S fiber-reinforced 3D-SiC/SiC composites, paper #P-230 presented at ICFRM-11, December 7-12, 2003, Kyoto, Japan, to be published in the *Journal of Nuclear Materials* (2004).
- [4] D. J. Senior, G. E. Youngblood, D. V. Archer, and C. E. Chamberlin, Recent Progress in Thermal Conductivity Testing of SiC-Based Materials for Fusion Reactor Applications, in the *Proceedings of the 3rd IEA Workshop on SiC/SiC Ceramic Composites for Fusion Structural Applications*, Cocoa Beach, Fla., January 29-30, 1999, p. 102.

- [5] G. E. Youngblood, D. J. Senior, and R. H. Jones, Thermal diffusivity/conductivity of irradiated Hi-Nicalon 2D-SiC/SiC composite, Fusion Materials Semiannual Progress Report for Period Ending June 30, 2003, DOE-ER-0313/34, p. 41.
- [6] Tyranno, SA ref.

FAST FRACTURE STRENGTH OF THIN PYROLYTIC CARBON INTERPHASE SILICON CARBIDE COMPOSITES—Y. Katoh, T. Nozawa, and L. L. Snead (Oak Ridge National Laboratory), T. Hinoki and A. Kohyama (Kyoto University, Japan), and W. Yang (National Institute for Materials Science, Japan)

OBJECTIVE

The objective of present work is to determine factors responsible for the reported deteriorative effects of thin pyrolytic carbon interphase on mechanical properties of chemically vapor-infiltrated silicon carbide matrix composites with conventional silicon carbide-based ceramic fibers and to evaluate the applicability of very thin pyrolytic carbon interphase to near-stoichiometric silicon carbide fiber composites for use in nuclear environments.

SUMMARY

The applicability of very thin pyrolytic carbon (PyC) interphase between fibers and matrices in silicon carbide (SiC) fiber-reinforced, chemically vapor-infiltrated SiC matrix composites was studied based on investigations on the effect of interphase thickness on fast fracture properties. It appears that the mechanical properties of near-stoichiometric high-crystallinity SiC fiber composites are not subject to strong interphase thickness effect, which has been reported for non-stoichiometric SiC fiber composites. This difference was discussed from the viewpoints of thermal residual stress, process-induced damages, fiber surface features, and interfacial bonding and friction. A preliminary conclusion is drawn that a thin PyC interphase, as low as ~25nm, will be generally beneficial for both fast fracture and lifetime limiting properties in stoichiometric SiC-based composites.

PROGRESS AND STATUS

Introduction

Continuous silicon carbide (SiC) fiber-reinforced SiC matrix composites (SiC/SiC composites) are considered as favorable options for structural materials in nuclear fusion and fission reactors, as well as in other advanced energy systems [1,2]. This is primarily due to the fact that the combination of inherent heat resistance, neutron tolerance, and low induced activation / low decay heat properties unique to SiC is of great benefit for core structure applications in nuclear systems. However, although stoichiometric crystalline SiC has demonstrated outstanding neutron tolerance [3], non-stoichiometric SiC-based ceramics, such as ceramic grade (CG-) Nicalon™ and Hi-Nicalon™ fibers, reaction-bonded or polymer-derived SiC-based matrices, and pyrolytic carbon (PyC) interphase are substantially susceptible to neutron-induced degradation [4-6]. Therefore, among presently available SiC/SiC composites, chemically vapor-infiltrated (CVI) near-stoichiometric SiC fiber-reinforced composites with minimal usage of PyC in their interphase appear to be the most appropriate for nuclear applications, and the thinner PyC interphase is likely to provide extended service life [7].

On the other hand, for SiC/SiC composites with PyC interphase between fiber and matrix, optimum flexural strength has reportedly been obtained for an intermediate interphase thickness [8]. It has also been reported that flexural strength decreases drastically when the interphase decreases in thickness with respect to this optimum value. Very limited neutron irradiation data show that, near-stoichiometry SiC

fiber-reinforced CVI-SiC composites with 150~200nm-thick PyC interphase do not undergo detectible degradation to a dose of $\sim 8 \times 10^{25}$ n/m² ($E > 0.1\text{MeV}$), while a sign of degradation was noted for similar composite with >500nm PyC interphase at the same dose [9]. This dose level corresponds to less than 10% of the desired lifetime in fusion power reactor applications [10]. Therefore, applicability of even thinner PyC interphase might be crucial for this material system. The present work is intended to determine the factors responsible for reported strength degradation in conventional thin-PyC interphase SiC/SiC composites and to evaluate the applicability of thinner PyC interphase to advanced SiC/SiC composites for nuclear applications.

Materials and Method of Evaluation

The materials evaluated were CVI-SiC matrix PyC interphase composites reinforced by two-dimensional (2D) plain-woven fabrics of various SiC-based fibers, namely, CG-Nicalon™, Hi-Nicalon™, Hi-Nicalon™ Type-S (Nippon Carbon Co., Tokyo, Japan) and 7.5-micron-diameter Tyranno™-SA Grade-3 (Ube Industries, Ltd., Ube, Japan). Details of the fibers are compiled elsewhere [11]. All the composites were matrix-densified by forced-flow CVI following PyC interphase deposition by isothermal CVD on fabrics stacked in 0°/90° or 0°/30°/60° sequences and tightly constrained in refractory fixtures [12,13]. The interphase thickness was tailored in a range of 0 to 760nm by varying deposition time. The interphase precursor was methane or propane and the optimum deposition temperature and pressure were selected for respective precursors, but the deposition rate of PyC was similar in a range of 30 to 100 nm/hr and the resultant microstructures were turbostratic carbon with very similar lattice images in all cases. The matrix precursor was methyltrichlorosilane (MTS) carried by hydrogen in all cases. Fiber volume fractions and the final porosity were 30 - 43% and 11 - 28%, respectively.

The mechanical property evaluation was performed at ambient temperature by either four-point flexure, three-point flexure, or tensile testing, following general guidelines of ASTM Standards D790, C1341 and C1275, respectively. Miniature specimens were used due to the limited availability of materials [14]. Fracture surfaces were examined for selected specimens by scanning electron microscopy (SEM). Fiber-matrix interfacial shear properties were evaluated by single fiber push-out / push-back method using a load / displacement-sensing nano-indentation device [15].

Results and Discussion

It was very clearly demonstrated that the ultimate tensile / flexural strength of the near-stoichiometry SiC fiber composites are much less sensitive to PyC interphase thickness than that of more conventional SiC-based fiber composites. As shown in Fig. 1, while CG-Nicalon™ and Hi-Nicalon™ composites exhibit their peak strength at an interphase thickness of 100 - 200nm, the strength of Tyranno™-SA and Hi-Nicalon™ Type-S composites is nearly independent of interphase thickness in the range of 25 - 250nm.

The ultimate strength of composites is determined by the strength and number of ‘working’ fibers and thus governed by the mean strength and Weibull modulus for strength of fibers and frictional stress at fiber-matrix interface in an ideal system [16]. Such a simple theory gives a reasonable explanation for the decrease in ultimate strength with increasing interphase thickness regardless of fiber type, as a result of decreasing frictional stress, beyond the strength peak. For near-stoichiometric SiC fiber composites, the Hi-Nicalon Type-S composites shows a slightly negative correlation between interphase thickness and UTS, while UTS of the Tyranno-SA composites is nearly constant over 25-250nm of interphase thickness. This difference could be attributed to the more pronounced dependence of interfacial frictional stress on interphase thickness in this range in the Hi-Nicalon Type-S composites arising from the significantly smoother fiber surface.

The situation on the thin side of the peak strength is more complex. For the case of CG-Nicalon composites, the interphase thickness effect has been discussed from viewpoints of interfacial bonding, friction, moderation of thermal residual stress [8], composites’ macroscopic fracture toughness, interlaminar shear strength [17], and the influence of elastic properties of interphase on crack propagation criteria [18]. These discussions apply to Hi-Nicalon composites, since both fibers have similar surface chemistry and morphology, coefficient of thermal expansion (CTE), and elastic moduli. The result of interfacial shear strength evaluation on Hi-Nicalon composites by single fiber push-out testing is presented in Fig. 2. In this test, the calculated stress reflects contributions from bonding and sliding stresses [13]. As shown by the results of Fig. 2, the interfacial bond readily fails in Hi-Nicalon composites when the interphase thickness is $< \sim 100\text{nm}$, except for the no-interphase case. Therefore, interfacial damage or substantial energy release due to CTE mismatch, which occurs either during

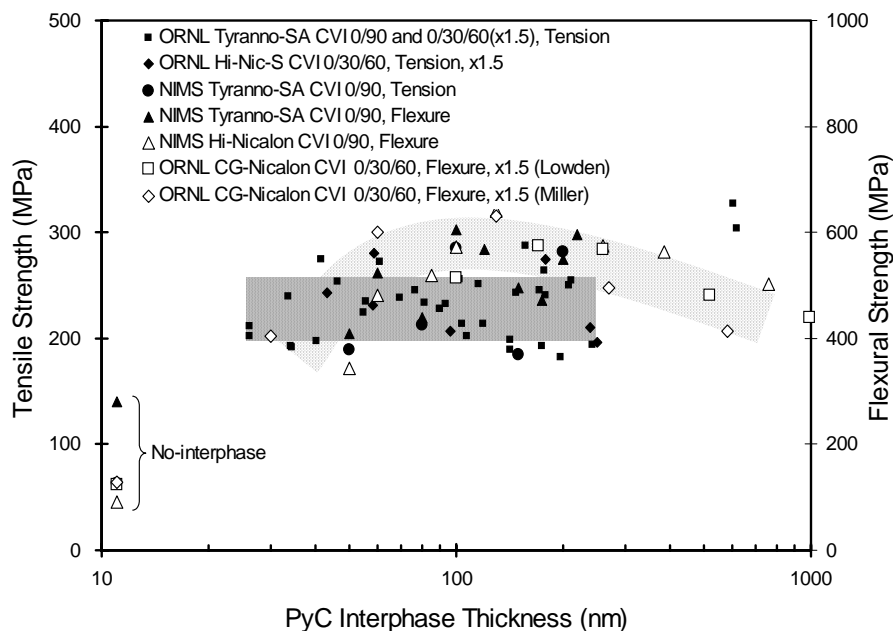


Fig. 1. The influence of PyC interphase thickness on ultimate tensile and flexural strength of CVI-SiC matrix composites reinforced with various SiC-based fibers. The strength of composites with a $0^\circ/30^\circ/60^\circ$ architecture is plotted after multiplying a factor of 1.5 in order to compensate the smaller fraction of longitudinal fibers than in $0^\circ/90^\circ$ composites.

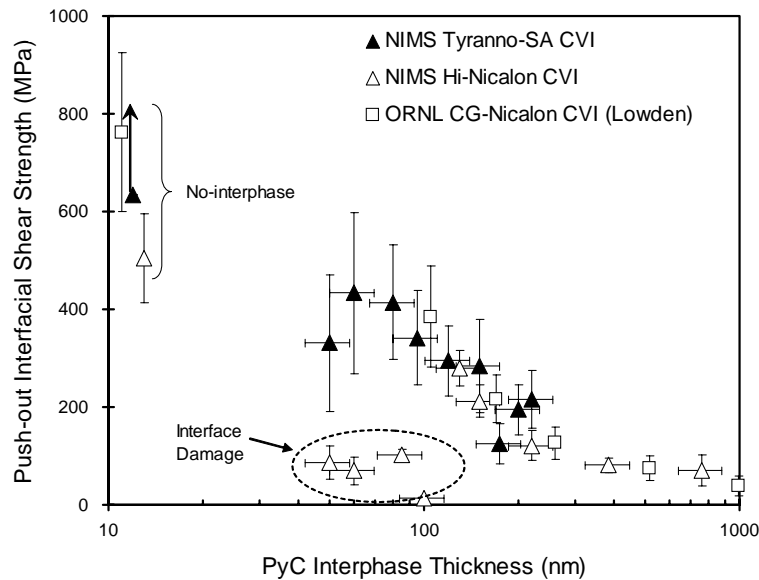


Fig. 2. The influence of PyC interphase thickness on interfacial shear strength as measured by single fiber push-out test. Vertical error bar corresponds to standard deviation. The minimum shear strength is shown for no-interphase Tyranno-SA composites since the interface did not debond in the test. Note the very small interfacial shear strength for Hi-Nicalon composites with PyC interphase thinner than ~100nm.

processing or during testing, is likely to be contributing to the observed interphase thickness effect. Another function of the PyC interphase is to protect the fibers against potential chemical attack by the matrix precursor. Excess carbon in non-stoichiometric SiC fiber reacts with the precursor gas to form SiC [19]. SEM examination of fiber fracture surfaces confirmed that uncoated Hi-Nicalon fibers clearly degrade during matrix processing, while a PyC coating of more than 50nm is sufficient to protect the fibers.

The greatly reduced sensitivity of fast fracture strength of near-stoichiometric SiC fiber composites to PyC interphase thickness may be primarily attributed to smaller CTE mismatch. This means that there exists less significant thermal residual stress in the matrix. Both types of the near-stoichiometric SiC fibers comprise primarily of cubic SiC and the C/SiC atomic ratios are 1.05~1.07. The excess carbon exists in a form of graphitic pockets at multi-grain junctions of cubic SiC grains of typically 20~200nm. A minor CTE mismatch between these fibers and cubic SiC matrix occurs due to the presence of graphitic phase, however, the extent of that is believed to be significantly smaller than for (Hi-) Nicalon composites. Detailed temperature dependent CTE data have not been published for near-stoichiometric SiC fibers. The proportional limit tensile stress (PLS) of Tyranno-SA composites exhibited slightly negative correlation with interphase thickness. Due to the radially graded concentration of excess carbon in Tyranno-SA, which results in better stoichiometry in near surface, the shear component of thermal residual stress at the fiber-matrix interface near matrix cracks should be even smaller than estimated from macroscopic CTE of the fiber.

In Fig. 3, fracture surfaces of Tyranno-SA composites are compared for uncoated and 120nm-thick PyC-coated fibers. Although practically no pullout is observed for the uncoated fibers reflecting strong

interfacial shear strength, the fiber fracture surface appears typical of undamaged fibers. Therefore, matrix processing presumably does not impose significant chemical damage to the near-stoichiometric SiC fibers.

Representative tensile stress-strain curves including intermediate unloading / reloading sequences are compared in Fig. 4 for Tyranno-SA composites with average interphase thickness of 25nm and 250nm, where little difference in fast fracture behavior is observed. This suggests that the interphase thickness effect, through energy release upon crack extension, was not active in this system, probably due to strong interfacial friction. The UTS difference noticed in Fig. 4 was not statistically significant. However, statistically significant interphase thickness dependence is found for tensile modulus and PLS, both of which negatively correlate with the interphase thickness [20]. The composites' elastic modulus moderation by the presence of interphase can reasonably be explained by relatively very small elastic

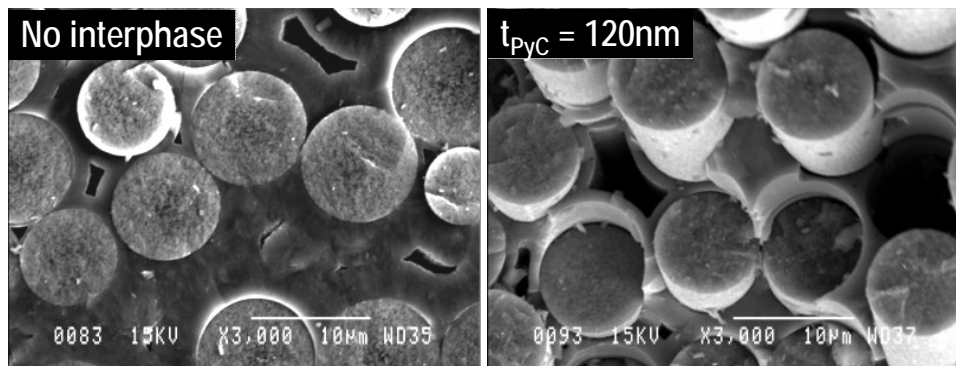


Fig. 3. SEM fracture surfaces of Tyranno™-SA composites without and with PyC interphase.

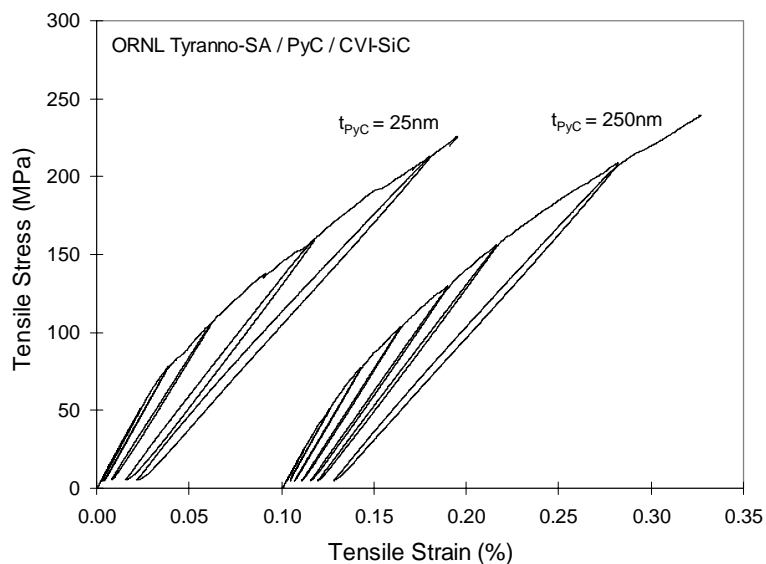


Fig. 4. Tensile behavior of Tyranno™-SA composites with PyC interphase thickness of 25nm and 250nm.

modulus of PyC. Proportional limit tensile strain was not affected by the interphase thickness, probably because the responsible matrix cracking initiates due to stress concentration at the surface of large inter-fiber-tow pores. Therefore, higher PLS in thinner interphase composite comes from the higher composite modulus.

Acknowledgement

The authors would like to thank Jerry McLaughlin and Tomitsugu Taguchi for contribution to material processing. Research partially supported by JUPITER-II US-DOE / Japanese Ministry of Education, Culture, Sports, Science and Technology (MEXT) collaboration for fusion material system research.

References

- [1] R. H. Jones et al., *J. Nucl. Mater.* 307-311 (2002) 1057-1072.
- [2] A. Kohyama and M. Singh, *Advances in Design and Fabrication of SiC/SiC Composites*, presented at 2003 ANS/ENS International Winter Meeting, November 16-20, 2003, New Orleans.
- [3] R. J. Price, *Nuclear Technology* 33 (1977) 320.
- [4] L. L. Snead, M. Osborne, and K. L. More, *J. Mater. Res.* 10 (1995) 736.
- [5] R. J. Price and G. R. Hopkins, *J. Nucl. Mater.* 108 and 109 (1982) 732-738.
- [6] Y. Katoh, A. Kohyama, and T. Hinoki, *Proc. 8th European Conference on Composite Materials Science -Technologies and Applications*, Vol. 4 (1998) 351-357.
- [7] Y. Katoh, A. Kohyama, T. Hinoki, and L. L. Snead, *Fusion Science and Technology* 44 [1] (2003) 155-162.
- [8] R.A. Lowden, in *Designing Ceramic Interfaces II*, Ed., S. D. Peters (1993) 155-171.
- [9] T. Hinoki, L. L. Snead, Y. Katoh, A. Hasegawa, T. Nozawa, and A. Kohyama, *J. Nucl. Mater.* 307-311 (2002) 1157-1162.
- [10] A. R. Raffray et al., *Fusion Engineering and Design* 55 (2001) 55-95.
- [11] K. Okamura, *Encyclopedia of Materials: Science and Technology*, ISBN 0-08-0431526, Elsevier Science Ltd. (2001) 1051-1056.
- [12] K. J. Probst, T. M. Besmann, D. P. Stinton, R. A. Lowden, T. J. Anderson, and T. L. Starr, *Surface and Coating Technology* 120-121 (1999) 250-258.
- [13] W. Yang et al., *Materials Transactions* 43 [10] (2002) 2568-2573.
- [14] T. Nozawa, T. Hinoki, Y. Katoh, A. Kohyama, and E. Lara-Cruzio, *Small Specimen Test Techniques*, Vol. 4, ASTM STP1418 (2002) 294-305.
- [15] T. Hinoki, W. Zhang, A. Kohyama, S. Sato, and T. Noda, *J. Nucl. Mater.* 258-263 (1998) 1567-1571.
- [16] A. G. Evans and D. B. Marshall, *Acta Metal.* 37 [10] (1989) 2567-2583.
- [17] J. H. Miller, P. K. Liaw, and J. D. Landes, *Materials Science and Engineering A317* (2001) 49-58.
- [18] S. Kumar and R. N. Singh, *Composites Science and Technology* 56 (1996) 1271-1281.
- [19] R. A. Lowden, *Characterization and Control of the Fiber-Matrix Interface in Ceramic Matrix Composites*, ORNL/TM-11039 (1989).
- [20] T. Nozawa et al., *Fusion Materials*, DOE/ER-0313/31 (2002) 40-46.

**3.0 FERRITIC/MARTENSITIC STEELS
AND
ODS STEELS**

OXIDE DISPERSION-STRENGTHENED STEELS: A COMPARISON OF EXPERIMENTAL AND COMMERCIAL STEELS—R. L. Klueh, J. P. Shingledecker, R. W. Swindeman, and D. T. Hoelzer (Oak Ridge National Laboratory)

OBJECTIVE

This work is carried out to develop an understanding of the mechanical properties and microstructures of experimental and commercial oxide dispersion-strengthened steels that are considered possible candidate materials for fusion applications.

SUMMARY

Oxide dispersion-strengthened (ODS) steels are being developed and investigated for nuclear fission and nuclear fusion applications in Japan, Europe, and the United States. In addition, commercial ODS products are available and have been used in niche applications. Microstructural and mechanical properties studies have been conducted at Oak Ridge National Laboratory and elsewhere on various commercial and experimental ODS steels. Tensile and creep properties have been obtained and collected from literature and commercial sources. These data are compared to show the differences and similarities of different ODS steels, and observations are explained in terms of the microstructures of the steels.

PROGRESS AND STATUS

Introduction

If the conventional high-chromium ferritic/martensitic steels, such as modified 9Cr-1Mo and Sandvik HT9, or the reduced-activation steels, such as F82H, ORNL 9Cr-2WVTa, EUROFER, and JLF-1, were used for a fusion power plant first wall and blanket structure, the upper operating temperature would be limited to 550-600°C.

One way suggested to increase this limit to higher temperatures and maintain the advantages inherent in ferritic/martensitic steels (i.e. high thermal conductivity and low swelling) is to use oxide dispersion-strengthened (ODS) steels. Elevated temperature strength in these steels is obtained through microstructures that contain a high density of small Y_2O_3 and/or TiO_2 particles dispersed in a ferrite matrix.

ODS steels are being developed and investigated for nuclear fission and fusion applications in Japan [1,2], Europe [3,4], and the United States [5]. Some commercial ODS products are available and are being used in limited quantities; commercial alloys include MA 956 and PM 2000 from Special Metals Corporation in the United States and Metallwerk Plansee GmbH in Germany, respectively. Microstructural and mechanical properties studies have been conducted at Oak Ridge National Laboratory (ORNL) on various commercial and experimental ODS steels. Results obtained at ORNL and elsewhere will be presented, compared, and discussed to show the differences and similarities of the different steels.

In previous work at ORNL, the microstructures and tensile and creep properties of two experimental ODS steels with nominal compositions of Fe-12Cr-0.25 Y_2O_3 (designated 12Y1), manufactured by Sumitomo Metal Industries Ltd., and Fe-12Cr-2.5W-0.4Ti-0.25 Y_2O_3 (designated 12YWT), manufactured by Kobe Special Tube Co. Ltd., were investigated [6]. Optical microscopy, transmission electron microscopy (TEM) [7], and atom probe field ion microscopy [8,9] studies indicated that the 12Y1 microstructures were very different from those of 12YWT (Fig. 1). For 12Y1 [Fig. 1(a)], particles were estimated to be 10-40 nm in diameter at a number density of 10^{20} - 10^{21} m^{-3} ; the dislocation density was estimated at $\approx 10^{15}$ m^{-2} . Diffraction studies indicated the particles were essentially pure, crystalline Y_2O_3 . For 12YWT [Fig. 1(b)], dislocation density, particle size, and particle number density were estimated at 10^{15} - 10^{16} m^{-2} , 3-5 nm diameter, and $1-2 \times 10^{23}$ m^{-3} , respectively. For this alloy, three-dimensional atom probe analysis revealed

compositionally distinct nano-sized clusters enriched in Y, Ti, and O, slightly enriched in Cr, and slightly depleted in Fe and W.

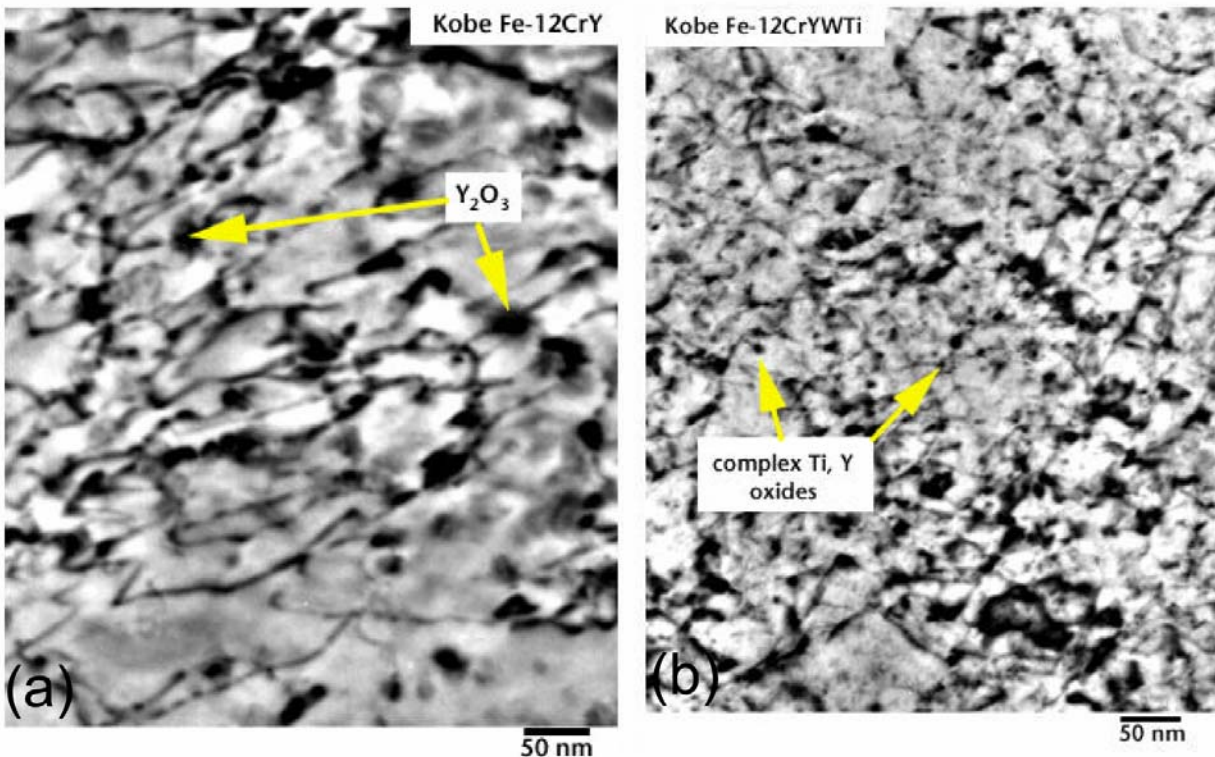


Fig. 1. Transmission electron micrographs of experimental ODS steels (a) 12Y1 (Fe-12Cr-0.25Y₂O₃) and (b) 12YWT (Fe-12Cr-2.5W-0.4Ti-0.25Y₂O₃).

These differences in microstructure were obviously the origin of large differences in tensile and creep properties [6]. Room-temperature yield stress of 12YWT was about 20% greater than 12Y1, but at 900°C, the 12YWT was about 2.5 times as strong. This large difference at the highest temperatures translated into a much higher creep strength for the 12YWT [6].

Mechanical properties of three other ODS steels have been determined: MA 956, MA957, and PM 2000. In this paper, tensile and creep properties of these commercial steels will be presented and compared with those of the experimental steels. The implications of the mechanical property results from the commercial steels will be discussed in terms of microstructural observations on the steels.

Experimental Procedure

Table 1 gives chemical compositions of the ODS steels to be discussed. Experimental alloys 12Y1 and 12YWT were produced in Japan by Sumitomo Industries and Kobe Special Tube, respectively. PM 2000 is a commercial product of Metallwerk Plansee GmbH of Germany. The MA 957 was manufactured by INCO Metals, and MA956 is a product of Special Metals Corporation.

Tensile and creep tests were conducted at ORNL on the 12Y1 and 12YWT [6]. Creep tests were conducted at ORNL on MA 957[10] and PM 2000 [11]. Creep and tensile data for the MA 956 [12] and MA 957 [13,14] and tensile data for PM 2000 [15] were taken from the literature or vendor data sheets. All tests are for specimens taken in the worked direction—the high-strength direction.

Different product forms for the different alloys were used in the creep and tensile tests at ORNL. Specimens of 12Y1 and 12YWT were from 2-mm sheet; the MA 957 specimens were from a tube 65-mm OD, 25-mm wall thickness, and the PM 2000 specimens were from 0.08- and 0.13-mm sheet.

Table 1. Chemical compositions of ODS steels

Element*	12Y1	12YWT	MA 956	MA 957	PM 2000
C	0.045	0.050	0.03	0.030	0.01
Mn	0.04	0.60	0.06	0.09	0.11
P	<0.001	0.019	0.008	0.007	<0.002
S	0.002	0.005	0.005	0.006	0.0021
Si	0.03	0.18	0.05	0.04	0.04
Ni	0.24	0.27	0.11	0.13	0.01
Cr	12.85	12.58	21.7	13.7	18.92
Mo	0.03	0.02	<0.05	0.30	0.01
V	0.007	0.002			
Ti	0.003	0.35	0.33	0.98	0.45
Co	0.005	0.02	0.03		0.01
Cu	0.01	0.02			0.01
Al	0.007		5.77	0.03	5.10
B	0.004			0.0009	<0.0003
W	<0.01	2.44			0.04
Zr	0.003				<0.01
N	0.017	0.014	0.029	0.044	0.0028
O	0.15	0.16	0.21	0.21	0.25
Y	0.20	0.16	0.38	0.28	0.37

*Balance iron

Results

Tensile behavior

The behavior of the yield stress and ultimate tensile strength of the experimental 12Y1 and 12YWT steels over the range room temperature to 900°C is shown in Fig. 2, along with data for a non-ODS reduced activation steel, ORNL 9Cr-2WVTa [16]. The obvious strength advantage of 12YWT is evident in the figure.

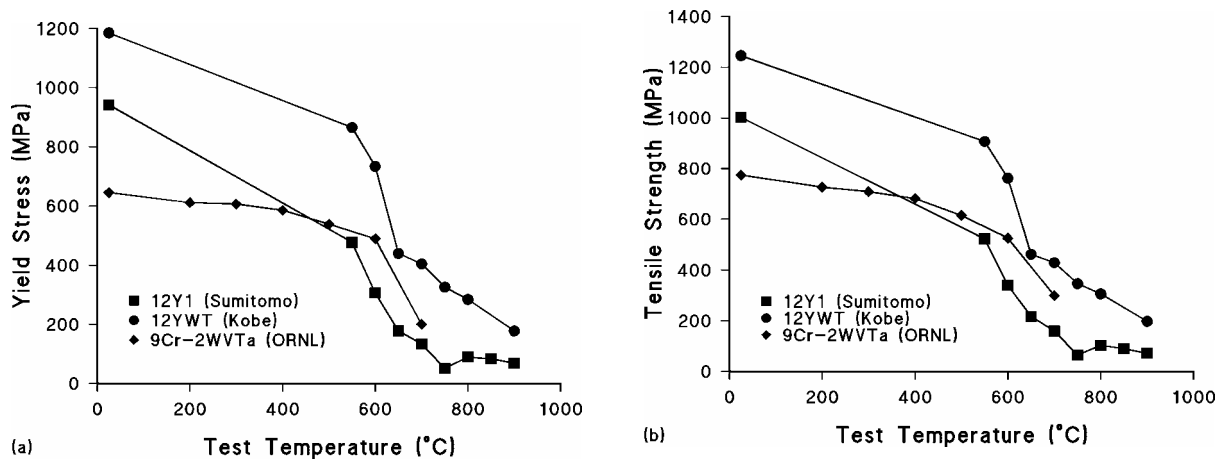


Fig. 2. (a) Yield stress and (b) ultimate tensile strength as a function of test temperature for the experimental ODS steels 12Y1 and 12YWT compared to the non-ODS reduced-activation steel ORNL 9Cr-2WVTa.

Of the commercial ODS steels, the MA 957 had the highest yield stress and ultimate tensile strength with the MA 956 having the lowest values (Fig. 3). In fact, up to 700°C, the yield stress of the MA956 was less

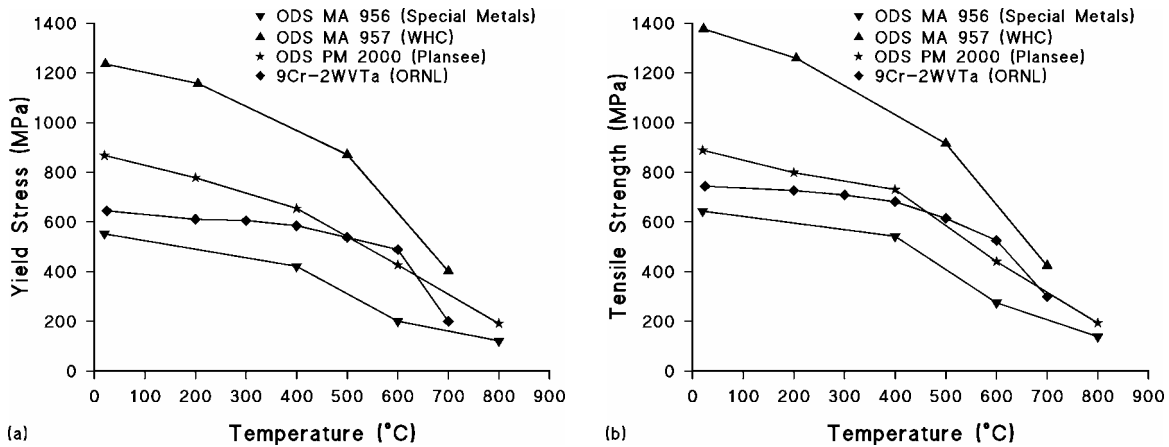


Fig. 3. A comparison of the (a) yield stress and (b) ultimate tensile strength as a function of test temperature for the three commercial ODS steels and the non-ODS reduced-activation steel ORNL 9Cr-2WVTa.

than that of 9Cr-2WVTa—a non-ODS martensitic steel. The strength of PM 2000 fell between the values for the MA 957 and MA 956.

When the commercial steels are compared with the experimental steels (Fig. 4), the MA957 and 12YWT, the strongest of the commercial and experimental steels, respectively, have similar strengths. The 12Y1 is similar to PM 2000 at low temperatures, but it then approaches the values for MA 956 at the higher temperatures. All steels appear to approach a common low strength value as the temperature is increased to 900°C.

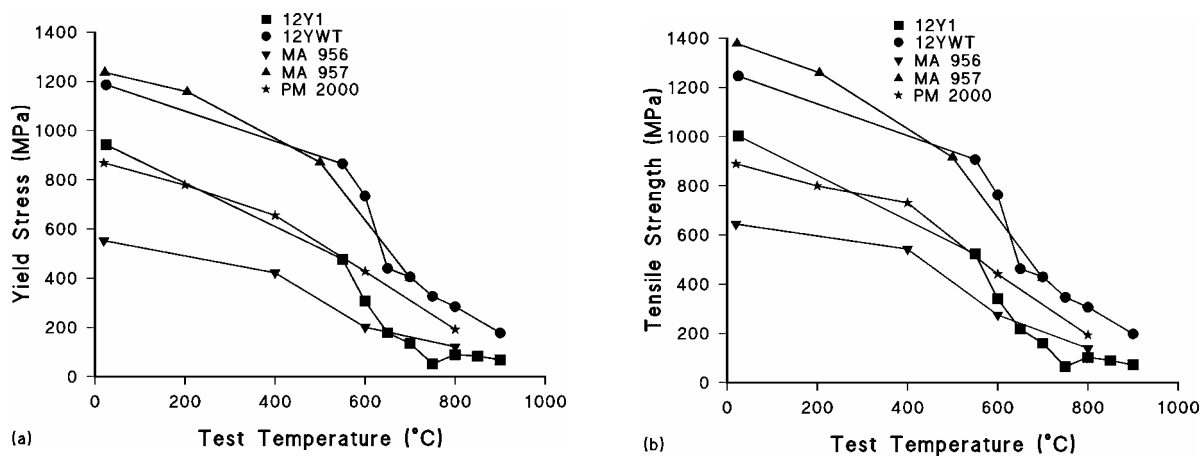


Fig. 4. A comparison of (a) yield stress and (b) ultimate tensile strength as a function of test temperature of the experimental and commercial ODS steels

Minor differences were observed in the total elongations of the experimental and commercial steels (Fig. 5). The 12Y1 and 12YWT had the lowest values at room temperature, and 12Y1 had the highest values.

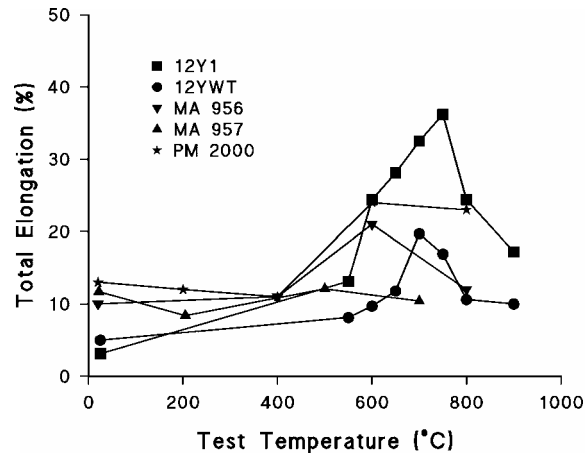


Fig. 5. A comparison of the total elongation as a function of test temperature of the experimental and commercial ODS steels between 600 to 800°C. Otherwise, the elongations of the commercial steels and the 12YWT were comparable.

Creep-rupture Behavior

Creep-rupture behavior was compared using a Larson-Miller Parameter (LMP) with a constant of 25, which was used for MA 956 and MA 957 previously [5]. A comparison of the experimental steels (Fig. 6) showed the superiority of the 12YWT to the 12Y1, in agreement with the yield stress behavior. Also shown on Fig. 6 are data for a conventional 9Cr-WMoVNb steel (a commercial steel designated NF616 or Grade 92). The creep behavior of the 12Y1 was similar to that of the conventional steel.

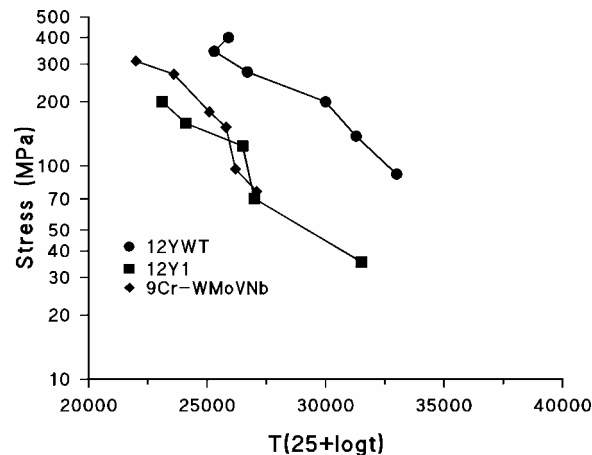


Fig. 6. Rupture stress vs. Larson-Miller parameter for the experimental ODS steels 12Y1 and 12YWT and a conventional non-ODS steel NF616 (9Cr-WMoVNb).

Comparison of the creep of the experimental ODS steels with the strongest (highest yield stress) commercial ODS steel MA 957, which was creep tested in this investigation, and MA 956, the weakest commercial ODS steel, indicates that the MA 956 and 12YWT have similar properties at high LMP (Fig. 7). Over the range where the LMP data for MA 957 and MA 956 overlap, it appears that they approach similar values, indicating an eventual convergence of the data for MA 957 and 12YWT, although that still needs to be demonstrated experimentally.

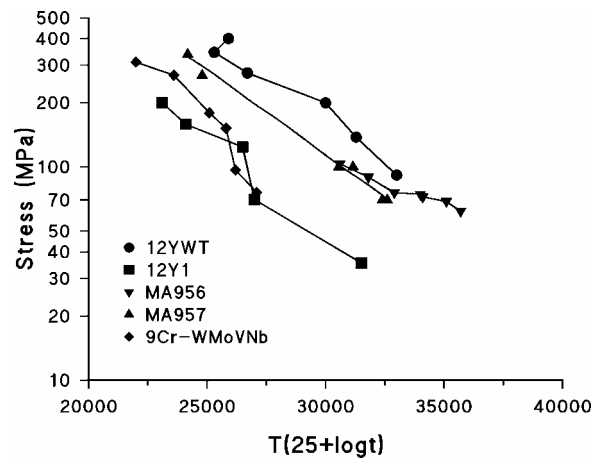


Fig. 7. Rupture stress vs. Larson-Miller parameter for the commercial steels MA 956 and MA957 compared to the experimental ODS steels and the non-ODS steel.

A comparison of the LMP values for PM 2000 with the experimental steels (Fig. 8) indicates that the creep-rupture strength of this steel is as good as that of 12YWT for the conditions tested. For the different sheet thicknesses, the thinner 0.08-mm sheet had better properties than the 0.13-mm sheet.

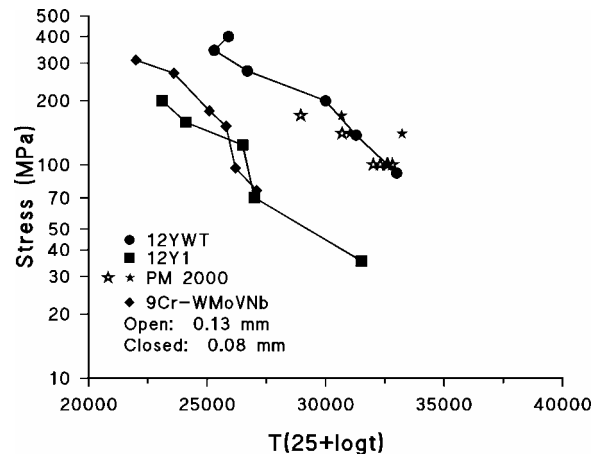


Fig. 8. Rupture stress vs. Larson-Miller parameter for the commercial steels PM 2000 compared to the experimental ODS steels and the non-ODS steel.

When the LMP for all the materials are compared (Fig. 9), it appears that all of the ODS steels except 12Y1 approach similar values for high LMP (low-stress and/or high temperature tests). This occurs despite the quite different yield stress values for the different steels.

Microstructures

Optical microscopy, TEM, and atom probe studies have been conducted on the 12Y1, 12YWT [7-9], and MA957 [17] with particular emphasis on the fine oxide particles that are responsible for the strength of the ODS alloys. In this study, microstructural features that are not part of the oxide dispersion and may therefore limit the strength and ductility have been conducted on the MA 957, and these will be discussed here.

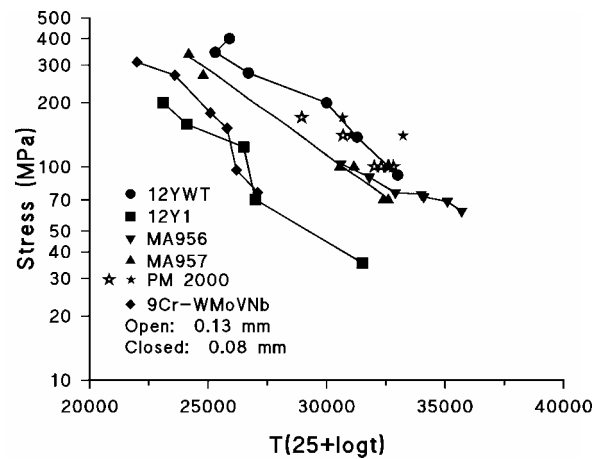


Fig. 9. Rupture stress vs. Larson-Miller parameter for all the commercial and experimental ODS steels and the non-ODS steel.

Optical microscopy of the MA 957 revealed large second-phase particles that often appeared as relatively large “stringers” (Fig. 10) aligned along the rolling direction. A failed creep-rupture specimen was examined, and the failure appeared to be associated with the stringer material (Fig. 11). That is, it appeared that cavities formed in conjunction with the particles of stringer material and other extraneous particles not in the stringers, and these cavities linked up perpendicular to the worked direction (parallel to the eventual fracture surface).

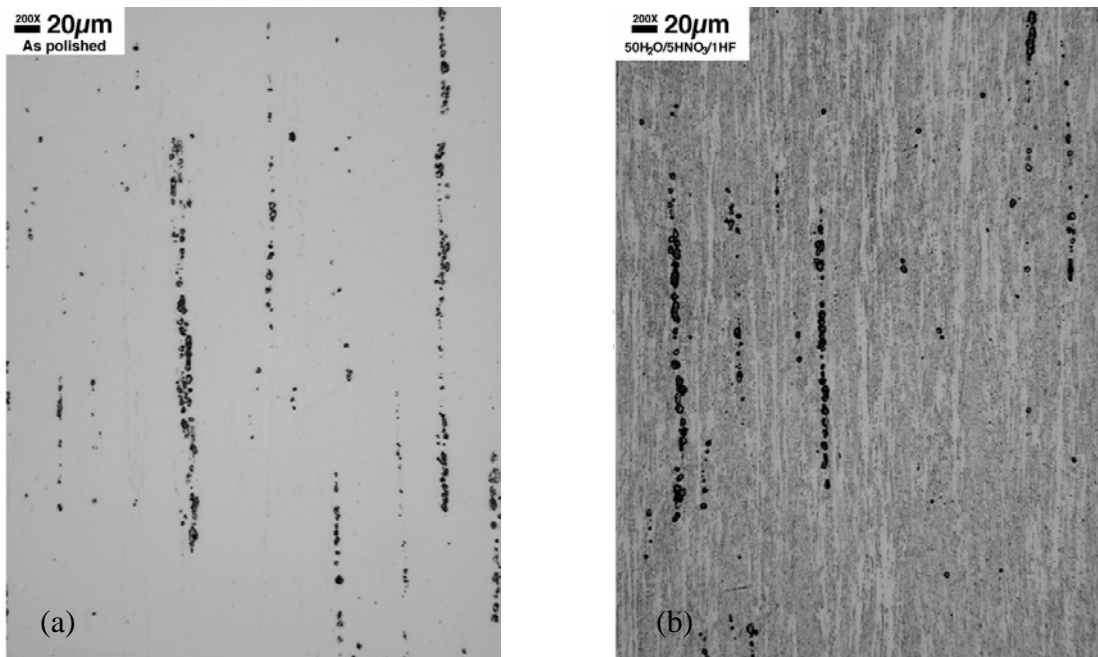


Fig. 10. Optical microstructure of MA 957 ODS steel (a) as polished and (b) etched.

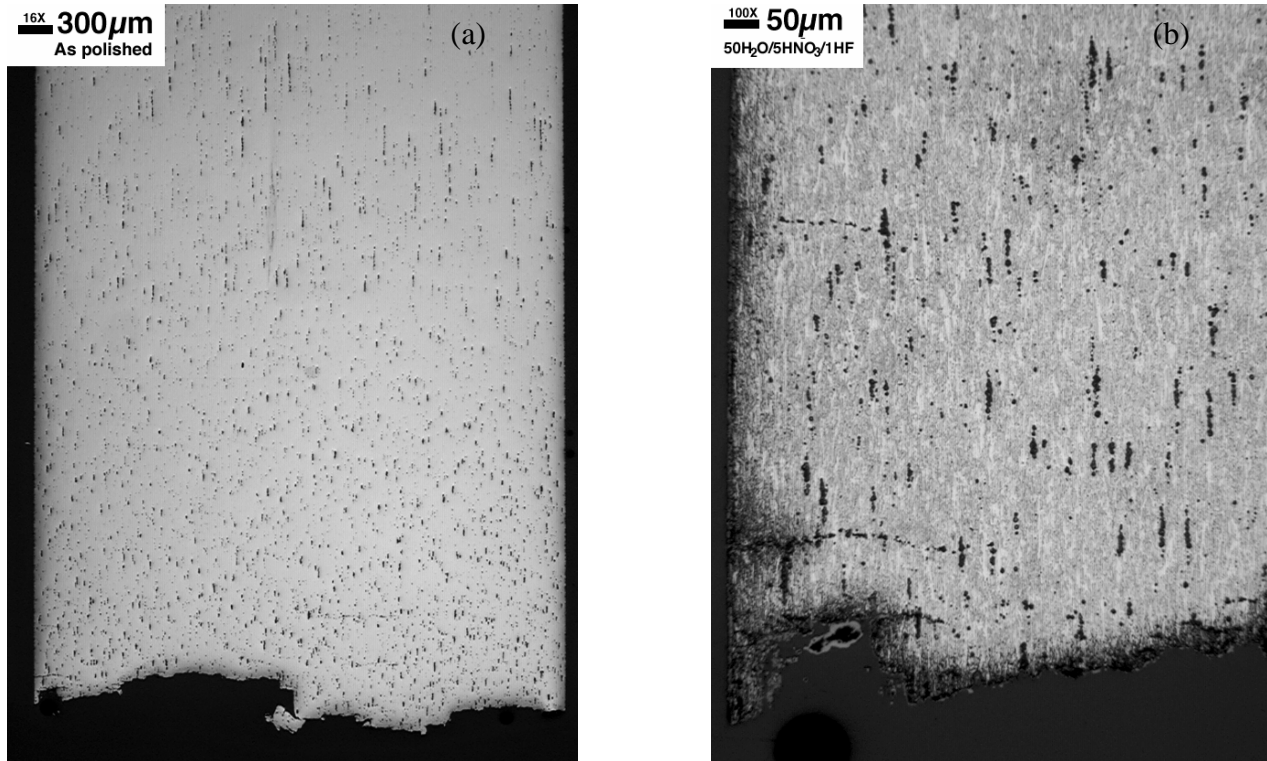


Fig. 11. Optical micrographs of fractured creep-rupture specimen of MA 957 tested at 100 MPa at 900°C that ruptured in 36.7 h at two different magnifications and (a) unetched and (b) etched.

To determine the nature of the particles in the stringers and other extraneous particles (not the fine distribution of oxide particles that strengthen ODS steels), the gage section of the creep-rupture specimen shown in Fig. 11 was examined by scanning electron microscopy (SEM) with a field emission gun (FEG) using backscattered and secondary electrons (Fig. 12). Such large particles are expected to be deleterious to the mechanical properties.

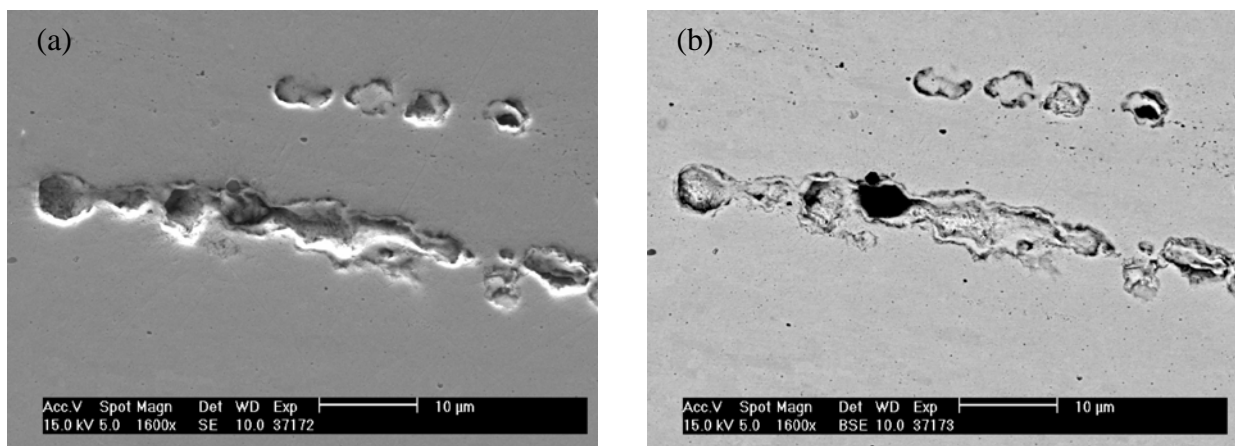


Fig. 12. (a) Secondary electron image and (b) backscattered electron image (compositional contrast) (right) of “stringers” in gage length of MA 957 creep specimen.

As expected, the primary elements identified in the matrix of the MA 957 were Fe, Cr, and Ti. The extraneous particles in and out of the stringers were rich in several different elements. Many particles in the stringers were carbon rich (Fig. 13); the presence of carbon is probably the result of mill contamination during the mechanical alloying process. Small precipitates throughout the microstructure were found to be aluminum rich (Fig. 13); aluminum is probably also from mill contamination, since the specification for MA 957 does not contain aluminum.

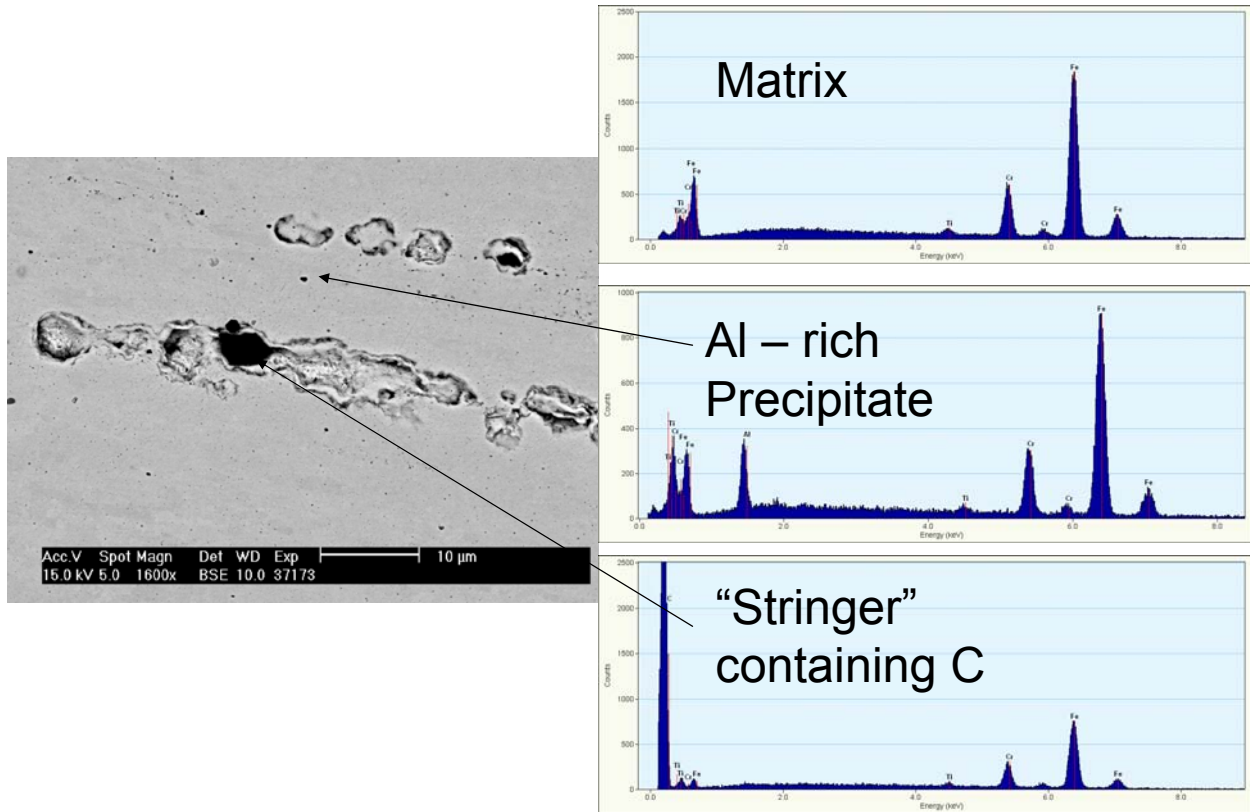


Fig. 13. Results of backscattered image analyses that show high-carbon and aluminum-rich particles present in the large particles present in the ODS steel MA 957.

Examination of a region near the creep failure indicated the presence of segregation that links up regions between stringers (Fig. 14) and probably leads to the relatively brittle creep failure shown in Fig. 11. The segregation, especially in the stringers, is rich in chromium, titanium, and carbon, which probably indicates the presence of carbide particles. These particles in the stringers were joined by “trails” of segregation that were found to be chromium rich. There were also indications of cavitation associated with areas of the segregation, indicating that it could be the joining of such cavitation that leads to the creep failure.

Discussion

Development of ODS steels for fast reactor cladding began in Belgium in the late 1960s [18], and work for that application has continued [19,20]. The main problem that kept the steels from being used for that application is anisotropy in properties that results from the fabrication process. Fabrication involves mixing the metal alloy powders with oxide (Y_2O_3) powders and mechanical alloying the powders, followed by compaction, and extrusion at elevated temperatures. The steels have superior creep strength in the longitudinal (extrusion) direction (properties most often studied), but, in the case of tubes, not in the biaxial direction. The problem with anisotropy still exists in more recent steels being developed [19,21],

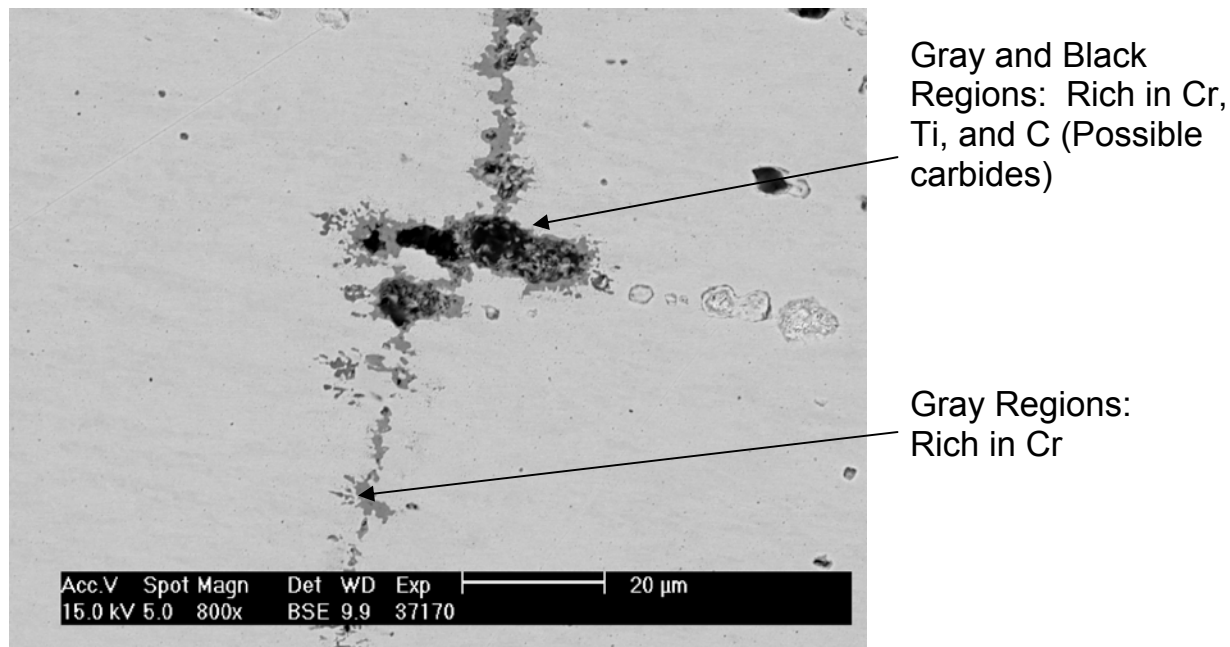


Fig. 14. Backscatter image showing that segregation occurs perpendicular to the worked direction in the region of the creep fracture.

although there have been advances in reducing it [22]. Anisotropy is present in the steels discussed in this paper, although that subject will not be discussed further. The objective of these studies was to compare strength properties in the strong (longitudinal) direction to determine similarities and differences among the different commercial and experimental steels that have been studied recently.

Initial TEM examination at ORNL of the experimental Fe-12.3Cr-3W-0.39Ti-0.25Y₂O₃ (12YWT) and an Fe-12.4Cr-0.25 Y₂O₃ (12Y1) ODS steels produced by Kobe Steel and Sumitomo Tubes, respectively, indicated that the 12YWT contained 3-5-nm diameter particles at a number density of $1-2 \times 10^{23} \text{ m}^{-3}$, whereas the 12Y1 contained 10-40 nm particles at a number density of $10^{20}-10^{21} \text{ m}^{-3}$ (Fig. 1) [7]. Electron diffraction indicated that particles in the 12Y1 were essentially pure Y₂O₃. Because of the size of the particles in 12CrYWT, the three-dimensional atom probe (3-DAP) was used to determine that the small particles were primarily atom clusters enriched in Y, Ti, and O [8,9]. From this [8,9] and previous work [23], it was concluded that the original Y₂O₃ particles dissolved during the mechanical alloying, and new clusters formed during subsequent processing (extrusion, etc.). This dissolution and subsequent reformation was obvious, since the atom probe indicated the concentration of titanium in the clusters was higher than the concentration of yttrium [8,9].

The difference in the microstructures of 12Y1 and 12YWT was reflected in the difference in tensile (Fig. 2) and creep (Fig. 6) strengths, with the 12YWT having much higher tensile and creep strengths than 12Y1. The yield stress of the 12YWT was also significantly higher than that of the commercial MA 956 and PM 2000, and it was comparable to that of MA 957 (Fig. 4).

The difference in creep properties of the commercial steels and 12YWT did not seem to follow from the relative strengths observed in the tensile tests. In particular, although 12YWT had the highest yield stress and ultimate tensile strength of the experimental steels and all the commercial steels but MA 957 (Fig. 4), creep-rupture properties based on the LMP comparison indicated that in the limit of low stresses and/or long rupture times, the commercial steels and the 12YWT approach a common strength level (Fig. 9).

The MA 956 had yield stress and ultimate tensile strength values from room temperature to 800°C that were much less than those for 12YWT. Nevertheless, the LMP values indicated that for long-time tests and/or high-temperature creep tests, the values for MA 956 approach those for 12YWT.

Similarly, the yield stress and ultimate tensile strength of PM 2000 were less than for 12YWT, but the long-time, low-stress creep properties of the PM 2000 0.08-and 0.13-mm sheet specimens were as good as those for the 12YWT based on LMP (Fig. 8). Note that the tensile properties in Fig. 4 for PM 2000 are from vendor data on bar product. Vendor data for ultimate tensile strength (no yield stress data were given) for 1-8-mm sheet showed the sheet to be weaker than the bar [15].

Finally, the MA957 and 12YWT had equivalent yield stresses and ultimate tensile strengths, but the a comparison of the LMP indicated that for the completed creep tests for MA 957, there was an advantage for 12YWT (Fig. 7). However, just as for the other commercial products, at high LMP, the values for MA 957 approached those for MA 956, which appear to converge with those for 12YWT.

These results indicate that, with the exception of 12Y1, the creep-rupture properties of the other four steels appear to approach a similar level with decreasing stress and/or increasing test temperature. As stated above, the excellent creep strength of the 12YWT was attributed to the fine distribution of particles (atom clusters) observed by atom probe studies in 12YWT and not 12Y1 [7-9].

Recent atom probe studies on the MA 957 indicated the presence of 2-nm-diameter particles similar to those in 12YWT [17]. Just as in 12YWT, the particles were rich in Ti, Y, and O. These results indicate that the same dissolution of the Y_2O_3 that occurred during mechanical alloying in Y12WT [8,23] must also occur during the mechanical alloying of MA 957. Since the creep properties of these steels depend on the distribution of oxide particles, the convergence of rupture properties at long times would be expected, given the similarity of the microstructures. Given the convergence of creep-rupture properties of MA 956, MA 957, PM 2000, and 12YWT at long rupture time and/or high temperatures (Fig. 9), one explanation is that the MA 956 and PM 2000 also contain the high density of small particles found in MA 957 and 12YWT.

Generally, relative creep strengths are comparable to the relative strengths observed in a tensile test. This raises a problem with the explanation that the similarity of creep behavior of the 12YWT and the commercial steels is caused by similar nano-sized particles, because it does not explain the difference in tensile properties of the different steels. That is, it would be expected that the high strength in the tensile tests of 12YWT and MA 957 would also depend on the presence of the small particles.

From TEM and atom-probe observations on the 12Y1 and 12YWT, it appeared that the major microstructural difference in the two was the absence of the small nano-sized clusters in 12Y1[7-9]. This difference could be used explain why 12Y1 has inferior tensile and creep properties compared to 12YWT. The observation of the nano-sized clusters in the MA 957 [17] also explains the similarity in tensile and creep properties of this steel and 12YWT. Therefore, if all the commercial steels contain the small nano-sized clusters postulated above and tensile and creep properties are determined by these particles, then all the commercial steels should have similar tensile properties, which is not the case.

Another possibility is that the lower tensile strength properties of the MA 956 and PM 2000 result from the absence of nano-sized particles in the latter two steels. This appears unlikely, given the observations on the much lower creep strength of the 12Y1, which did not contain the nano-sized particles. If it were true, however, the conclusion would be that the creep-rupture properties do not depend on the nano-sized particles, but on another dimension of particles. Obviously, TEM and atom probe studies of MA 956 and PM 2000 are required.

It appeared that the yield stress and ultimate tensile strength for all the steels converged at the highest test temperatures, although the 12Y1 had the lowest values at the highest temperatures (Fig. 4). Convergence for this steel appeared to be at a much higher temperature than for the other steels. Given this observation and the observation on the inhomogeneity of the microstructure of the MA 957 (Figs. 11-14), another explanation can be suggested. Such inhomogeneous regions may affect the strength

negatively at low tensile test temperatures, and it is the difference in the relative amounts of such regions in the different steels that plays a role in limiting the strength in a tensile test at temperatures up to 800-900°C, where the tensile properties begin to converge. Optical microscopy indicated that such inhomogeneous regions exist in all of the experimental and commercial steels tested. Another possibility is the effect of an inhomogeneous grain size, which is generally observed in the microstructures of these steels. Detailed SEM and optical quantitative microscopy along with TEM is required to determine if these explanations can be correlated with the mechanical properties observations.

Summary and Conclusions

Tensile and creep-rupture data for two experimental ODS steels and three commercial ODS steels were collected and compared. The experimental steels are: 12Y1 (nominally Fe-12Cr-0.25Y₂O₃) and 12YWT (Fe-12Cr-3W-0.4Ti-0.25Y₂O₃); the commercial steels are: MA 956 (Fe-20Cr-4.5Al-0.33Ti-0.5 Y₂O₃), MA 957 (Fe-14Cr-0.3Mo-1Ti-0.25Y₂O₃), and PM 2000 (Fe-19Cr-5.5Al-0.5Ti-0.5 Y₂O₃).

There was a significant variation in the yield stress and ultimate tensile strength of the different steels tested at room temperature to 800°C. The 12YWT was much stronger than the 12Y1. Of the commercial steels, the MA 957 was the strongest with strength properties similar to the 12YWT. The MA 956 was the weakest of the commercial steels, with strengths below that of the 12Y1 below 650°C, and somewhat stronger at higher temperatures. The PM 2000 had a strength between that of MA 956 and MA 957; up to ≈550°C, the strength of PM 2000 was comparable to that of 12Y1, but at higher temperatures, PM 2000 was substantially stronger. Strength properties appeared to merge for extrapolations above ≈900°C.

Creep-rupture properties were compared using Larson-Miller parameters. Although there were differences between the 12YWT and the three commercial steels, at high Larson-Miller parameter values (high-temperature, long rupture time tests) there appeared to be a convergence of properties. Values for these four steels were greater than those for 12Y1, which gave no indication of converging to the same value.

The reason for the similar tensile and creep behavior of the MA 957 and 12YWT was concluded to be the distribution of nano-sized particles rich in Y, Ti, and O that have been observed by TEM and atom probe studies on 12YWT and MA 957. In contrast, such studies found much larger Y₂O₃ particles in the weaker 12Y1, explaining why this steel had inferior tensile and creep properties. However, a quandary exists when it comes to explaining the apparent excellent long-term creep properties of MA 956 and PM 2000, despite these steels having significantly lower tensile properties than 12YWT and MA 957.

References

- [1] S. Ukai, T. Nishida, H. Okada, T. Okuda, M. Fujiwara, and K. Asabe, *J. Nucl. Sci. Tech.* 34 (1997) 256.
- [2] S. Ukai, T. Yoshitake, S. Mizuta, Y. Matsudaira, S. Hagi, and T. Kobayashi, *J. Nucl. Sci. Tech.* 36 (1999) 710.
- [3] A. Alamo, J. Decours, M. Pigoury, C. Foucher, in: *Structural Applications of Mechanical Alloying*, ASM International, Materials Park, Ohio, 1990.
- [4] A. Alamo, H. Regle, G. Pons, and L. L. Bechade, *Materials Science Forum* 88-90 (1992) 183.
- [5] D. K. Mukhopadhyay, F. H. Froes, and D. S. Gelles, *J. Nucl. Mater.* 258-263 (1998) 1209-1215.
- [6] R. L. Klueh, P. J. Maziasz, I. S. Kim, L. Heatherly, D. T. Hoelzer, N. Hashimoto, E. A. Kenik, and K. Miyahara, *J. Nucl. Mater.* 307-311 (2002) 773.
- [7] I-S. Kim, J. D. Hunn, N. Hashimoto, D. L. Larson, P. J. Maziasz, K. Miyahara, and E. H. Lee, *J. Nucl. Mater.* 280 (2000) 264.
- [8] D. J. Larson, P. J. Maziasz, I-S. Kim, and K. Miyahara, *Scripta Met.* 44 (2001) 359.
- [9] M. K. Miller, E. A. Kenik, K. F. Russell, L. Heatherly, D. T. Hoelzer, and P. J. Maziasz, *Mat. Sci. Eng. A* 353 (2003) 140.
- [10] R. L. Klueh and J. P. Shingledecker, unpublished research, 2003.
- [11] B. A. Pint, R. W. Swindeman, K. L. More, and P. F. Tortorelli, *Proc. Intl. Gas Turbine and Aeroengine Congress and Exhibition*, New Orleans, June 4-7, 2001, American Society of Mechanical Engineers, New York, 2001.
- [12] Engineering Data Sheet for Incoloy MA 956, Special Metals Corp., SMC-008, October 2003.

- [13] J. J. Fischer, US Patent 4,075,010,21, February 1978.
- [14] M. L. Hamilton, D. S. Gelles, R. J. Lobsinger, G. D. Johnson, W. F. Brown, M. M. Paxton, R. J. Puigh, C. R. Eiholzer, C. Martinez, and M. A. Blotter, Fabrication Technological Development of the Oxide Dispersion Strengthened Alloy MA 957 for Fast Reactor Applications, Pacific Northwest National Laboratory, PNNL-13168, February 2000.
- [15] Material Data Sheet ODS-Superalloy PM 2000, Metallwerk Plansee GmbH, February 1993.
- [16] R. L. Klueh, *Met. Trans. 20A* (1989) 463.
- [17] M. K. Miller, D. T. Hoelzer, E. A. Kenik, and K. F. Russell, *J. Nucl. Mater.*, to be published.
- [18] J.-J. Huet, H. Massaux, L. DeWilde, and J. Noels, *Revue de Métallurgie* 65 (1968) 12.
- [19] S. Ukai, T. Yoshitake, S. Mizuta, Y. Matsudaira, S. Hagi, and T. Kobayashi, *J. Nucl. Sci. Tech.* 36 (1999) 710.
- [20] M. L. Hamilton, D. S. Gelles, R. J. Lobsinger, G. D. Johnson, W. F. Brown, M. M. Paxton, R. J. Puigh, C. R. Eiholzer, C. Marinez, and M. A. Blotter, Oxide Dispersion Strengthened Alloy MA957 for Fast Reactor Applications, Pacific Northwest National Laboratory, PNNL-13168, February 2000.
- [21] M. J. Alinger, G. R. Odette, and G. E. Lucas, *J. Nucl. Mater.* 307-311 (2002) 484.
- [22] S. Ukai and M. Fujiwara, *J. Nucl. Mater.* 307-311 (2002) 749.
- [23] T. Okuda and M. Fujiwara, *J. Mater. Sci. Lett.* 14 (1995) 1600.

4.0 COPPER ALLOYS

No contributions.

5.0 REFRACTORY METALS AND ALLOYS

No contributions.

6.0 AUSTENITIC STAINLESS STEELS

No contributions.

**7.0 MHD INSULATORS, INSULATING CERAMICS, AND
OPTICAL MATERIALS**

STUDY OF THE LONG-TERM STABILITY OF MULTI-LAYER MHD COATINGS FOR FUSION REACTOR APPLICATIONS—B. A. Pint, P. F. Tortorelli, L. D. Chitwood, and H. M. Meyer (Oak Ridge National Laboratory, USA) and M. Fujiwara (Tohoku University, Japan)

OBJECTIVE

The objective of this task is to assess the long-term, high-temperature compatibility of high electrical resistance, multi-layer coatings with lithium at high temperatures. Electrically insulating coatings on the first wall of magnetic confinement reactors are essential to reduce the magnetohydrodynamic (MHD) force that would otherwise inhibit the flow of the lithium coolant. A recent assessment of the crack tolerance for these coatings determined that a multi-layer coating with metal and ceramic layers was needed to prevent Li from wetting coating cracks or defects. Therefore, basic compatibility of a vanadium coating layer is now being assessed by studying the compatibility of vanadium alloys in static lithium.

SUMMARY

Static lithium compatibility tests have been conducted on vanadium alloys at 800°C. Mass gains have been detected that are not consistent with prior static Li exposures of unalloyed vanadium and are difficult to interpret based on the impurity levels in the lithium specified by the manufacturer. A second test gave more reasonable results. Some of the mass gain could be attributed to N and C uptake from the Li but this should be countered by O loss from the alloy. Post exposure analysis of the specimens indicated a surface layer rich in O, C and Ca but no indication for the embrittlement observed.

PROGRESS AND STATUS

Introduction

A recent evaluation of the effects of cracks and defects on the performance of MHD coatings indicated that a very small fraction of through-thickness cracks could be tolerated with the assumption that Li will wet the cracks and thereby short the coating.[1,2] Even if cracks in the coating are not inherent from the fabrication process, tensile stresses are likely to cause periodic cracking in the brittle ceramic layer.[2] One strategy to address this issue is to use a two-layer or multilayer coating with a metallic layer adjacent to the Li to prevent wetting of cracks in the ceramic layer. Multilayer coatings have been suggested in several papers, e.g., Ref. 3. This strategy switches the focus of the compatibility work from the ceramic layer to the metallic layer. A likely candidate for the metallic layer is vanadium or a V-base alloy. The V-Li blanket system was originally proposed because of the reported good compatibility between vanadium and Li, e.g., Ref. 4. However, a review of the literature revealed that some studies showed relatively high dissolution rates of vanadium alloys with Li in loop tests.[1,5,6] while others found good compatibility.[7,8] This discrepancy suggests that more work needs to be done to understand the compatibility of vanadium alloys in Li before the multi-layer concept can be considered viable. This report presents results from three capsule experiments conducted at ORNL; the first two with specimens from Japan and the third with specimens from the US program.

Experimental Procedure

Vanadium alloy coupons (250 μ m x 5mm x 25mm or 1mm x 10mm x 15mm) with various Cr and Ti contents and miniature tensile specimens (SS-3) of V-4Cr-4Ti (Heat#832665 made at Wah Chang, Albany, OR) were tested after a 1050°C, 1h vacuum anneal. The experimental procedure for static lithium capsule exposures has been outlined elsewhere.[9,10] Molybdenum capsules were used and all of the capsule tests were exposed for 1000h at 800°C. However, 5g of Li (9.4cm³) was used in each test and the

specimen volume was different in each test. After exposure, the vanadium alloy specimens were cleaned by a variety of techniques: (1) submerging them in methanol for 24h to dissolve the residual Li, (2) submerging them in ice water for 1h, (3) vacuum distillation for 10h at 550°C followed by 12h at 600°C in a specially developed rig with a water cooled copper coil and a base pressure of 10^{-6} Pa. The exposed SS-3 specimens were characterized using Auger electron spectroscopy (AES).

Results and Discussion

Figure 1 shows the specific mass change results for three Mo capsule tests with vanadium alloy specimens exposed to Li for 1000h at 800°C. The first capsule contained seven vanadium alloy coupons with various Cr and Ti contents with a total volume of 1.00cm^3 and all of the specimens were cleaned in alcohol. The second capsule contained nine coupons of V-4Cr-4Ti (NIFS Heat #2) with a total volume of 0.31cm^3 which had the Li removed by different methods. In each test, the specimens gained an unexpectedly large amount of mass. Because the mass gain is associated with impurity (e.g., N and C) uptake from the Li, the higher mass gains for the V-4Cr-4Ti specimens may be due to the smaller specimen volume in that capsule. Figure 1a shows the results for the first two capsules for specimens cleaned with alcohol and compares the mass changes for different Ti and Cr levels. Specimens with higher Cr levels showed the lowest mass gains. However, all of the mass gains were relatively similar. Figure 1b shows the mass gains for the V-4Cr-4Ti specimens with different cleaning methods. The mass gain after distillation was the highest. This could be due to some O uptake during the 600°C vacuum distillation exposure. From the second capsule test, the lowest mass gains were for cleaning in water. In prior work, lithium removal in water has been associated with the dissolution of Li_9CrN_5 . [11] For all of the cleaning methods, a thin surface film was observed on the specimens after exposure. Most of the specimens from these tests were sent to Japan for further characterization.

Because of the unexpected results, a third Mo capsule test was performed for the same time and temperature but using three SS-3 specimens of V-4Cr-4Ti with a total volume of only 0.18cm^3 . After this exposure, the specimens were cleaned in alcohol and appeared shiny (as expected). However, Fig. 1b shows that the specimens still experienced a significant mass gain. However, the mass gain was much

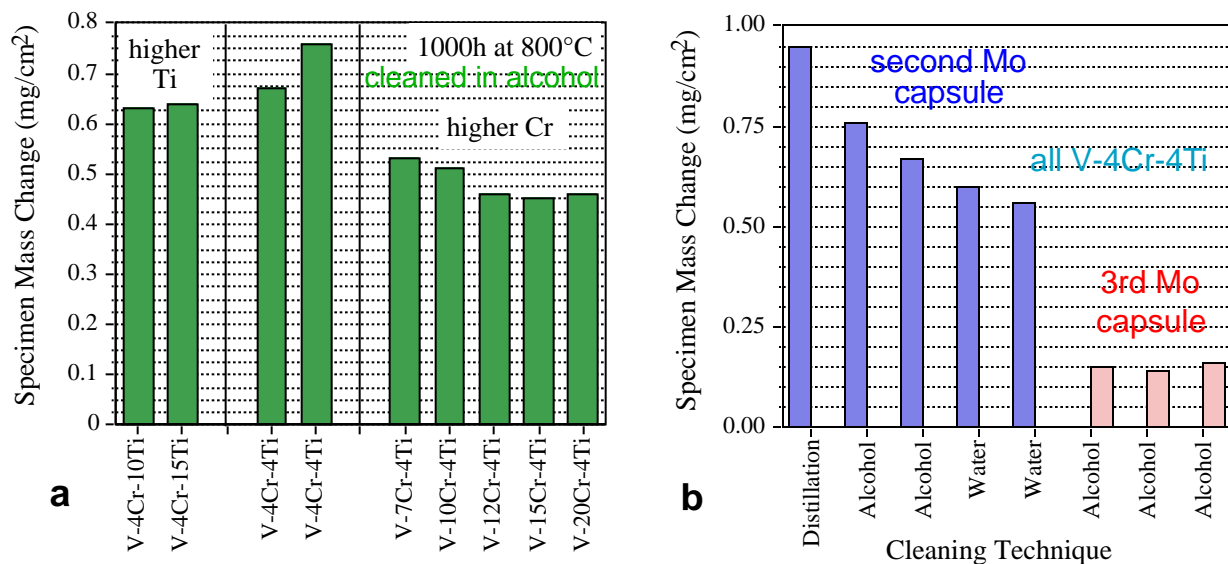


Fig. 1. (a) mass gain for various V-Cr-Ti alloy specimens after 1000h at 800°C in Li-filled Mo capsule and cleaned with chilled alcohol and (b) mass gain for V-4Cr-4Ti specimens after 1000h at 800°C in Li-filled Mo capsules and cleaned by various techniques.

lower compared to the previous tests. While drying one of the specimens in a lint-free cloth, it broke suggesting that all of the specimens were highly embrittled.

In all cases, the relatively high mass gains for so many samples cannot be explained. Vanadium alloys would be expected to getter N and C from the Li at this temperature. Each capsule contained 5g of Li with a manufacturers' analysis of 65ppmw N. No information is currently available on the C content. For the three specimens in the third capsule test, the N uptake could be as high as 0.06mg/cm^2 . However, a mass loss of 0.10mg/cm^2 would be expected if the Li gettered 300ppmw O from each specimen (which has a starting O content of 310ppmw[12]). The starting Li oxygen content has not been determined but this element would be expected to remain in the Li based on thermodynamic stability. In order to explain the mass gain for these specimens, a large fraction of the N and C must have absorbed by the V-4Cr-4Ti while little O was lost. The Li chemical composition from the third capsule after exposure is currently being measured in order to determine if there was any significant change in the chemistry.

It also is possible that some Li was absorbed into the specimen or Li-containing compounds formed. After exposure and cleaning, the V-4Cr-4Ti specimen which broke during cleaning was characterized by AES. (As with most analytical techniques for vanadium alloys, there is great difficulty resolving the overlap between the V and O and Ti and N signals. However, AES is able to detect Li.) Figure 2 shows examples of the specimen surface. No surface preparation was performed prior to the test so the as-rolled surface morphology is present. The morphology in Fig. 2a was similar to that of a specimen from the same batch exposed to He indicating that no significant reaction occurred on the surface. However, at higher magnification, the surface appeared terraced, suggesting that some mass transfer or surface rearrangement occurred. No significant amount of Mo was detected by AES analysis, thus ruling out mass transfer from the capsule. Also, no Li was detected on the specimen surface. However, a non-uniform distribution of Ca was found on the surface in the form of a Ca-V-O layer, approximately 5-10nm thick. Apparently a modification of the native oxide on the specimen, which was 10-15nm thick, must have occurred. The Ca was likely due to the 53ppmw Ca impurity in the Li but this layer could not account for even 5% of the mass increase for this specimen. (If all of the Ca in the Li reacted to form an oxide on the surfaces of the three specimens, a mass gain of 0.046mg/cm^2 would be expected.) Isolated particles also were observed on the surface, e.g., Fig. 2b. These particles were often rich in V, Ti, C and N but also occasionally contained small amounts of Ca, O, Cu and Mo. The small number of these particles also could not account for much of the mass increase.

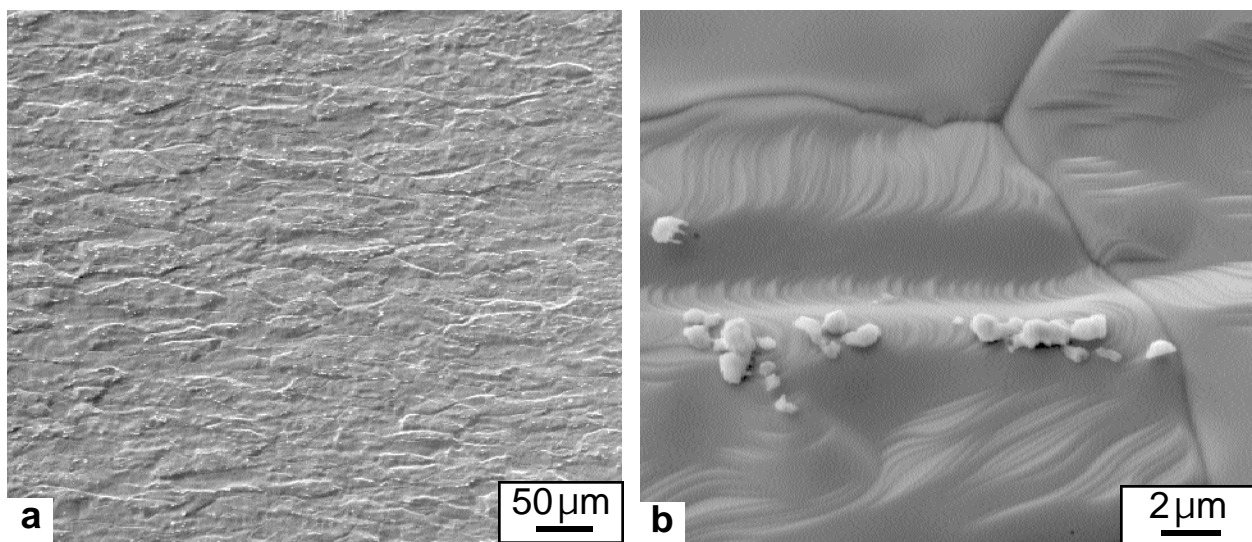


Fig. 2. SEM secondary electron images of the rolled V-4Cr-4Ti surface after exposure to Li for 1000h at 800°C. At higher magnification, (b), slight faceting or terracing of the surface was observed.

The fracture surface also was examined to determine the fracture mode. For this specimen, it appeared to be generally transgranular fracture, which indicates that the grain boundaries were not selectively embrittled, Fig. 3. This observation suggests that the matrix was embrittled by the exposure consistent with the mass gain.

To put the current results in perspective, Table I summarizes the results from a 1964 ORNL report by DiStefano of unalloyed vanadium tested in static Li capsule tests for 100h at 815°C.[13] Various levels of oxygen were added to vanadium using exposures at 850°C at an oxygen pressure of 10^{-2} Pa (9×10^{-5} Torr). Additions of O to Nb were known to increase its susceptibility to Li attack. However, for unalloyed vanadium, the O was selectively removed from the specimens resulting in a mass loss after exposure proportional to the O removed. No dissolution or attack of the vanadium specimens was observed. In this case, the specimens were cleaned by vacuum distillation.

Additional characterization is needed to further understand these results including measuring the impurity contents (N, O, C, H) of the specimens after exposure and obtaining more information on the Li chemistry. In general, future work will need to determine the role of Cr and Ti alloy additions on the compatibility of vanadium alloys with Li. However, capsule experiments can only be expected to produce a limited picture of V-Li compatibility. A loop experiment with a temperature gradient is needed to truly determine the compatibility in this system.

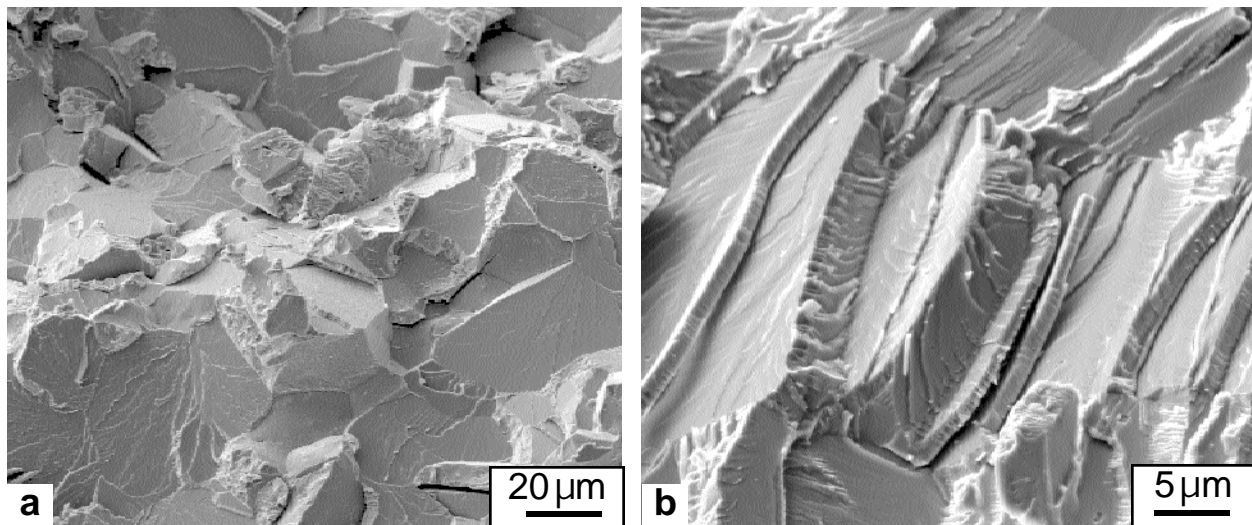


Fig. 3. SEM secondary electron images of the fracture surface of V-4Cr-4Ti which broke on handling after 1000h at 800°C.

Table 1. Summary of previous results of unalloyed vanadium exposed to Li for 100h at 815°C.[13]

Oxygen Content (ppmw)		<u>Mass loss</u>
<u>Before test</u>	<u>After Li exposure</u>	
400	80	0.08 (mg/cm ²)
800	110	0.20
1200	30	0.25
2200	180	0.52

REFERENCES

- [1] D.-K. Sze, private communication, 2003.
- [2] B. A. Pint, P. F. Tortorelli, A. Jankowski, J. Hays, T. Muroga, A. Suzuki, O. I. Yeliseyeva, and V. M. Chernov, *J. Nucl. Mater.* 329-333 (2004) 119.
- [3] Y. Y. Liu and D. L. Smith, *J. Nucl. Mat.* 141-43 (1986) 38.
- [4] S. J. Zinkle and N. M. Ghoniem, *Fusion Eng. Design* 51-52 (2000) 55.
- [5] Ch. Adelhelm, H. U. Borgstedt, and J. Konys, *Fusion Tech.* 8 (1985) 541.
- [6] O. K. Chopra and D. L. Smith, *J. Nucl. Mater.* 155-157 (1988) 683.
- [7] V. A. Evtikhin, I. E. Lyublinski, and A. V. Vertkov, *J. Nucl. Mater.* 258-263 (1998) 1487.
- [8] S. N. Votinov et al., *J. Nucl. Mater.* 233-237 (1996) 370.
- [9] B. A. Pint, J. H. DeVan, and J. R. DiStefano, *J. Nucl. Mater.* 307-311 (2002) 1344.
- [10] B. A. Pint, L. D. Chitwood, and J. R. DiStefano, *J. Nucl. Mater.* 289 (2001) 52.
- [11] O. K. Chopra and D. L. Smith, *J. Nucl. Mater.* 141-143 (1986) 584.
- [12] D. L. Smith, H. M. Chang, B. A. Loomis, and H.-C. Tsai, *J. Nucl. Mater.* 233-237 (1996) 356.
- [13] J. R. DiStefano, ORNL report No. 3551, Oak Ridge, Tenn. (1964).

EVALUATION OF THE CHEMICAL COMPATIBILITY OF Y_2O_3 AS AN ELECTRICALLY INSULATING COATING FOR A LIQUID LITHIUM BLANKET—P. F. Tortorelli, B. A. Pint, and T. M. Besmann (Oak Ridge National Laboratory, USA)

OBJECTIVE

The objective of this task is to assess the long-term, high-temperature compatibility of high electrical resistance coatings with lithium at high temperatures. Electrically insulating coatings on the first wall of magnetic confinement reactors are essential to reduce the magnetohydrodynamic (MHD) force that would otherwise inhibit the flow of the lithium coolant. Thermodynamic modeling is an integral part of this assessment program.

SUMMARY

Modeling of the chemical stability of Y_2O_3 in molten lithium was hampered by the lack of available thermochemical data for mixed oxides of Li-Y and Ti-Y. Nevertheless, this evaluation indicated that Y_2O_3 was not stable in a lithium environment at 600-1000°C. Furthermore, the results indicated that the experimental observations of Y-Ti oxides on Y_2O_3 after exposure to molten lithium in V-4Ti-4Cr capsules was likely due to formation of Li_2TiO_3 and $LiYO_2$.

PROGRESS AND STATUS

Background

Previous work related to the development of electrically insulating coatings to minimize the MHD resistance to lithium flow has shown significant instability issues related to several candidate ceramics (see, for example, [1]). A fundamental problem is that many oxides with sufficient electrical resistivity are reduced by molten lithium.[2,3] Furthermore, ceramics that appear to be stable based on their free energies of formation (ΔG 's) with respect to the ΔG of Li_2O (such as CaO) can still decompose due to dissolution of the metallic species when the cation solubility in lithium is appreciable.[4] Therefore, recent efforts have emphasized Y_2O_3 and Er_2O_3 as potential MHD coatings.[1] In this regard, initial fusion-related exposures of bulk Y_2O_3 in static lithium yielded somewhat promising results[4,5] consistent with some early work on lithium compatibility.[6] However, experiments with Y_2O_3 coatings have shown degradation of the ceramic.[1,7] While some of the incompatibilities can possibly be ascribed to coating defects and/or poor adhesion, chemical interactions of the Y_2O_3 and lithium were noted based on the presence of $LiYO_2$. [1,5,7] This product is electrically conductive and thus compromises the insulating ability of the coating.[1] Furthermore, some evidence of oxide particles containing yttrium and titanium were reported using Auger electron spectroscopy when Y_2O_3 coatings were exposed in V-4Ti-4Cr capsules.[1] Using glancing angle x-ray diffraction, a number of unidentified d peaks were observed but none could be matched to the limited data available from the Y-Ti-O system. In view of these observations, the fundamental chemical stabilities of Y_2O_3 and mixed yttrium-titanium oxides in molten lithium was investigated using equilibrium thermodynamic approaches based on the FACTSage™ databases and codes.[8]

Modeling Results

Based on simple free energy of formation considerations, Y_2O_3 is expected to be stable in molten lithium because the free energy of formation (ΔG) for yttria is significantly more negative than that of Li_2O over the temperature range of interest (see Table 1). In addition, the solubility of yttrium in lithium is expected to be low[9] so, unlike CaO in lithium,[4] cation dissolution should not significantly compromise

Table 1. Calculated free energies of formation per atom of oxygen

Temperature (°C)	ΔG (kJ/atom of O ₂)		
	Li ₂ O	Y ₂ O ₃	Li ₂ TiO ₃
600	-484	-550	-466
700	-470	-541	-456
800	-456	-531	-446
900	-443	-522	-435
1000	-429	-513	-425

compatibility. There are no thermodynamic data available for LiYO₂ in the FACTSage™ databases and, consequently, calculation of stable species in the Li-Y-O system does not predict this product. However, given the experimental observations of such,[1,5,7], LiYO₂ must be considered a stable product in the subject system.

The observation of Y-Ti-O products after exposure to static lithium[1] suggests the interesting possibility that such mixed oxides may be stable in molten lithium environments. (The titanium must be supplied from the V-Cr-Ti capsule wall or the V-4Cr-4Ti substrates, which were coated on one side only.) Thermodynamic data for Y₂TiO₅ and Y₂Ti₂O₇ were not found in any of the available databases. Therefore, to obtain initial thermodynamic values for these compounds, the 298K heats of formation and entropy, and heat capacities for Y₂O₃ and TiO₂ (rutile) were simply added in the appropriate proportions. Then, in order to get the phases to be sufficiently stable to form over the lower end of the temperature range, the binary oxides needed to be somewhat more stable. This was done by making the 298K heats of formation for Y₂TiO₅ and Y₂Ti₂O₇ more negative by a minimum of 2 and 3 kJ/mol, respectively.

Using the estimated ΔG 's for Y₂TiO₅ and Y₂Ti₂O₇, along with existing data for other phases and species in the Li-Y-Ti-O system, the equilibrium composition was calculated assuming one mole each of Y₂O₃, TiO₂, and Li at 800, 900, and 1000°C. In all cases the Li reacted to form complex oxides and reduced TiO₂. The Y₂TiO₅ and Y₂Ti₂O₇ phases did not form under these conditions. Interestingly, Li₂TiO₃ was one of the stable products. Its free energy is on the same order as that for Li₂O (see Table I).

To explore the degree of stability needed for Y₂TiO₅ to be present and for Li to remain metallic, the 298K heat of formation for this oxide was systematically made more negative until an equilibrium phase assemblage containing Li only as the metal was obtained. This required that the 298K heat of formation for Y₂TiO₅ be approximately 160 kJ/mol more negative. This is not a reasonable value, and is therefore unlikely. For comparison, the 298K heat for formation reported for the phase Y₂Zr₂O₅ is approximately 22kJ/mol more negative than that calculated by summing the values for Y₂O₃ and ZrO₂ (1:2). This confirms that the Y₂TiO₅ and Y₂Ti₂O₇ phases are unlikely to be stable with respect to Li under the conditions of interest.

Based on the thermochemical modeling described above, it appears the experimental finding of Y-Ti oxides on the yttria coating after exposure in molten lithium[1] cannot be explained on the basis of a stable Y₂TiO₅ or Y₂Ti₂O₇. However, it is quite possible that a mixture of LiYO₂ and Li₂TiO₃ formed and that this is what was observed. The extent of degradation of the Y₂O₃ by formation of these products depends on the respective rate constants, the morphologies of their reaction fronts, and the extent to which the electrical conductivity of the coating is raised by formation of these mixed oxides.

REFERENCES

- [1] B. A. Pint, P. F. Tortorelli, A. Jankowski, J. Hays, T. Muroga, A. Suzuki, O. I. Yeliseyeva, and V. M. Chernov, *J. Nucl. Mater.* 329-333 (2004) 119.
- [2] J. E. Battles, *Intern. Mater. Rev.* 34 (1989) 1.
- [3] R. J. Lauf and J. H. DeVan, *J. Electrochem. Soc.* 139 (1992) 2087.
- [4] B. A. Pint, J. H. DeVan, and J. R. DiStefano, *J. Nucl. Mater.* 307-311 (2002) 1344.
- [5] T. Terai, T. Yoneoka, H. Tanaka, A. Suzuki, S. Tanaka, M. Nakamichi, H. Kawamura, K. Miyajima, and Y. Harada, *J. Nucl. Mater.* 233-237 (1996) 421.
- [6] D. W. Jeppson, J. L. Ballif, W. W. Yuan, and B. E. Chou, Hanford Engineering Development Laboratory report, HEDL-TME 78-15, April 1978.
- [7] T. Mitsuyama, T. Terai, T. Yoneoka, and S. Tanaka, *Fus. Eng. Design* 39-40 (1998) 811.
- [8] C. W. Bale, P. Chartrand, S. A. Degterov, G. Eriksson, K. Hack, R. B. Mahfoud, J. Melancon, A. D. Pelton, and S. Petersen, *Calphad* 26 (2002) 189.
- [9] K. Natesan, C. B. Reed, M. Uz, J. H. Park, and D. L. Smith, ANL/TD/TM00-10 (2000).

HIGH DOSE NEUTRON IRRADIATION OF $MgAl_2O_4$ SPINEL: EFFECTS OF POST-IRRADIATION THERMAL ANNEALING ON EPR AND OPTICAL ABSORPTION—A. Ibarra (CIEMAT. Inst. Investigación Básica), D. Bravo (Universidad Autónoma de Madrid), F. J. Lopez (Universidad Autónoma de Madrid), and F. A. Garner (Pacific Northwest National Laboratory)*

OBJECTIVE

The object of this effort is to explore the origins of radiation-induced changes in physical properties of ceramic materials proposed for use in fusion reactors.

SUMMARY

Electron paramagnetic resonance (EPR) and optical absorption spectra were measured during thermal annealing for stoichiometric $MgAl_2O_4$ spinel that was previously irradiated in FFTF-MOTA at $\sim 405^\circ C$ to ~ 50 dpa. Both F and F+ centers are to persist up to very high temperatures (over $700^\circ C$), suggesting the operation of an annealing mechanism based on evaporation from extended defects. Using X-ray irradiation following the different annealing steps it was shown that the optical absorption band is related to a sharp EPR band at $g=2.0005$ and that the defect causing these effects is the F+ center.

PROGRESS AND STATUS

Introduction

$MgAl_2O_4$ is a ceramic spinel material with rather high radiation resistance, at least from the point of view of maintaining its original mechanical and elastic properties [1-4]. That resistance makes this material suitable for applications in high radiation environments such as anticipated in fusion reactors. Other environments where $MgAl_2O_4$ would be useful are those which require a stable ceramic matrix such as in nuclear waste containment media or as substrates for optical devices manufactured using ion implantation. This resistance to radiation has been attributed to its structural characteristics, although the reason for this behavior is not fully understood. Proposed mechanisms involve a very high recombination rate of radiation-induced point defects or a very difficult formation of dislocation loops. In any case, it seems to be related to an exceptional tolerance of this material toward a high concentration of intrinsic defects even in the absence of radiation.

One example of this tolerance is that up to 30% cation antisite disorder have been found to occur in synthetic spinel crystals, inducing a very high concentration of traps for electrons (Al^{3+} in tetrahedral symmetry sites) and holes (Mg^{2+} in octahedral symmetry sites) [5]. Another example is that $MgAl_2O_4$ crystals always exhibit some significant deviation from stoichiometry, i.e. the composition can be described as $(MgO)(Al_2O_3)_x$ with x close to but not exactly 1.0. Thus cation vacancies, mainly of tetrahedral type, are formed to compensate for the extra charge of Al^{3+} ions [6]. After high dose neutron irradiation it has been observed that the nucleation and growth of defect clusters is greatly inhibited, whereas the number of antisite defects increases enormously, in sharp contrast to the radiation response observed in other ceramic oxides [2, 7-9].

The present work is a continuation of an experimental series in which an extensive characterization was performed on stoichiometric $MgAl_2O_4$ spinel specimens that were irradiated at high temperatures to very high neutron exposures (50 to 200 dpa) in the FFTF fast reactor. In previous work the effect of irradiation temperature and total dose on stoichiometric spinels has been studied, with emphasis on point defect characteristics, using characterization techniques such as optical absorption, photoluminescence, electron paramagnetic resonance, electrical conductivity and others

*Pacific Northwest National Laboratory (PNNL) is operated for the U.S. Department of Energy by Battelle Memorial Institute under contract DE-AC06-76.

[10-12]. These specimens have also been characterized using neutron diffraction [8], as well as mechanical and elastic properties [3, 4] and electron microscopy [5, 13].

It has been observed that these irradiations induced a large increase in the optical absorption, mainly in the ultraviolet-visual range as well as in some EPR bands. Generally speaking, the optical absorption increases in intensity with dose and decreases with increasing irradiation temperature. To gain more information about the details of these radiation-induced changes, it is desirable to study the annealing behavior of the radiation effects as a function of temperature. In particular, we report in this paper the results of a detailed study of annealing effects on both the optical absorption and electron paramagnetic resonance (EPR) spectra.

Experimental Details

The specimens studied were [100] oriented stoichiometric spinel single crystals from Union Carbide Corporation, in the form of 4.8 mm diameter cylindrical pellets. The details of impurity levels, specimen fabrication and irradiation are given in [3]. The specimen was irradiated in the Materials Open Test Assembly in the Fast Flux Test Facility (FFTF/MOTA) at a nominal temperature of 405°C to a total fluence of 5.3×10^{26} n/m² ($E > 0.1$ MeV), producing ~50 dpa. After irradiation, thin slices with thickness between 0.2 to 0.5 mm were cut and polished from the cylinders. The specimens were heated to 300°C to release all charges retained in shallow traps.

Optical absorption measurements were made at room temperature with a Cary 5E spectrometer between 3300 and 200 nm. EPR spectra were obtained with a Bruker spectrometer model ESP 300E working in the X-band. Accurate values of the microwave frequencies and magnetic fields were obtained with a Hewlett-Packard HP5342A frequency meter and a Bruker ER35 M gaussmeter, respectively. All spectra were measured with a modulation frequency of 100 kHz and modulation amplitude of 0.5 Gauss.

Some low dose X-ray irradiations were also performed at room temperature through a 1 mm thick aluminium plate at about 0.5 Gy/s with a Siemens Kristalloflex 2H (tungsten anode) operated at 50 kV and 30 mA. The purpose of these irradiations was to assist in the identification of the defect types created by neutron irradiation.

Annealing was performed in air, using a conventional air-cooled oven able to reach 1200°C. The ramp rate up to the maximum temperature and down to room temperature is 10 C/min. The stabilization time at high temperature was ~30 min.

Results and Discussion

Optical Absorption Measurements

Figure 1 shows the optical absorption spectra obtained after different annealing temperatures. Before the first annealing step, the observed spectrum shows very high absorption for energies over 34,000 cm⁻¹ (4.22 eV) and a peak at around 19,500 cm⁻¹ (2.42 eV). These results are in close agreement with those of previous studies [10].

The first annealing step was made at a temperature around 400°C close to the nominal irradiation temperature of 405°C. No annealing effect should be expected at temperatures lower than the irradiation temperature. As can be observed in Fig. 1, increasing the annealing temperature from 393 to 760°C induces a significant decrease in the magnitude of the optical absorption spectra, but the decrease is not uniform for all wavelengths. Clearly, it can be observed that the intensities at absorption energies below 46,000 cm⁻¹ anneal out faster than those in the deep UV range.

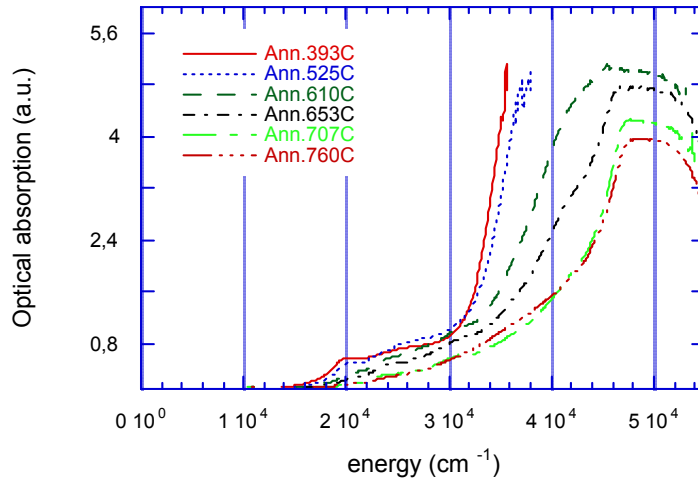


Fig. 1. Room temperature optical absorption spectra of neutron-irradiated MgAl_2O_4 annealed to temperatures between 400 and 760°C.

During annealing it is possible to observe that the measured optical absorption spectra are related to the presence of a number of different absorption bands. To improve the visibility of these bands Fig. 2 shows the difference spectra between the different annealing steps and the final step (after annealing at 760°C). This figure allows us to identify the optical absorption bands that are modified by the annealing process. The main annealing effect is related to the decrease of the intensity of a band around $42,000 \text{ cm}^{-1}$ (5.21 eV). In addition, annealing of optical absorption bands at $19,500$ (2.42 eV), $28,000$ (3.47 eV) and $46,000 \text{ cm}^{-1}$ (5.70 eV) was also observed.

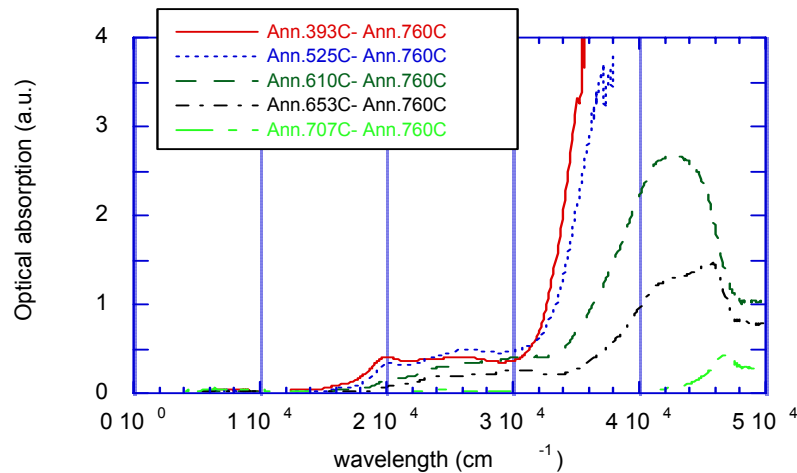


Fig. 2. Difference between the optical absorption spectra of neutron-irradiated MgAl_2O_4 annealed at different temperatures and the spectrum obtained after the 760°C annealing.

For temperatures higher than 760°C the specimen surface was degraded by reaction with the inner materials of the oven (mainly some kind of alumina), developing a white coating at the surface that precludes further optical measurements. This coating is now under study.

It is interesting to note that the band at $42,000 \text{ cm}^{-1}$ has been also observed in neutron irradiated samples at lower doses and room temperature [14-17]. This band has been related to the presence of

F centers. Bands at $27,000\text{ cm}^{-1}$ and $18,800\text{ cm}^{-1}$ were also observed in these studies. These bands can be considered to be similar to those observed in this current work at $28,000$ and $19,500\text{ cm}^{-1}$, specially taking into account the fact that they are complex bands probably associated with defects with slightly different distorted surroundings [16, 18, 19]. Therefore, in the case of very high dose and high temperature irradiation, it seems reasonable to assume that these bands can appear at slightly different positions.

From comparison of our observed spectra with that observed in [14], it is quite clear that the relative height of the ultraviolet absorption compared with the one at $19,500\text{ cm}^{-1}$ is very similar, whereas the height of the bands in the region around $25,000\text{--}30,000\text{ cm}^{-1}$ are quite different. This suggests that the dose and temperature dependencies of the $19,500\text{ cm}^{-1}$ band and the ultraviolet absorption are similar, whereas the intensities of the other bands saturate at much lower doses.

Therefore, it seems that the defect responsible for absorption at $19,500\text{ cm}^{-1}$ is related to the defect responsible for the main ultraviolet absorption. It is also possible to observe that the annealing of the band at $19,500\text{ cm}^{-1}$ appears before the main annealing step since this band was not detected after the 610°C annealing. This behavior is also observed in the annealing process described in [14] but at a completely different temperature (in this work the $18,800\text{ cm}^{-1}$ band is only observed below 450°C). Again, this suggests that the band at $19,500\text{ cm}^{-1}$ is closely related to the ultraviolet bands. Taking into account that the ultraviolet bands are related to the oxygen vacancy defects (mainly F centers) it seems reasonable to relate the $19,500\text{ cm}^{-1}$ band to some oxygen vacancy defect, probably small clusters of two or three vacancies (giving rise to F2 or F3 defects). This proposal is further supported when taking into account that these type of defect also appears in the same energy region for Al_2O_3 or MgO [18, 20], and that they anneal out before the main F center annealing step.

At this point, it is important to note that these results suggest the presence of F centers in the irradiated material up to temperatures of 700°C . This is considered to be a very high temperature for stable F centers. For low dose, low temperature irradiations it has been found that optical bands related to V-centers anneal out for temperatures below 300°C [16, 21-23], whereas bands related to F centers usually anneal out below 500°C [14, 16, 22]. Similar results have been observed for annealing of damage produced in low-dose, low-temperature irradiations using electrons or ions [24]. Measurements of the vacancy centers during annealing made using other techniques such as positron annihilation [24] or length change [25] also provide similar information.

On the other hand, the annealing of specimens after high-dose, high-temperature irradiation shows a different behavior. From transmission electron microscopy studies it was observed that radiation-induced dislocation loops start to shrink around 725°C and completely disappear at 1200°C , whereas cavities grew slightly around 1300°C and then began to shrink with increasing annealing temperature [13]. Unfortunately, for these irradiation conditions there are no corresponding optical data.

For other irradiation conditions, such as high-dose, low-temperature irradiation, there are no neutron data, but some qualitative information can be obtained by analysing ion implantation results. In this case, the thermal annealing of radiation damage for ion implanted materials reaching the amorphization level shows that the crystallinity of the specimen recovers in a wide step starting at around 600°C and almost fully recovers by 1200°C [26]. This recovery behavior has been previously ascribed to the dissociation of defect clusters.

From these observations it can be concluded that in low-dose irradiations, vacancy centers in MgAl_2O_4 anneal out below 500°C in a process regulated by the mobility of point defects, whereas in high-dose irradiations, vacancy-related centers (such as the F center) can be observed at very high temperatures and their thermal stability is controlled by the thermal stability of defect clusters.

In addition to these bands, the data presented in Figs. 1 and 2, allow us to identify a band around $48,000\text{--}50,000\text{ cm}^{-1}$ that seems to anneal out at much higher temperatures. This band has not been previously observed in low-temperature, low-dose irradiations.

In summary, optical absorption spectrum changes induced by high-dose, high-temperature irradiation are composed of absorption bands at $50,000$, $46,000$, $42,000$, $28,000$ and $19,500\text{ cm}^{-1}$. These bands anneal out at different temperatures in the range between 500 and 1000°C .

EPR Results

The EPR spectra at room temperature of the irradiated specimen before the first annealing step consists of a band at $g = 2.0005 \pm 0.0005$, as can be seen in Fig. 3. This type of band does not usually show any dependence on the orientation of the magnetic field with respect to the specimen. Band A is sharp, with a peak-to-peak width of 11 G in the derivative line. These results are in agreement with those previously published [27]. It was suggested earlier that this band could be related to F+ centers [19, 27].

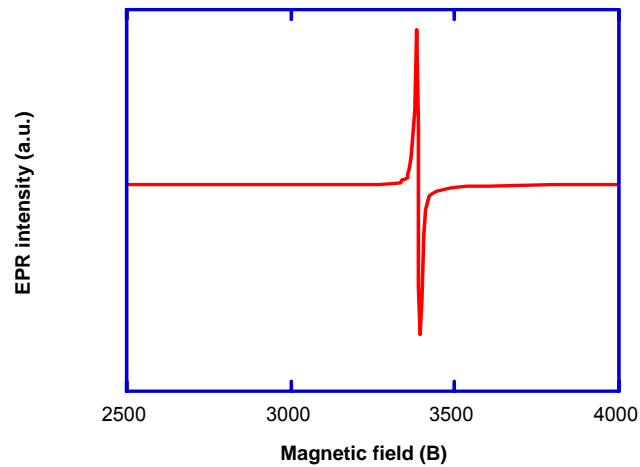


Fig. 3. Typical EPR spectrum obtained at room temperature for the neutron-irradiated MgAl_2O_4 specimen.

During annealing, the height of this band decreases with temperature, almost disappearing after the last heat treatment. Figure 4 shows the height of the measured band as a function of temperature. It is interesting to note that the decrease of the band takes place over the entire temperature range, and the observed behavior is similar to that observed for the $42,000\text{ cm}^{-1}$ absorption band.

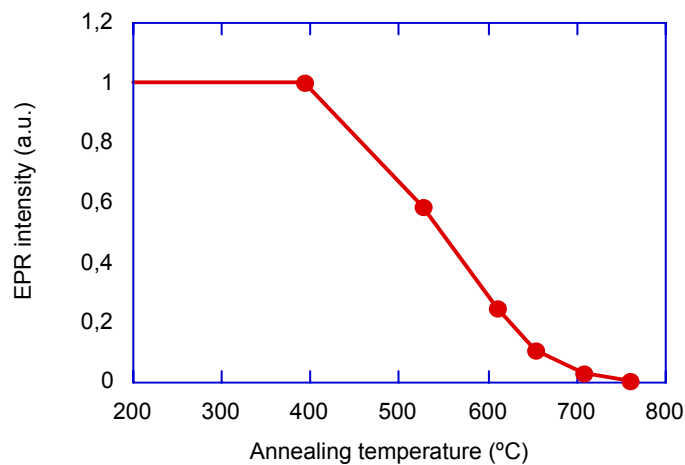


Fig. 4. Dependence on annealing temperature of the intensity of the EPR band measured in the MgAl_2O_4 specimen

Ionizing Radiation Effects

In order to determine if the observed annealing behavior is related to ionic or electronic effects, the samples were irradiated with X-rays after each annealing step, and the EPR and optical absorption properties were then measured both before and after the X-ray irradiation.

Before thermal annealing, no change of the spectra was found if a small level of X-ray irradiation was applied to the specimen. This is a very interesting result because before neutron irradiation, X-ray irradiation gives rise to a very characteristic and intense EPR spectra associated with the trapping of holes in cation vacancies (V-centers) [22]. The lack of this band in the optical and EPR spectra of neutron-irradiated specimens should indicate that there are no cation vacancies available, although this is unlikely taking into account that their concentration is very high even in the starting material, or that these vacancies are distorted in such a way that they cannot stabilize the holes at the cation sites. A similar mechanism has been suggested to explain the higher sensitivity to gamma irradiation of stoichiometric single crystal compared with non-stoichiometric ones [28]. This proposal is further supported by the results obtained for other neutron irradiations at lower doses and lower temperatures in which it has been observed that the V centers related optical and EPR characteristics are distorted by the irradiation and can be recovered after thermal annealing [14]. Most importantly, it should be noted that no recovery was observed in our case.

For X-ray irradiations made after annealing over 525°C there is clearly observed an increase of the absorption spectra after irradiation. In this case, as well as all the other annealing steps at higher temperatures, the dose dependence and the low temperature annealing of the ionizing radiation effect have been studied. In general, there is observed an increase of the optical absorption, mainly in the region around 37,000 cm⁻¹ (4.59 eV) and also around 19,000 cm⁻¹. Figure 5 shows the increase of the optical absorption induced by different X-ray irradiations (i.e. the difference between the optical absorption spectra after and before X-ray irradiation) for the 610°C annealing step. It can be observed that the effect shows saturation behavior. The observed increase in optical absorption anneals out at temperatures below 400°C in a wide annealing step process that starts at room temperature and finishes around 400°C, similar to the annealing behavior observed for V-centers [22]. At the same time, it is observed that the previously mentioned EPR band also increases after X-ray irradiation and decreases during thermal annealing. Figure 6 shows the dose and temperature dependence of both processes for the optical absorption at 37,000 cm⁻¹ and for the EPR band. It can be clearly observed that both bands behave in a similar way, indicating that they are closely related. In many papers this optical band has been related to the presence of F⁺ centers [14-23]. Taking this relationship into account, it can be clearly concluded, for the first time, that the observed EPR band is associated with F⁺ centers.

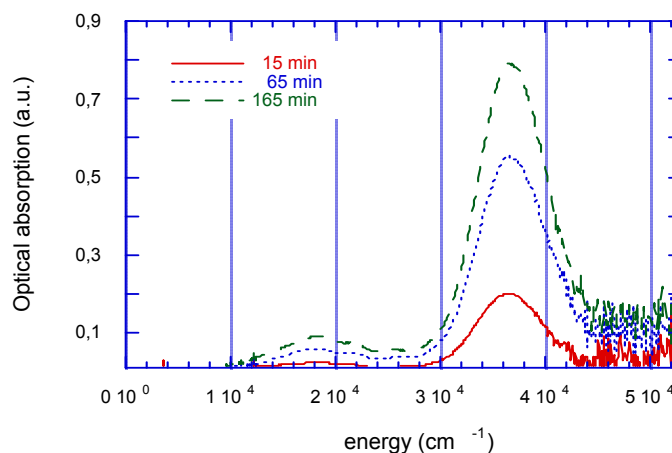


Fig. 5. Effects of different X-ray irradiations on the optical absorption spectra of neutron-irradiated MgAl₂O₄ specimen annealed at 610°C.

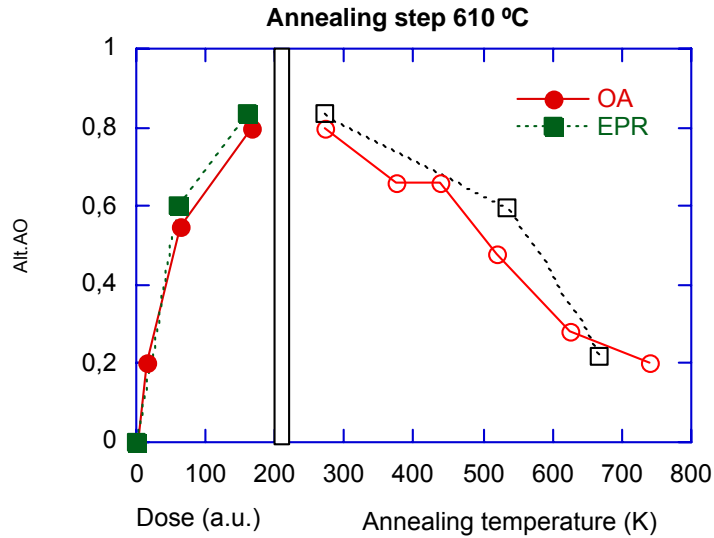


Fig. 6. Dependence on dose and thermal annealing of the X-ray effect on the neutron-irradiated MgAl_2O_4 specimen annealed at 610°C . (O) behavior of the optical absorption band at $37,000\text{ cm}^{-1}$ (\square) behavior of the EPR band. Open symbols relate to the thermal annealing experiment and filled symbols relate to the dose dependence study.

Conclusions

The thermal annealing of the EPR and optical absorption characteristics of a MgAl_2O_4 specimen that was neutron-irradiated to 50 dpa at $\sim 405^\circ\text{C}$ has been studied. It was found that the main characteristics of both EPR and optical absorption spectra anneal out between 400 and 800°C . Both F and F+ centers are found to persist up to very high temperatures (over 700°C), suggesting the operation of an annealing mechanism based on evaporation from extended defects. It has also been demonstrated that a sharp EPR band with $g=2.0005$ in these irradiated specimens is related to the presence of F+ centers.

Acknowledgments

This work was performed in the framework of CIEMAT projects for Nuclear Fusion Research and was partly supported by European Union within the European Fusion Technology Programme and by the CICYT (Spain) under contract number FTN2003-03855. The neutron irradiation and the participation of F.A. Garner were performed under the sponsorship of the U.S. Department of Energy, Office of Fusion Energy under Contract DE-AC06-76RLO 1830.

References

- [1] F. W. Clinard, Jr., G. F. Hurley, R. A. Youngman, and L. W. Hobbs, *J. Nucl. Mater.* 133-134 (1985) 701.
- [2] S. Zinkle and C. Kinoshita, *J. Nucl. Mater.* 251 (1997) 200.
- [3] F. A. Garner, G. W. Hollenberg, F. D. Hobbs, J. L. Ryan, Z. Li, C. A. Black, and R. C. Bradt, *J. Nucl. Mater.* 212-215 (1994) 1087.
- [4] C. A. Black, F. A. Garner, and R. C. Bradt, *J. Nucl. Mater.* 212-215 (1994) 1096.
- [5] R. I. Sheldom, T. Hartmann, K. E. Sickafus, A. Ibarra, D. N. Argyriou, A. C. Larson, and R. B. von Breele, *J. Am. Ceram. Soc.* 82 (1999) 3293.
- [6] T. Soeda, S. Matsumura, C. Kinoshita, and N. J. Zaluzecc, *J. Nucl. Mater.* 283-287 (2000) 952.
- [7] K. Fukumoto, C. Kinoshita, and F. A. Garner, *J. Nucl. Sci. Tech.* 32 (1995) 773.

- [8] K. E. Sickafus, A. C. Larson, N. Yu, M. Nastasi, G. W. Hollenberg, F. A. Garner, and R. C. Bradt, *J. Nucl. Mater.* 219 (1995) 128.
- [9] K. E. Sickafus, N. Yu, and M. Nastasi, *Nucl. Instr. Methods Phys. Res. B* 116 (1996) 85.
- [10] A. Ibarra, R. Vila, and F. A. Garner, *J. Nucl. Mater.* 233-237 (1996) 1336.
- [11] A. Ibarra, F. A. Garner, and G. L. Hollenberg, *J. Nucl. Mater.* 219 (1995) 135.
- [12] A. Ibarra, D. Bravo, M. A. Garcia, J. Llopis, F. J. Lopez, and F. A. Garner, *J. Nucl. Mater.* 258- 263 (1998) 1902.
- [13] K. Yasuda, C. Kinoshita, and F. A. Garner, *J. Nucl. Mater.* 283-287 (2000) 937.
- [14] A. Ibarra, D. Bravo, F. J. Lopez, and I. Sildos, *Mater. Sci. Forum* 239-241 (1997) 595.
- [15] G. P. Summers, G. S. White, K. H. Lee, and J. R. Crawford Jr., *Phy. Rev. B* 21 (1980) 2578.
- [16] L. S. Cain, G. J. Pogatshnik, and Y. Chen, *Phys. Rev. B* 37 (1988) 2645.
- [17] V. T. Gritsyna, J. V. Afanasyev-Charkin, V. A. Kobayakov, and K. E. Sickafus, *J. Nucl. Mater.* 283-287 (2000) 927.
- [18] M. J. Springis and J. A. Valbis, *Phys. Stat. Sol.* 8b9 132 (1985) K61.
- [19] V. T. Gritsyna and V. A. Kabyakov, *Sov. Phys. Tech. Phys.* 30 (1985) 206.
- [20] L. S. Welch, A. E. Hughes, and G. P. Pells, *J. Phys. C: Sol. Stat. Phys.* 13 (1980) 1805.
- [21] V. T. Gritsyna, I. V. Afanasyev-Charkin, V. Kobayakov, and K. E. Sickafus, *J. Am. Ceram. Soc.* 82 (1999) 3365.
- [22] A. Ibarra, F. J. Lopez, and M. Jimenez de Castro, *Phys. Rev. B* 44 (1991) 7256.
- [23] G. S. White, K. H. Lee, and J. R. Crawford Jr., *App. Phys. Lett.* 35 (1979) 1.
- [24] J. He, L. Lin, T. Lu, and P. Wang, *Nucl. Instrum. Method. B* 191 (2002) 596.
- [25] T. Yano, A. Insani, H. Sawada, and T. Iseki, *J. Nucl. Mater.* 258-263 (1998) 1836.
- [26] C. G. Lee, Y. Takeda, and N. Kishimoto, *Nucl. Instrum. Method. B* 191 (2002) 591.
- [27] A. Ibarra, D. Bravo, M. A. Garcia, J. Llopis, F. J. Lopez, and F. A. Garner. *J. Nucl. Mater.* 258-263 (1998) 1902.
- [28] N. Mironova, V. Skvortsova, A. Smirnov, and U. Ulmanis, *Sov. Phys. Solid State* 34 (9) 1492 (1992).

8.0 BREEDING MATERIALS

No contributions.

**9.0 RADIATION EFFECTS, MECHANISTIC STUDIES,
AND EXPERIMENTAL METHODS**

MULTISCALE MODELING OF DEFECT GENERATION AND EVOLUTION IN METALLIC ALLOYS FOR FUSION POWER—Jörg Rottler, David J. Srolovitz, and Roberto Car (Princeton Institute for the Science and Technology of Materials, Princeton University)

OBJECTIVE

This work aims at creating a computational framework that is capable of describing the microstructural evolution of metallic alloys under irradiation on length scales reaching from the atomistic to the continuum. We focus explicitly on the annealing kinetics of elemental point defects (self-interstitials and vacancies) generated in high-energy collision cascades. To study the defect dynamics, we employ molecular dynamics and kinetic Monte Carlo simulations in combination with continuum rate equations. We begin by first considering pure bcc metals and then extend our study to the effects of alloying.

SUMMARY

We perform an analysis of the time evolution of self-interstitial atom and vacancy (point defect) populations in pure bcc metals under constant irradiation flux conditions. Mean-field rate equations are developed in parallel to a kinetic Monte Carlo (kMC) model. When only considering the elementary processes of defect production, defect migration, recombination and absorption at sinks, the kMC model and rate equations are shown to be equivalent and the time evolution of the point defect populations is analyzed using simple scaling arguments. We show that the typically large mismatch of the rates of interstitial and vacancy migration in bcc metals can lead to a vacancy population that grows as the square root of time. The vacancy cluster size distribution under both irreversible and reversible attachment can be described by a simple exponential function. We also consider the effect of highly mobile interstitial clusters and apply the model with parameters appropriate for vanadium and iron.

PROGRESS AND STATUS

We implemented a general kinetic Monte Carlo (kMC) model that represents Frenkel pair production, point defect diffusion, defect recombination and absorption at sinks in bcc metals. Of particular importance in our study is the mixed 1D/3D nature of self-interstitial diffusion in bcc metals [1]. We study the consequences of this 1D/3D random walk for the evolution of the point defect distributions with explicit kMC and arrive at excellent agreement with analytical scaling predictions. The elemental model is then solved with kMC and shown to be equivalent to a set of classic rate equations. Figure 1 shows the time evolution of interstitial and vacancy populations n_i and n_v for several different values of the production rate. Up to four distinct scaling regimes appear that can be easily described through the corresponding rate equations. Two of these are steady state regimes in which defect production is balanced by a combination of loss processes. Most interesting, however, is a non-steady state regime in which the vacancy density does not increase linearly with time but as the square root of time.

We then include vacancy clustering into our model and compute the time-dependent cluster size distribution in a point defect “gas”. We find a simple, general exponential expression (see Fig. 2) that is a consequence of the continuous diffusive arrival of vacancies attaching to clusters and interstitials recombining with them. Other aspects of this study include the effect of highly mobile self-interstitial clusters, which is shown to anneal quickly at early times. In the final part of the study, we apply the model to vanadium and alpha-iron in which the diffusivities were determined using molecular dynamics simulations. Interestingly, our model predicts that the point defect kinetics in these two metals are very similar, despite large differences in the specific values of the energy barriers for interstitial and vacancy migration between these metals. While explicit kMC simulations can accurately capture the early dynamical regimes in the sub-dpa region, it is not feasible to extend these simulations to the macroscopic time scales of interest. Hence, properly

parametrized rate equations must be used. This work has been summarized in a research article currently submitted for publication [2].

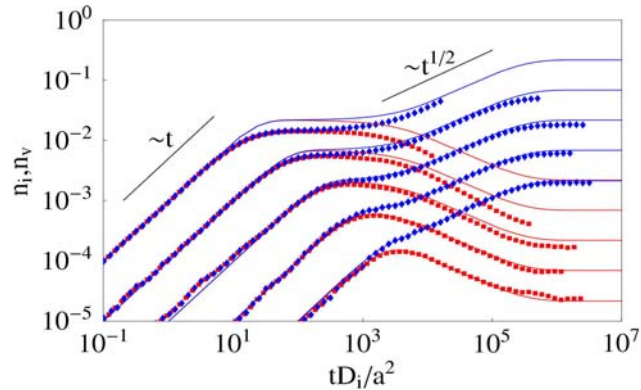


Fig. 1. Self-interstitial (red squares) and vacancy (blue diamonds) densities as a function of time for several different ratios of the interstitial hopping rate to the production rate (increasing from top to bottom). The solid lines show the result of direct numerical integration of continuum rate equations and the symbols correspond to the results of the kMC simulations in a periodic simulation cell.

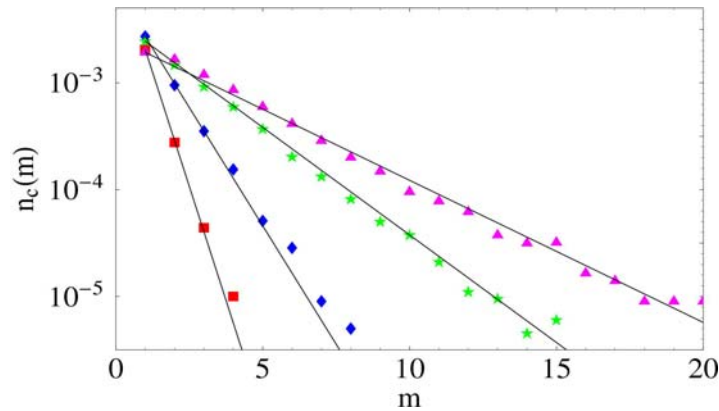


Fig. 2. Plot of the vacancy cluster size distribution found from the kMC simulations at four different times (time increasing from red to purple). The latest distribution corresponds to steady state. The straight lines show a simple analytic prediction $n_v(t)^m / (\text{const } n_i(t))^{(m-1)}$, where m is the number of vacancies in the cluster and the constant depends on the relevant ratios of production and hopping rates.

Based on our kMC simulation for pure metals, we have begun studies of models for diffusion in alloys. Impurity atoms must lead to a local modification of the defect hopping rates. We initially considered two different types of models [3] suitable for an implementation into lattice kMC:

- a “trap-model” (see Fig. 3), in which the hopping rates only depend on the initial position of the point defect, and
- a “barrier-model” (see Fig. 4) in which the hopping rate depends on the direction of defect motion (the link between two sites) and therefore on the initial and final defect position.

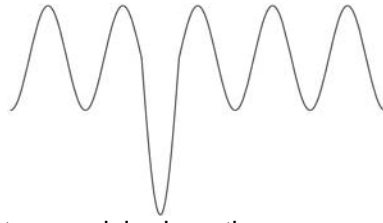


Fig 3. Energy landscape in a trap model, where the escape rate is increased at the impurity site.

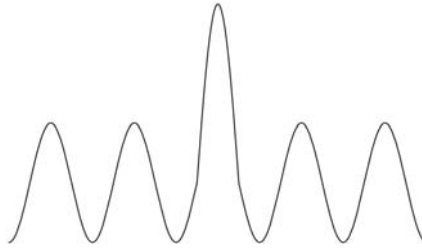


Fig 4. Energy landscape in the barrier model, where the hopping rates depend on the direction of motion near an impurity.

The most important difference between these two models is that the “barrier-model” induces correlations in the random walk, while the “trap-model” does not. For the trap model, one can therefore easily compute a total effective hopping rate by averaging over the total number of inverse hopping rates occurring in the system. For the “barrier-model,” one can obtain a mean hopping frequency by directly averaging over all hopping rates, but the effective diffusivity is modified by a suitable correlation factor. The value of the correlation factor depends on the details of lattice geometry and hopping frequencies, and its computation represents the major challenge to describing diffusion in alloys.

Typical theories of vacancy assisted diffusion in alloys focus on models of the barrier type, and methods to compute the correlations are well established [4]. The simplest model, for instance, considers only two frequencies, one for vacancy-solvent exchange and one for vacancy-solute exchange regardless of the local environment. More complicated models such as the “five-frequency-model” are often considered for fcc metals. Somewhat less explored than vacancy diffusion is self-interstitial diffusion, because it is usually only relevant in radiation environments. Here the presence of solute atoms may not only modify the (usually very low) migration barriers, but may also affect the rotation frequencies. There is, therefore, a greater need to identify suitable models that capture the most relevant frequencies.

Work in progress therefore includes the implementation of some of the standard models for vacancy and self-interstitial diffusion in alloys into our kMC framework for bcc metals. As in the pure metals, we begin with the simplest models and then include more processes. Unlike in conventional diffusion studies, the focus here is on the transport of the defects themselves rather than on the self- and solute diffusivities. Also, the presence of defect production and annihilation may induce interesting dynamical effects on the alloy structure such as demixing or precipitation. Our objectives are, therefore, twofold:

- determine the effective diffusivities and the resulting modifications of the annealing kinetics of point defects in impurity rich environments
- study the time dependent effects of defect production, recombination and absorption on alloy composition and structure.

Once the general methodology is established, we will use EAM-type potentials to compute static exchange frequencies for specific ferritic alloys of interest, e.g, FeCr. Molecular dynamics of single self-interstitial diffusion will also be employed, as appropriate.

References

- [1] L. Zepeda-Ruiz, J. Rottler, S. Han, G. Ackland, D. J. Srolovitz, and R. Car, *Strongly non-Arrhenius self-interstitial diffusion in vanadium*, Phys. Rev. B, in press.
- [2] J. Rottler, D. J. Srolovitz, and R. Car, *Point defect dynamics in bcc metals*, submitted to Phys. Rev. B.
- [3] K. W. Kehr and T. Wichmann, Mater. Science Forum 223 (1996) 151.
- [4] A. R. Allnatt and A. B. Lidiard, Atomic Transport in Solids, Cambridge (1993).

IN-SITU TEM STUDY ON THE COLLAPSE PROCESS OF SFT DURING PLASTIC DEFORMATION—Y. Matsukawa, Yu. N. Osetsky, R. E. Stoller, and S. J. Zinkle (Oak Ridge National Laboratory)

OBJECTIVE

The objective of this research is to obtain the information about the collapse process of stacking fault tetrahedra (SFTs) during plastic deformation by in-situ straining experiments in a transmission electron microscope (TEM).

SUMMARY

Dynamic observation of the collapse process of SFTs during plastic deformation in quenched gold was carried out using a TEM. SFTs having perfect pyramid structure were collapsed by direct interaction with gliding screw dislocations. Although Wirth et al. pointed out that truncation of SFT before interaction with gliding dislocations was an important factor for the SFT collapse [1], the present experimental results clearly showed that truncation of SFT was not a crucial factor for the collapse mechanism. An SFT collapsed in a unique way: only the base portion divided by the gliding plane of dislocation annihilated, while the apex portion remained intact. Judging from the fact that similar collapse process was observed in recent computer simulations using molecular dynamics codes [2], this collapse process is a major one. However, it is still unclear whether this is only one process for SFT collapse, because this collapse process leaves a small SFT as a remnant, whereas SFTs are completely swept out in the dislocation channels actually observed in the deformation microstructure of irradiated fcc metals [3-12]. Further research works will be required for fully understanding of dislocation channeling, which is believed to be a key for ductility reduction of irradiated metals [3].

PROGRESS AND STATUS

Introduction

Recent improvements in resolution of transmission electron microscope (TEM) have established that small defect clusters ($\leq 2\text{nm}$) in the microstructure of neutron irradiated pure fcc metals, so called 'black dots', are in many cases stacking fault tetrahedra (SFTs) [13-15]. Thus, there is substantial

interest in the interaction of SFT with gliding dislocations as a key in atomistic scale mechanism for variation of mechanical properties of fcc metals in nuclear reactor environments.

The SFT is a vacancy-type defect cluster having a complex crystallographic geometry: the tetrahedral outer shape consists of intrinsic stacking faults with displacement vectors $R=1/12\langle 111 \rangle$ on four crystallographically equivalent $\{111\}$ planes, and the edges of the tetrahedron are composed of sessile stair-rod dislocations with Burgers vector of $b=1/6\langle 110 \rangle$ [16]. The complex structure indicates that SFTs are highly stable under shear stress. However, defect-free regions (dislocation channels) are created locally as deformation progresses in both quenched and irradiated metals [4-12]. This has led to great interest in resolving how SFTs annihilate during plastic deformation and dislocation channels are created.

There are two proposed annihilation mechanisms: (1) annihilation due to large stress fields, associated with localized deformation, and (2) annihilation by direct interaction with individual dislocations, which would operate in a heterogeneous manner and lead to formation of defect-free slip bands. Regarding the former idea, Hiratani et al. investigated the stability of a SFT by numerical analysis based on elasticity theory for the stress field of a glide dislocation [17]. Their calculation showed that the stress field from a single dislocation could never annihilate an SFT. However, in the situation where there is localized deformation, large numbers of dislocations would form a dislocation pile-up, resulting in high stress field at the pile-up front, which could favor destabilization of SFT. Further investigation is necessary to determine the importance of this mechanism. Regarding the second idea, Kimura and Maddin approached this issue forty years ago from the viewpoint of dislocation reactions [18-19]. However, the validity of this model remains unclear because of a lack of experimental evidence.

Recent molecular dynamics computer simulations have investigated the dynamic interaction of a SFT with gliding dislocations [1, 2]. Wirth et al. showed that an SFT remained intact even after multiple (up to 6) interactions with a gliding dislocation [1]. However, an overlapping truncated SFT configuration was annihilated by interactions with a single gliding edge dislocation. These authors concluded that the perfection of the SFT, i.e. perfectly formed or truncated, is an important factor for SFT collapse. However, more recently, Osetsky et al. showed an SFT having perfect pyramid shape collapsed by gliding dislocations [2]. Based on the information obtained by these computer simulations, the crucial factor for SFT collapse has been discussed. Against this background, assessments by experiments using real materials have been expected.

The most direct experimental method for investigation of the SFT annihilation involves in-situ straining experiments using a transmission electron microscope (TEM). There are several reports based on in-situ straining experiments performed on ion and/or neutron irradiated fcc metals [8-12]. However, the size of SFT introduced by ion/neutron irradiation is small ($< 2\text{nm}$), comparable to the resolution limit of TEM in the diffraction contrast imaging techniques [20]. As a result, few experimental data are available to identify the detailed interaction process with gliding dislocations leading to collapse of SFTs.

In the present study, an in-situ straining experiment has been carried out on SFTs introduced into gold by quenching. SFT size can be controlled relatively easily in quenching: from more than 100nm to less than 2nm [21]. Information obtained by direct observation allows insight of the annihilation process of SFT.

Experimental Procedure

SFTs were introduced into 99.9975% purity gold specimens, whose thickness was $100\ \mu\text{m}$, by quenching from 1273K in an open vertical furnace to 233K in CaCl_2 solution. As addressed elsewhere, a key parameter controlling the size of SFT was annealing time at 1273K . The specimens in the present experiments were all kept at 1273K for 1hr. Since vacancies are mobile at room temperature in gold, the thermal history after quenching also affects the formation behavior of SFT [21]. The specimens were kept at 233K for 1hr, then at 298K for 2hr, and finally at 373K for 1hr, before electro-polishing. Tensile specimens for in-situ straining experiments had a rectangular shape ($10\ \text{mm} \times 2.5\ \text{mm} \times 100\ \mu\text{m}$), and the central section was electro-polished by the twin jet method. Electrolytic solution for the polishing was KCN 67 g/l water solution, and the polishing temperature was 276K . In-situ straining experiments were carried out at room temperature. The electron microscope accelerating voltage was 200kV , which introduces negligible irradiation damage in gold. An FEI Tecnai20 TEM with Twin pole piece was used for the in-situ straining tests, with a GATAN Model 671 single tilt cooling straining stage. The crosshead speed of the straining holder is variable ranging from 0.01 to $1\ \mu\text{m/s}$. Motion pictures of the in-situ straining were captured with a GATAN Model 622 camera, at a frame rate of 30 frames/s, recorded on DV tapes, and then computer processed.

Results

The SFTs introduced by quenching are essentially perfect pyramid shape without any truncation. Although some truncated SFTs are also present in Fig. 1(A2, A3, B2), their truncation style is entirely different from the style predicted by Silcox and Hirsch [22]: the truncated SFT in their model is missing the top portion of the tetrahedron, while the truncated SFTs in Fig. 1 are all missing portions of their edge region. The truncation of the SFTs in Fig. 1 is simply caused by intersection of the specimen surface. We have not observed any cases of truncated SFTs except those created by intersection with the foil surface during specimen preparation by electro-polishing. SFTs grow by absorbing vacancies and forming a so-called V-ledge on the stacking fault planes [23-24]. Thus, nearly all SFTs should inevitably have ledges of one atomic layer thickness on their stacking fault planes. This statement is supported by high-resolution images shown by Ajita et al [16]. However, possession of atomic-layer ledges is an entirely different issue from the truncation where the top

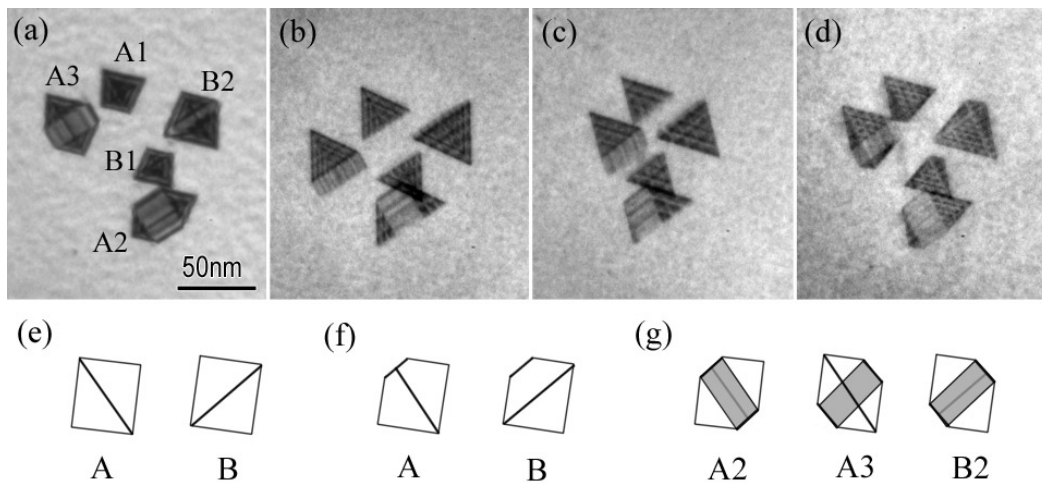


Fig. 1. Typical example of SFTs in quenched gold. Two types of crystallographically equivalent SFTs are indexed as A and B in these figures. A1 and B1 have perfect pyramid shape; however, the others are truncated. The truncation is simply due to intersection by foil surface. A2 and B2 are intersected by a surface, and A3 by another surface. All of the SFTs in quenched gold have essentially perfect pyramid structure. (a) SFTs observed from near $[001]$ zone axis. (b)(c)(d) Observed from directions tilted from (a). (e)(f)(g) Schematic diagrams of SFTs in various conditions observed from $[001]$ zone axis. (e) Image of SFTs without any truncation. (f) Image of SFTs missing a top portion. (g) Image of SFTs missing an edge portion.

portion of the SFT is missing. It is unclear whether an SFT having ledges can be called 'perfect' in the strict sense; however, in what follows these SFTs are called 'perfect' in order to distinguish them from truncated SFTs.

Figure 2 shows the typical collapse process of an SFT by direct interaction with gliding dislocations. Judging from the interaction behavior with the gliding dislocation, both ends of which intersect the foil surfaces, it is clear that the SFT is located at the center of the foil thickness direction. Therefore, this is a perfect SFT without being truncated by foil surface. SFTs collapsed into a smaller SFT. This collapse process is different from any models previously proposed by Kimura, because in those models such small SFT cannot be the remnant of collapse [18-19]. The gliding dislocation intersected the SFT does not have any remarkable jog at the moment of SFT collapse, indicating that the dislocation did not cross-slip on the original SFT as assumed in Kimura's model for screw dislocation, but simply intersected the SFT. The geometry analysis revealed that the smaller SFT corresponds to an apex portion of the original SFT: in other words, only the base portion divided by intersection with the dislocation annihilated, while the top portion intact [25-26]. After the SFT collapse, a vacancy cluster having ambiguous shape was created on the intersected dislocation, then the vacancy cluster developed into a super jog. Judging from that dislocation cross-slip is not involved in the collapse process, this type of SFT collapse may be induced irrespective of dislocation-type: not only by screw but also by edge [26]. Although the SFT was collapsed at the intersection with third dislocation in Fig. 2, the number of intersection would not be the primary factor dominating the collapse process: actually, it was often observed that an SFT was collapsed at the intersection with first dislocation [3, 26].

When an SFT is intersected by a dislocation gliding on the (111), steps are created on the two of three stacking fault planes, which were actually intersected, depending on the Burgers vector of the intersecting dislocation, as schematically shown in Fig. 3. The steps on stacking faults are traditionally called V-ledge and I-ledge [27]: the Burgers vector of the dislocation determines which type of ledge is created on which stacking faults. Fig. 4 is the schematic diagram showing variation of atom configuration for V-ledge and I-ledge. At V-ledge, exactly the same stacking sequence of (111) planes is created as the SFT bottom. However, at I-ledge, a quite unusual atom configuration appears: the atoms on adjacent (111) planes are overlapping each other.

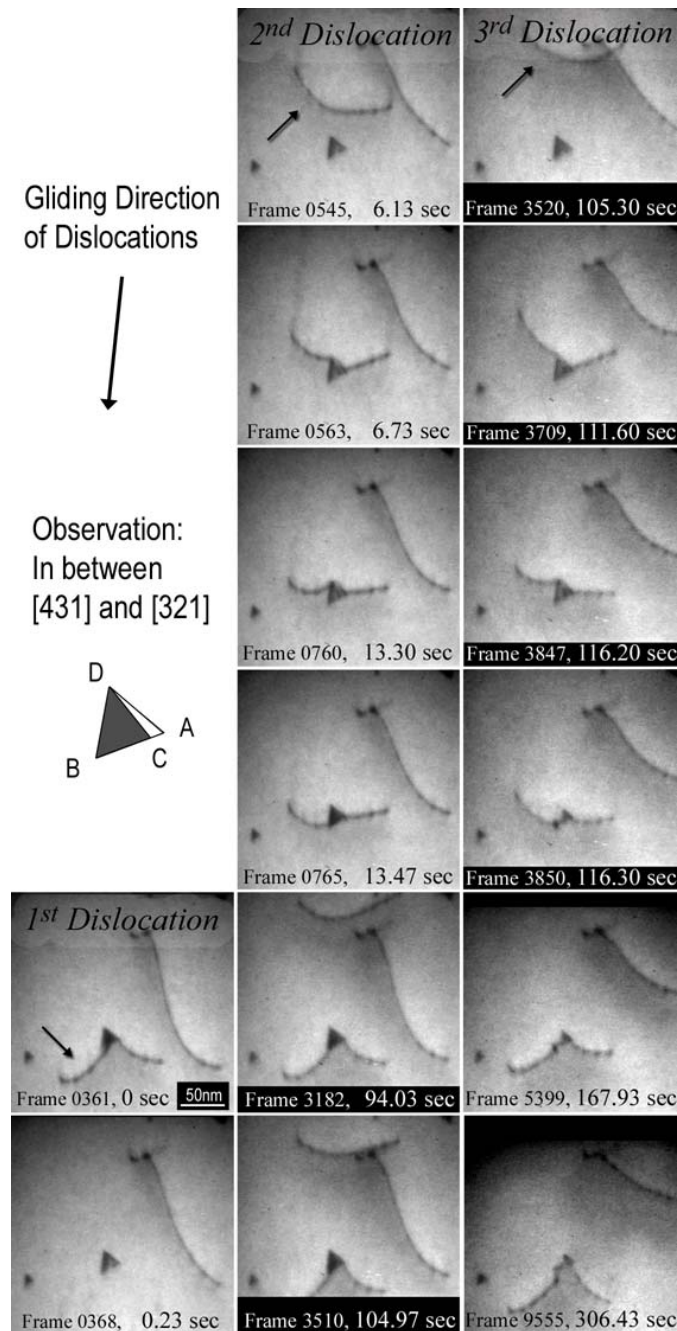


Fig. 2. An example of SFT collapse by gliding dislocations. The SFT collapsed on interaction with the third dislocation. A small SFT and a vacancy cluster were produced by the SFT collapse. The vacancy cluster gradually developed into a super jog on the dislocation collapsed the original SFT. Judging from the interaction behavior with the SFT, dislocations were gliding on $(\bar{1}\bar{1}1)$, i.e. parallel to ABD. The SFT edge length was 27nm, dislocation length was 121nm, and specimen foil thickness was 99nm.

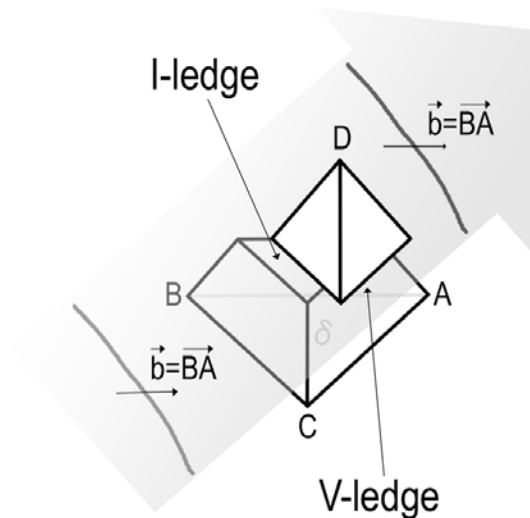


Fig. 3. Intersection by a dislocation produces ledges on two of three stacking fault planes intersected by the dislocation.

This simple assessment of atom configuration in consideration of dislocation's Burgers vector provides a key to understand the SFT collapse process observed in experiments: those overlapping atoms have strong repulsive force that may be the driving force for the SFT collapse. Those overlapping atoms will displace to somewhere to relax the dense configuration. However, at the place where the atom displaced, another dense configuration is created by this displacement. This chain reaction of displacements continues until the displacement finally creates energetically favorable configuration such as Frank loop. An important point in this chain reaction is, judging from the geometry of an I-ledge, that the chain reaction inevitably collapses only the base portion of the SFT. The detail mechanism will be discussed elsewhere [28].

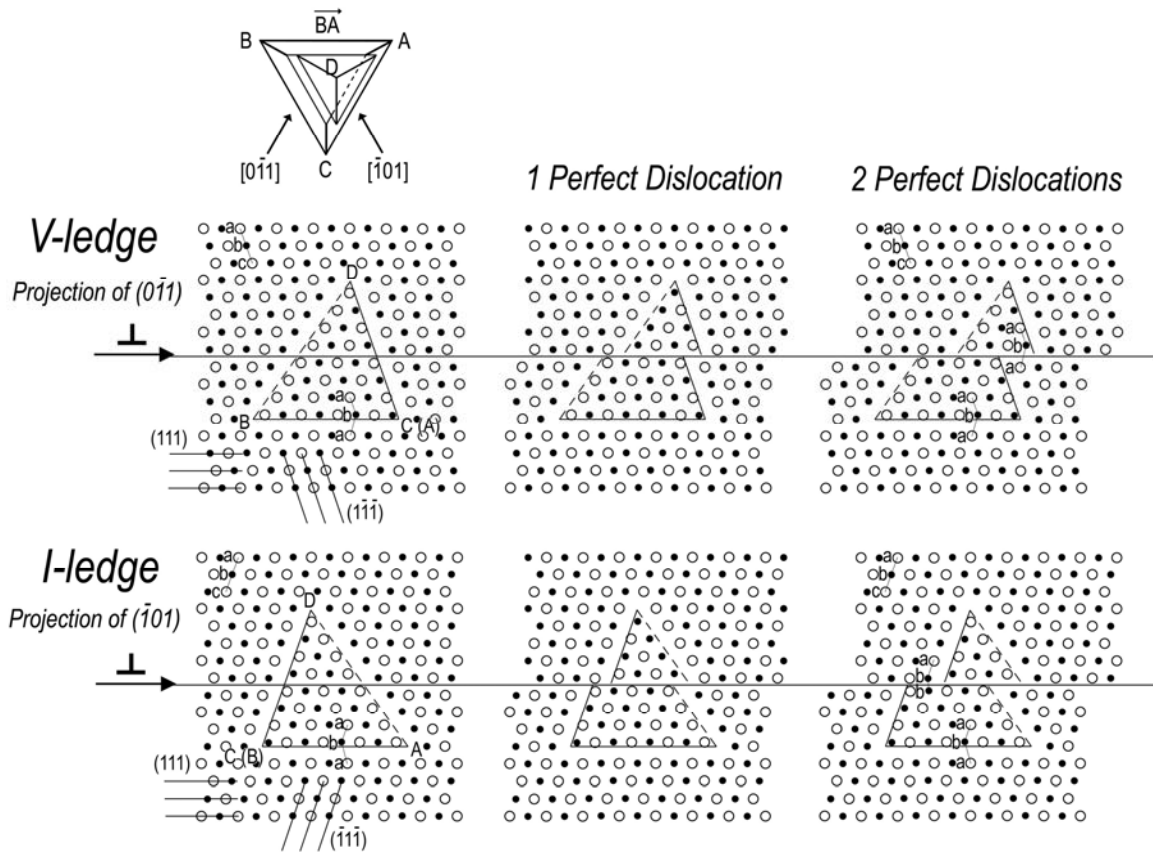


Fig. 4. Variation of atom configuration by intersection with perfect dislocations gliding on a (111) plane, projected on $(0\bar{1}1)$ for V-ledge, and on $(\bar{1}01)$ for I-ledge, respectively. Burgers vector of the intersecting perfect dislocations is $1/2 [\bar{1}\bar{1}0]$. Filled circles represent atoms on a plane $1/4 [\bar{1}01]$ below the open circles.

Acknowledgments

This research was sponsored by the Office of Fusion Energy Sciences, U.S. Department of Energy, under contract DE-ACO5-00OR22725, with UT-Battelle, LLC. We are grateful to Kathy Yarborough for specimen preparation, Cecil Carmichael for furnace operation, and Dr. Neal Evans for maintenance of TEM. Also, we thank Drs. Stas Golubov, Thak Sang Byun, Nao Hashimoto, Joe Horton, and Jim Bentley at ORNL, and Dr. Kazuto Arakawa at Shimane University for valuable comments.

References

- [1] B. D. Wirth, V. V. Bulatov, and T. Diaz de la Rubia, *J. Eng. Mat. Tech.* 124 (2002) 329-334.
- [2] Yu. N. Osetsky, personal communication.
- [3] S. J. Zinkle, N. Hashimoto, Y. Matsukawa, R. E. Stoller, and Yu. N. Osetsky, *MRS Symp. Proc.* 792, Eds., L. M. Wang et al. (Materials Research Society, Warrendale Pa., 2004), R1.1.1-1.1.10.
- [4] M. Meshii and J. W. Kauffman, *Acta Met.* 7 (1959) 180-186.
- [5] M. S. Bapna, T. Mori, and M. Meshii, *Phil. Mag.* 17 (1968) 177-184.
- [6] A. Okada, K. Kanao, T. Yoshiie, and S. Kojima, *Trans. JIM* 30, No. 4 (1989) 265-272.
- [7] S. Yoshida, M. Kiritani, Y. Deguchi, and N. Kamigaki, *Trans. JIM* 9 (supplement) (1968) 83-89.
- [8] J. V. Sharp, *Phil. Mag.* 16 (1967) 77-96.
- [9] H. Saka, K. Noda, K. Matsumoto, and T. Imura, *Proceedings of 4th International Conference on High Voltage Electron Microscopy, Toulouse (1975)* 325-327.
- [10] K. Noda, H. Saka, K. Shiraishi, H. Yoshida, and T. Imura, *Proceedings of 5th International Conference on High Voltage Electron Microscopy, Kyoto (1977)* 403-406.
- [11] E. Johnson and P. B. Hirsch, *Phil. Mag. A* 43, No. 1 (1981) 157-170.
- [12] J. S. Robach, I. M. Robertson, B. D. Wirth, and A. Arsenlis, *Phil. Mag.* 83, No. 8 (2003) 955-967.
- [13] M. Kiritani, *Mat. Chem. Phys.* 50 (1997) 133-138.
- [14] S. J. Zinkle and L. L. Snead, *J. Nucl. Mater.* 225 (1995) 123-131.
- [15] M. Victoria, N. Baluc, C. Bailat, Y. Dai, M. I. Luppo, R. Schaublin, and B. N. Singh, *J. Nucl. Mater.* 276 (2000) 114-122.
- [16] N. Ajita, H. Hashimoto, and Y. Takaki, *Phys. Stat. Sol. (a)* 87 (1985) 235-252.
- [17] M. Hiratani, H. M. Zbib, and B. D. Wirth, *Phil. Mag. A* 82, No. 14 (2002) 2709-2735.
- [18] H. Kimura and R. Maddin, *Lattice Defects in Quenched Metals*, Proceedings of an International Conference, Argonne National Laboratory, June 15-17, 1964, Ed., R. Cotterill (New York: Academic Press, 1965) 319-386.
- [19] P. B. Hirsch, *Vacancies '76*, Proceedings of a Conference on Point Defect Behaviour and Diffusional Process, September 13-16, 1976, Ed., R. E. Smallman and J. E. Harris (London: The Metals Society, 1977) 95-107.
- [20] Y. Satoh, H. Taoka, S. Kojima, T. Yoshiie, and M. Kiritani, *Phil. Mag. A* 70, No. 5 (1994) 869-891.
- [21] A. Yoshinaka, Y. Shimomura, M. Kiritani, and S. Yoshida, *Japanese J. Appl. Phys.* 7, No. 7, (1968) 709-714.

- [22] J. Silcox and P. B. Hirsch, *Phil. Mag.* 4 (1959) 72-89.
- [23] M. De Jong and J. S. Koehler, *Phys. Rev.* 129 (1963) 49-61.
- [24] D. Kuhlmann-Wilsdorf, *Acta Met.* 13 (1965) 257-270.
- [25] Y. Matsukawa and S. J. Zinkle, *J. Nucl. Mater.* (2004) in press.
- [26] Y. Matsukawa and S. J. Zinkle, *Dynamic Observation of the Collapse of a Stacking Fault Tetrahedron by Gliding Dislocations.*, *Phil. Mag.*, to be submitted.
- [27] D. Kuhlmann-Wilsdorf, *Acta Met.* 13 (1965) 257-269.
- [28] Y. Matsukawa and S. J. Zinkle, *The Driving Force for the Collapse of a Stacking Fault Tetrahedron due to Intersection by Gliding Dislocations.*, *Phil. Mag.*, to be submitted.

VOID HARDENING IN BCC-IRON STUDIED BY ATOMIC-SCALE MODELLING—
S. I. Golubov, Yu. N. Osetsky, and R. E. Stoller (Oak Ridge National Laboratory)

OBJECTIVE

The objective of this work is atomic-scale modelling of interactions between moving dislocations and particular obstacles. Two different atomic-scale techniques based on (a) a periodic array of dislocations (PAD) and (2) Green's function boundary conditions (GF) in alpha-Fe are used. to elucidate influence the dislocation-image interaction taking place in the case of PAD. Since the PAD and GFBR methods are quite different, they have been applied to the same problem for comparative study. First results of such a study are presented for motion of dislocation in perfect crystal and in crystal containing a row of 2nm spherical voids in bcc Fe.

SUMMARY

Atomic-scale modelling permits detailed simulation of the interactions between moving dislocations and particular obstacles. Such simulations should be of large enough scale to simulate a realistic dislocation density and obstacle spacing, and correctly treat long-range self-interaction between dislocation segments. Results obtained with a 2 nm void and two different atomic-scale techniques based on (1) a periodic array of dislocations (PAD) and (2) Green's function boundary conditions (GF) in alpha-Fe are presented. Static, zero temperature, simulations have been carried out with incrementally increasing strain until dislocation overcomes the obstacle. It is concluded that both techniques reproduce the same critical resolved shear stress (CRSS), and similar void and dislocation modifications are observed.

PROGRESS AND STATUS

Introduction

The crucial role of dislocations in mechanical properties of materials has been successfully shown by continuum elasticity theory. However, understanding the processes that are controlled by atomic scale mechanisms require development of new modelling techniques. The interaction between gliding dislocations and an obstacle in its glide plane is an example of such a process. One of the most successful models [1] is based on a periodic array of dislocations (PAD) using an approach originally proposed by Baskes and Daw. PAD simulates a crystal containing initially straight edge dislocations with periodic boundary conditions along the dislocation line and in the direction of the Burgers vector. The model allows the correct configuration of the dislocation core structure to be simulated and has been successfully applied to study different type of obstacles in bcc and fcc metals (see e.g. [2, 3]). The model is simple and fast, but some limitations arise when compared with results from macro-models based on the "single dislocation in infinite media" approach. These appear because of dislocation-image interaction due to periodic boundary conditions along Burgers vector.

Another model proposed recently [4] employs 3D Green's function boundary relaxation conditions (GFBR) [5]. In this method, flexible GFBC are used along the Burgers vector and perpendicular to the slip plane. Periodicity is maintained along the dislocation line only to enable simulating the mobility of a single dislocation and its interaction with an array of obstacles [4, 6]. The simulation cell consists of three regions: atomistic, Green's function and continuum. In the atomic region atoms are displaced according to Newton's equation of motion. As the atomic region is relaxed, forces build up on atoms in the Green's function region, which cause displacements in all three regions (an efficient method to calculate the elastic displacement field was developed in [7]). Atoms in the first region are relaxed in response to the forces followed again by relaxation of whole crystal via GFBC is reached a stable configuration. This model has been used to calculate the interaction of edge dislocation with voids in bcc tungsten [4]. Since the PAD and GFBR methods are quite different, they have been applied to the same problem for comparative study. First results of such a study are presented for motion of dislocation in perfect crystal and in crystal containing a row of 2nm spherical voids in bcc Fe.

Calculation Details

An edge dislocation with Burgers vector $\frac{1}{2}[111]$ and $\{110\}$ slip plane in bcc-iron was simulated using the many-body interatomic potential of Finnis-Sinclair type parameterized in [8]. The calculations by PAD are carried out in crystals containing $(2-8) \times 10^6$ mobile atoms whereas GFBC were applied in crystals having $\sim(0.2-1.0) \times 10^6$ mobile atoms. The crystal size is varied in the direction of Burgers vector only to test influence the dislocation-image interaction. To simulate motion of the dislocation a shear strain was incrementally increased with a step equal to 10^{-4} . Each increment was followed by relaxation to the minimum potential energy. For the FBC, each strain increment also was followed by up to 8 relaxation steps of the GF boundary layer. Strain was increased until the dislocation moved over a desired distance or overcame the obstacle. In both types of calculation, a stress-strain curve, critical resolved shear stress (CRSS) and dislocation line shape at the CRSS has been obtained and analysed. The both techniques have been applied at $T=0K$.

Results

An example of the stress-strain curves calculated for the case of dislocation glide in perfect crystal, together with the dislocation core displacement, is presented in Fig. 1. As can be seen, the stress-strain curves are the same in linear elastic regime, i.e., before the dislocation moves. When the stress reaches a critical value, i.e., the Peierls stress, the dislocation moves and this motion is different in different models. Thus, in the case of PAD model the dislocation motion depends on dislocation density and obeys the Orowan relationship $\varepsilon = \bar{x}b\rho$. In the case of GFBC, when a single dislocation is simulated in the infinite medium, the dislocation moves continuously until interaction with boundaries compensates applied shear stress. Note that in the case of PAD the Peierls stress is the maximum stress generated in the system (curve 2 in Fig. 1) whereas in the case of GFBC the maximum stress can be infinitely high reflecting the repulsive force between the dislocation and a boundary (curve 1 in Fig. 1a). However, the value of Peierls stress calculated in the both cases is the same ($\tau_p \sim 24MPa$) as well as the critical strain: $\varepsilon_p = 0.033\%$ (GFBC) and 0.035% (PAD).

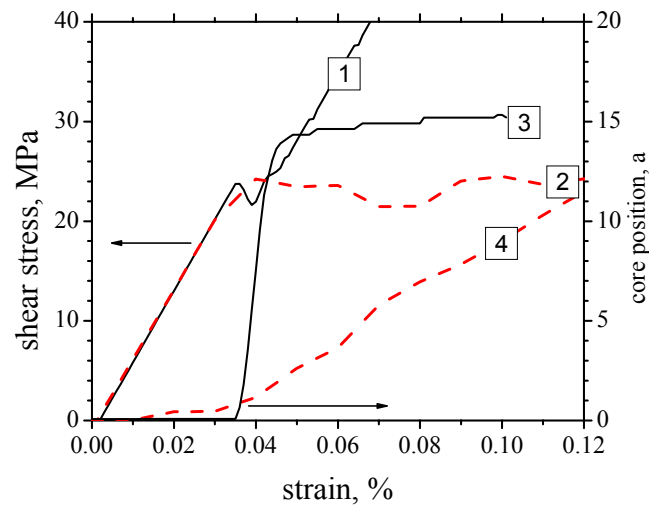


Fig. 1. The stress-strain curves and core positions for the edge dislocation calculated via PAD and GFBC. 1, 2 – stress-strain for GFBC and PAD; 3, 4– core positions for GFBC and PAD.

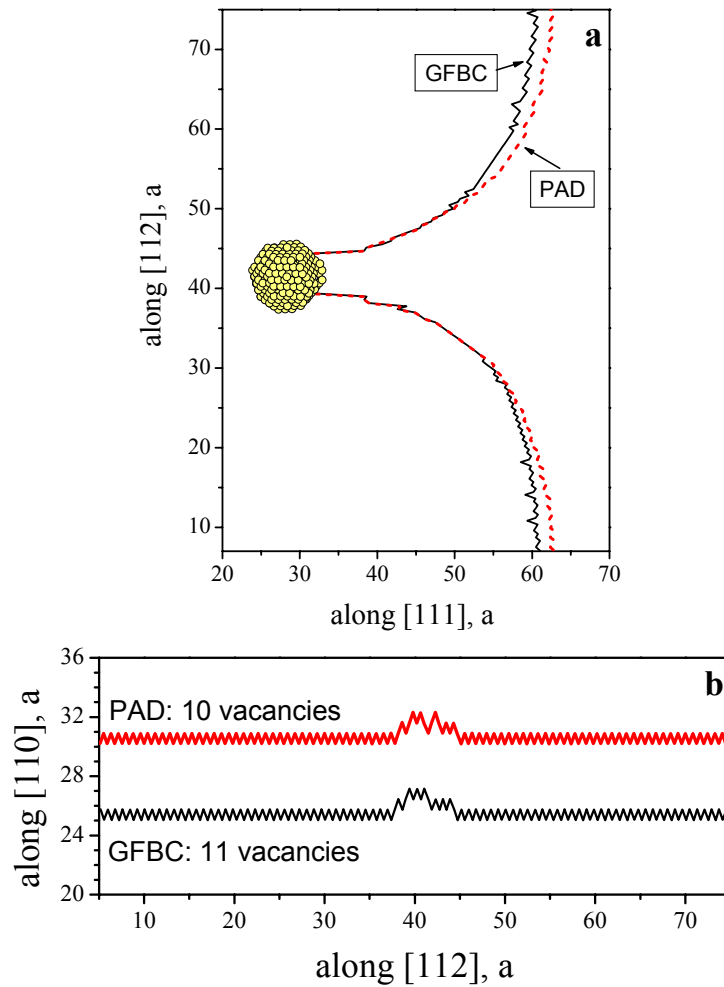


Fig. 2. Comparison of PAD and GFBC calculations for 2nm void at 0K: (a) -dislocation line shape at (b) -critical stress and dislocation climb due to interaction.

In the case of dislocation-void interaction, a full stress-strain curve can be obtained only for the PAD [1, 2]. Therefore, a comparison between the models was made only for the dislocation line shape at the critical condition, i.e., just before it overcomes the obstacle out, and the line shape after the interaction. The former is presented in Fig. 2a where one can see that both lines have very similar shape suggesting that the force distribution related to dislocation-void interaction is also very similar. It was observed earlier that the dislocation absorbs vacancies during the interaction with a void. It is found that in both cases the dislocation absorbs a similar number of vacancies, i.e., 11 for the GFBC and 10 for the PAD, and the shape of superjog created due to climb is also very similar (see Fig. 2b).

Conclusions

Two atomistic-scale techniques, PAD and GFBC, have been used to study dislocation dynamics in perfect crystal and dislocation-void interaction in bcc-Fe. It was found that both techniques lead to similar results: including, the Peierls stress and strain, the dislocation line shape near the void at critical stress and atomic-scale structure of the dislocation line, and void shrinkage after dislocation-void interaction.

References

- [1] Yu. N. Osetsky and D. J. Bacon, *Modelling Simulation Mater. Sci. Eng.* 11 (2003) 427.
- [2] Yu. N. Osetsky, D. J. Bacon, and V. Mohles, *Phil. Mag.* 83, Nos. 31-34 (2003) 3623.
- [3] Yu. N. Osetsky and D. J. Bacon, *J. Nucl. Mater.* 323 (2003) 268.
- [4] Xiangli Liu, S. I. Golubov, C. H. Woo, and Hanchen Huang, *Computer Modelling in Engineering and Sciences* 5 (#6) (2004) 527.
- [5] S. Rao, C. Hernandez, J. P. Simmons, T. A. Parthasarathy, and C. Woodward, *Phil. Mag. A* 77 (1998) 231.
- [6] Xiangli Liu, S. I. Golubov, C. H. Woo, and Hanchen Huang, *Material Science and Engineering A365* (2004) 96.
- [7] S. I. Golubov, Liu Xiangli, Huang Hanchen, and C. H. Woo, *Computer Physics Communications* 137/2 (2001) 312-324.
- [8] G. J. Ackland, D. J. Bacon, A. F. Calder, and T. Harry, *Philos. Mag. A* 71 (1997) 553.

THE INTERACTION OF HELIUM ATOMS WITH EDGE DISLOCATIONS IN α -Fe—H. L. Heinisch, F. Gao, and R. J. Kurtz (Pacific Northwest National Laboratory)

OBJECTIVE

The objective of this work is to quantitatively describe at the atomic level the fate of helium atoms produced in metals and alloys by the neutrons in a fusion reactor.

SUMMARY

Formation energies, binding energies, and the migration of interstitial He atoms at and near the center of an $a/2\langle 111 \rangle\{110\}$ edge dislocation in α -Fe are determined using molecular dynamics and conjugate gradient relaxation methods. Results are compared as a function of the distance of the interstitial He atoms from the center of the dislocation and the amount of excess volume around the dislocation. Interstitial He atoms have negative binding energy on the compression side of the dislocation and strong positive binding energy on the tension side. Even at low temperatures, interstitial He atoms in the vicinity of the dislocation easily migrate to positions near the center of the dislocation, where they form crowdion interstitials with binding energies in excess of 2 eV.

PROGRESS AND STATUS

Introduction

An important first step in mitigating helium effects in fusion reactor materials is to understand the fate of helium with respect to the microstructural features with which it can interact. Molecular statics, molecular dynamics and the dimer method of potential surface mapping are being used to study the fate of helium in the vicinity of dislocations in alpha-iron. We report here on results of conjugate gradient relaxation calculations of formation energies of He atoms in interstitial positions about the dislocation, which are used to map the locations of the most stable configurations of the He atom-dislocation interaction. In addition, some molecular dynamics simulations at 100 K have been performed to study the migration of interstitial He atoms within about 1 nm from the center of the dislocation. The correlation of this information with the spatial distribution of excess volume around the dislocation is also discussed. It is hoped that understanding the He disposition in these simple examples, including the response to excess volume and the effects of dislocation stress fields, will also provide insight and tools for analyzing He disposition in more complicated microstructural environments.

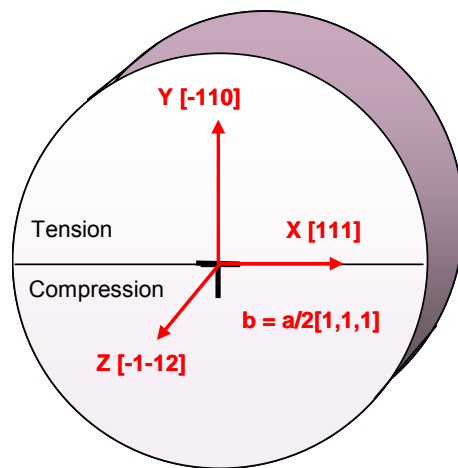
Modeling

An $a/2\langle 111 \rangle\{110\}$ edge dislocation was created along the axis of a cylindrical cell of body-centered cubic Fe atoms by displacing the atoms according to the anisotropic elastic displacement field of the dislocation, then relaxing the entire model. The model is periodic along the dislocation line. One He atom was then placed within the cell, and the cell was again relaxed to determine the He interstitial formation energy and atomic configuration. In all cases the set of interatomic potentials due to Ackland[1], Wilson and Johnson[2], and Beck[3] were used for the Fe-Fe, Fe-He and He-He interactions, respectively. Interstitial formation energies were calculated for He atoms initially at both octahedral and tetrahedral sites at various locations about the dislocation. Relaxation calculations were also performed for an interstitial He atom near the corner of a jog on the dislocation.

Using the same computational cell, molecular dynamics (MD) simulations were performed at a lattice temperature of 100 K for individual interstitial He atoms starting from several different positions about the dislocation for simulated times as long as 8.4 ps. Excess volume in the vicinity of the dislocation was determined using a "Voronoi volume" approach to determine the volumes associated with various interstitial sites, where the volume is centered at the interstitial site.

Results

Figure 1 shows the orientation of the computational cell and the relative positions of the compressive and tensile stress fields of the dislocation. Calculations were performed for He atoms placed at crystallographically equivalent interstitial positions along a line normal to the dislocation slip plane. This was done along a line running through the center of the dislocation (along the y-axis in Fig. 1) as well as along lines parallel to the y-axis at lateral distances from the center. Both octahedral and tetrahedral interstitial sites were examined. In these simulations a He atom in an octahedral interstitial position is slightly more stable than in the tetrahedral interstitial position both in the perfect Fe lattice and in the vicinity of the edge dislocation. However, octahedral interstitial He atoms placed within about 2 Burgers vectors of the dislocation center relax into crowdion interstitial sites along the direction of the Burgers vector, $[111]$, resulting in significant displacements of Fe atoms along the close-packed row.



$a/2[111] [-1-12]$ Edge Dislocation

Fig. 1. Cylindrical computational cell for an $a/2 [111] [-1-12]$ dislocation in α -Fe.

The binding energies of interstitial He atoms to the dislocation are shown in Fig. 2, plotted as a function of their initial unrelaxed positions. The binding energy is the difference between the formation energy of the interstitial He atom in the perfect lattice and in its relaxed position near the dislocation. As expected, the binding energy is negative (repulsive) in the compressive field of the edge dislocation and positive (attractive) in the tensile field. The He atoms that relax to the crowdion interstitial positions have binding energies in excess of about 1-2 eV, depending on their location, while the He atoms placed farther from the dislocation center relax to positions near their original octahedral interstitial sites and have significantly smaller binding energies.

The “reconstruction” of octahedral and tetrahedral interstitial configurations into crowdion configurations takes place as part of the relaxation process, thus no thermal energy is added to the system other than that arising from the artificial creation of the initial unrelaxed configuration. To investigate the role of crowdion formation further, MD simulations at a lattice temperature of 100 K were performed for individual octahedral interstitial He atoms starting at various distances from the dislocation. In Fig. 3 a composite of their individual trajectories is shown. In these cases, octahedral interstitial He atoms beginning well away from the dislocation center migrate to the layer of atoms nearest the slip plane, and become crowdion interstitial defects.

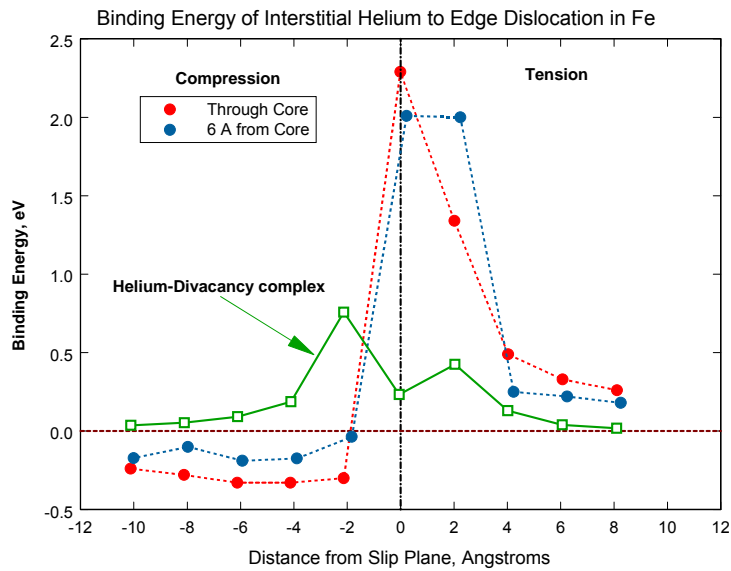


Fig. 2. Binding energies of interstitial He atoms at various positions near the edge dislocation. The green points (boxes) are binding energies for He-divacancy complexes.

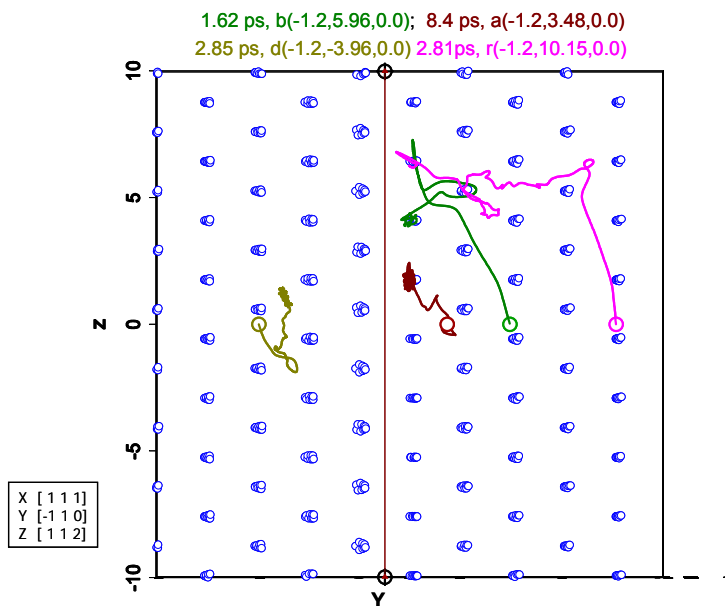


Fig. 3. Trajectories of interstitial He atoms in α -Fe migrating at a temperature of 100 K. The figure is a composite of 4 individual migration simulations. The large circles are starting positions of He atoms and the small blue circles are initial positions of Fe atoms. The vertical line lies along the center of the dislocation. The compression region is to the left of the line. The simulated migration time for each He atom is at the top of the figure.

In each case in Fig. 3 the He interstitials were initially at non-equilibrium positions, so they quickly gained some initial kinetic energy that may have allowed them to more easily migrate short distances to their final positions. On the tension side of the dislocation the He interstitials migrated to crowdion positions in the row of atoms at the slip plane. On the compression side the He atom did not migrate far

before being trapped in an octahedral interstitial location. Simulated times ranged from 1.6 ps to 8.4 ps,, but in all cases the majority of that short time was spent in the final configuration. Quantitative diffusion information for these defects and others will be obtained from long time-high temperature MD simulations and Dimer saddle point energy determinations that are in progress.

Relaxation calculations have also been performed to determine formation and binding energies of He-divacancy complexes near the dislocation. This defect is essentially a divacancy with a He atom trapped in it. Although this complex can be represented in models initially as a substitutional He atom and a neighboring vacancy, when relaxed the He atom prefers to reside at a position that is somewhat off its initial position in the direction of the neighboring vacancy, and it can easily jump to the nearest neighbor vacancy. This complex migrates in a perfect crystal by a mechanism similar to that of single vacancy migration, and the He atom is dragged along, to be described in more detail elsewhere [4]. Figure 2 also contains the binding energies for He-divacancy complexes at various positions around the dislocation, similar to the locations used for the individual interstitial He atoms. Figure 2 shows that the binding energy of the He-divacancy complex to the dislocation is positive on both the compression and tension sides of the dislocation, and it is of significant magnitude only within about 7-8 Å from the center of the dislocation.

Discussion and Conclusions

As expected, interstitial He atoms are attracted to the tension side of the dislocation and repelled from the compression side. He atoms initially in octahedral or tetrahedral interstitial positions within about 2 Burgers vectors of the center of the dislocation on the tension side of the dislocation relax to crowdion positions. Elsewhere around the dislocation and in a perfect Fe crystal He crowdions are not the most stable interstitial configuration.

The formation of stable He crowdions can be associated with excess volume, but the correlation appears to depend on more than just the excess volume in a single interstitial site. Figure 4 shows the He interstitial binding energy as a function of the excess octahedral interstitial volume, where the excess

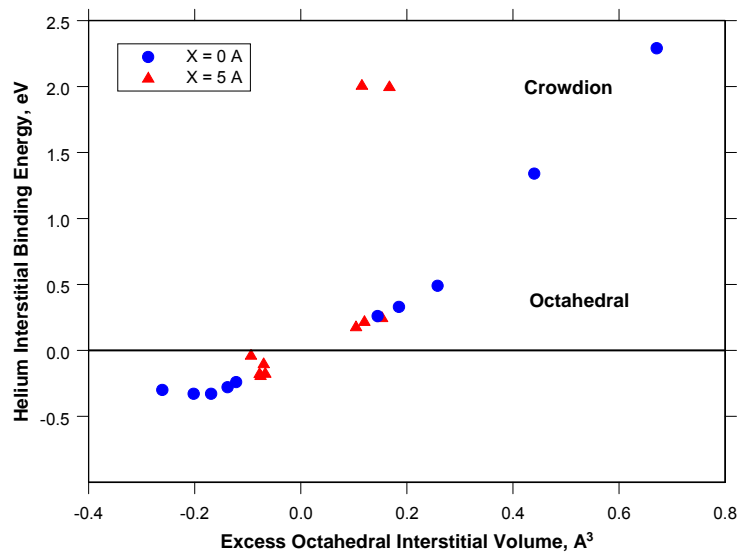


Fig. 4. Helium interstitial binding energy as a function of excess octahedral interstitial volume in α -Fe.

volume is defined as the difference between the volume of the octahedral interstitial site near the dislocation and that at a similar location in the perfect crystal. There is a good correlation between the binding energy and the excess volume for octahedral interstitial positions along a line through the center of the dislocation and normal to the slip plane ($x=0$). With increasing excess volume the binding energy increases, as does the tendency to form crowdion interstitials. However, along a parallel line not through the center ($x=5$ Å) the correlation, if any, is more complicated. Perhaps the “softness” of the lattice configuration surrounding a given interstitial site beyond the nearest neighbor atoms plays a role in the ability to relax to a crowdion. Also, another factor may be that the line along $x=5$ is not on an axis of symmetry of the stress field.

These results indicate that interstitial He atoms are either repelled from or trapped at edge dislocations in α -Fe, depending on the direction of approach. He is trapped as a crowdion with 1-2 eV greater binding energy than as an octahedral interstitial. Thus, it is likely that interstitial He will be strongly trapped at edge dislocations, perhaps forming clusters and bubbles as the He concentration increases. Preliminary results for multiple He interstitials near a dislocation indicate that they can form clusters. Other preliminary results indicate that interstitial He is more strongly bound to jogs than to straight dislocations. Trapped as a crowdion, interstitial He is unlikely to migrate along the edge dislocation by “pipe diffusion.” However, the results in Fig. 2 indicate that the He-divacancy complex defects have much weaker binding to the dislocation than do interstitial He atoms, and they are evidently attracted near the center of the dislocation in both the tension and compression regions of the dislocation stress field. Work is in progress to determine the migration characteristics of He-divacancy complexes in the vicinity of dislocations.

Future Activities

Work is in progress on He interactions with screw dislocations in α -Fe, including He interstitials and He-divacancy complexes. Dimer calculations are in progress to determine He migration mechanisms and saddle point energies in the vicinity of edge and screw dislocations.

References

- [1] G. J. Ackland, D. J. Bacon, A. F. Calder, and T. Harry, *Phil. Mag.* A75 (1997) 713.
- [2] W. D. Wilson and R. D. Johnson, *Interatomic Potential and Simulation of Lattice Defects*, Plenum (1972) 375.
- [3] D. E. Beck, *Mol. Phys.* 14 (1968) 311.
- [4] F. Gao, H. L. Heinisch, and R. J. Kurtz, to be presented at the Second International Conference on Multiscale Materials Modeling, UCLA, Los Angeles, October 11-15, 2004.

**10. DOSIMETRY, DAMAGE PARAMETERS, AND
ACTIVATION CALCULATIONS**

No contributions.

**11. MATERIALS ENGINEERING AND DESIGN
REQUIREMENTS**

No contributions.

12. IRRADIATION FACILITIES AND TEST MATRICES

IRRADIATION START OF MFE-RB-17J EXPERIMENT—D. K. Felde, A. L. Qualls, K. R. Thoms, D. W. Heatherly, R. G. Sitterson, and R. L. Wallace (Oak Ridge National Laboratory)

OBJECTIVE

The objective of this work is to irradiate mostly vanadium alloy specimens in direct contact with lithium at temperatures of 450°C, 600°C and 700°C in a europium-shielded RB position of the High Flux Isotope Reactor (HFIR). Some steel and ceramic specimens are included but are isolated from the primary lithium bath.

SUMMARY

The 17J experiment was installed in a europium-shielded RB* position of HFIR and irradiation began with cycle 400 on April 27, 2004. The capsule temperatures were maintained near the target values with the exception of the lower capsule. An apparent temperature-dependent blockage of the purge gas line limited operation of the lower capsule to ~ 425°C.

PROGRESS AND STATUS

Background

The MFE-RB-17J irradiation experiment was described in an earlier report [1]. Three axially stacked specimen holders are contained within a common inner containment housing, which is itself contained in an outer containment housing tube. The two upper holders are made from the molybdenum alloy TZM and the lower holder is made from stainless steel. The holders are designed to irradiate three sets of metallurgical and ceramic test specimens in lithium baths at 700°C, 600°C and 450°C, in order from top to bottom within the experiment.

The temperatures of the three holders are controlled independently by adjusting the thermal conductivity of the mixtures of inert gases flowing between the holders and the inner housing, which effectively controls the temperature difference from the holder to the inner housing. Gas supply lines can feed helium, neon or argon or a mixture of either helium and neon or helium and argon to the plenums below each of the three holders. Gas from lower holders become part of the mixture for upper holders, so while the temperature of the zones can be independently controlled, they are dynamically coupled.

A helium gas supply line, referred to as a purge line, is routed to the lower holder lower plenum at the base of the inner housing. Helium flows through this line during the experiment passing upward past the specimen holders and out an effluent line open at the top of the inner containment. The purge line remains open at all times and the flow is increased in response to detected off-normal operating conditions while all other gas flows are stopped, guaranteeing that holder temperatures decrease.

Operation

HFIR operating cycle 400 was initiated on April 27, 2004. A plot showing temperatures for the three zones along with reactor power is shown in Fig. 1. A detail of the early part of the cycle is shown in Fig. 2. The initial operation included two reactor startups for operator training purposes along with an approximate 3 hour hold at 10% power associated with neutron scattering experiments. A detailed breakdown of the power history for cycle 400 is provided in Table 1.

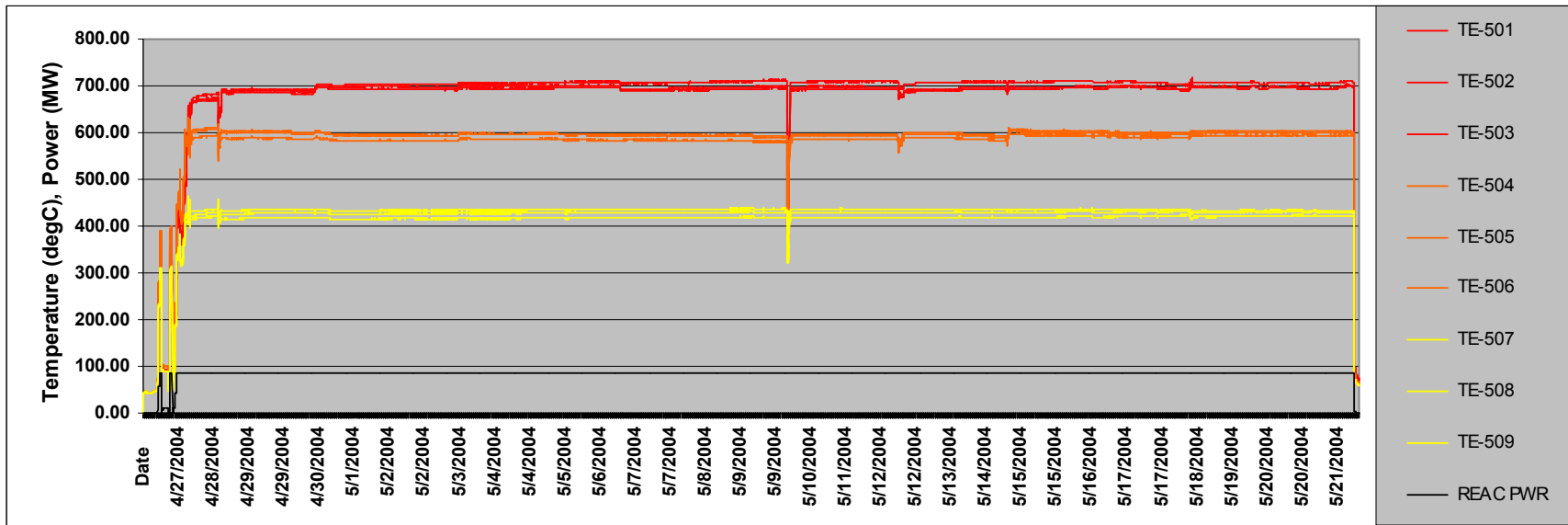


Fig. 1. 17J temperature and power history for HFIR operating cycle 400.

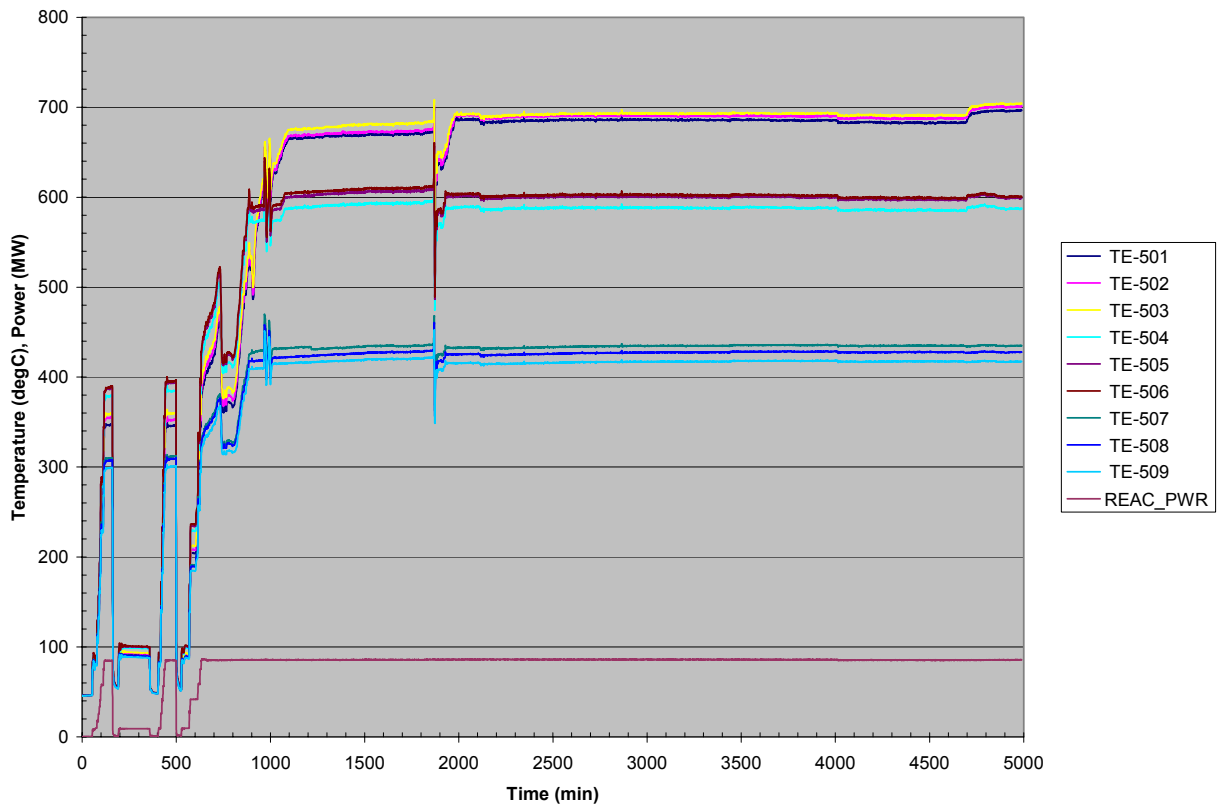


Fig. 2. 17J experiment – startup portion of HFIR operating cycle 400.

The lower thermal conductivity of the helium/argon mix was required in order to reach the desired target temperatures in all three of the capsule regions, with an approximate 70%, 50% and 80% argon concentration in the lower, middle, and upper zones, respectively, at the beginning of the cycle. It was observed during startup that as temperature was increased in the lower zone above $\sim 430^{\circ}\text{C}$ the pressure difference required to flow the helium purge gas to the system increased significantly, eventually causing a decrease in the amount of helium flow when the regulated supply pressure was reached. This reduction in helium led to increasing temperatures in all of the capsules. This occurred in two separate instances as gas flow rate adjustments were made to increase temperatures, one while adjusting flow rate in the helium purge line and the other when increasing argon flow to the same region. These temperature excursions can be seen at ~ 700 and 1800 minutes in Fig. 2. Both occurred within a couple of degrees of the same lower capsule average temperature of 430°C (whereas the middle and upper capsules were at different temperatures for the two cases). This appears to indicate that the purge line has a pinch point that is temperature dependent.

As the control system is currently set up, a Hi Alarm is notification only, with no automatic actions. A Hi-Hi Alarm condition will shut off the argon/neon flow to the control gas lines. An Emergency Cooling temperature set point is reached above the Hi-Hi Alarm condition and shuts off all gas flow to the control gas lines, leaving only helium flow via the purge line. During the first case above, argon flow was manually reduced to cool the system down. During the second case mentioned above, the temperatures reached the Hi-Hi set point and the consequent shut off of argon resulted in the relatively rapid cool down of the capsules.

Table 1. Power history for HFIR operating cycle 400

CYCLE #	Begin time	End time	Elapsed time	Reactor power	Integrated power	COMMENTS	
(days)	(m/d/y hh:mm)	(m/d/y hh:mm)	(hours)	(MW)	(MWD)		
SOC 400	4/27/04 0232	4/27/04 0255	0.4	0.0	0		
	4/27/04 0255	4/27/04 0319	0.4	8.5	0		
	4/27/04 0319	4/27/04 0326	0.1	17.0	0		
	4/27/04 0326	4/27/04 0332	0.1	25.5	0		
	4/27/04 0332	4/27/04 0336	0.1	34.0	0		
	4/27/04 0336	4/27/04 0339	0.0	42.5	1		
	4/27/04 0339	4/27/04 0353	0.2	59.5	1		
	4/27/04 0353	4/27/04 0357	0.1	76.5	1		
	4/27/04 0357	4/27/04 0442	0.8	85.0	4	Dose meas. On HB-4 at Low power	
	4/27/04 0442	4/27/04 0515	0.6	0.0	4		
	4/27/04 0515	4/27/04 0800	2.8	8.5	5		
	4/27/04 0800	4/27/04 0830	0.5	0.0	5		
	4/27/04 0830	4/27/04 0845	0.3	0.0	5		
	4/27/04 0845	4/27/04 0858	0.2	8.5	5	Training	
	4/27/04 0858	4/27/04 0910	0.2	25.5	5		
	4/27/04 0910	4/27/04 0916	0.1	42.5	5		
	4/27/04 0916	4/27/04 0922	0.1	59.5	6		
	4/27/04 0922	4/27/04 0926	0.1	76.5	6		
	4/27/04 0926	4/27/04 1020	0.9	85.0	9		
	4/27/04 1020	4/27/04 1056	0.6	0.0	9		
	4/27/04 1056	4/27/04 1129	0.6	8.5	9	Training	
	4/27/04 1129	4/27/04 1132	0.0	25.5	9		
	4/27/04 1132	4/27/04 1214	0.7	42.5	11		
	4/27/04 1214	4/27/04 1226	0.2	59.5	11		
	4/27/04 1226	4/27/04 1231	0.1	76.5	11	4/27/2004 22:35	
	4/27/04 1231	5/21/04 1735	581.1	85.0	2069	23.79166667	
	EOC 400	5/21/04 1735	6/16/04 1200	618.4			

One other temperature transient can be seen on the plot in Fig. 1. A Watchdog Timer alarm that monitors communication within the control system was received and resulted in initiation of the Emergency Cooling mode. The alarm was apparently caused by some power switching work being done for the ORNL site. With helium only, the zone temperatures dropped to the 300-400 C range. The system was reset and temperatures were back up to near operating level within ~1 hour of the transient.

The lower capsule operating temperature was lowered to ~425 °C in order to avoid the transient conditions caused by the blocked flow. The apparent temperature-dependent blockage of the control gas line is not repairable, and a decision was made to operate at this lower temperature for the remainder of the follow-on cycles as well.

After the completion of cycle 400, the purge line and control gas line supplying the lower zone were switched at the control cabinet. This will result in blockage of argon to the zone as temperature increases, rather than helium.

References

- [1] A. L. Qualls et al., Fusion Materials Semiannual Progress Report for Period Ending December 31, 2003, DOE/ER-0313/35, U.S. Department of Energy, 242-249.

ASSEMBLY OF THE US-JAPAN JP-27 EXPERIMENT AND START OF IRRADIATION IN THE HFIR—
D. K. Felde, K. R. Thoms, D. W. Heatherly, S. H. Kim, R. G. Sitterson, and R. E. Stoller (Oak Ridge National Laboratory) and H. Tanigawa (Japan Atomic Energy Research Institute, Tokai, Japan)

OBJECTIVE

This work is being carried out under Annex I of the Collaboration on Fusion Materials between the U.S. DOE and the Japan Atomic Energy Research Institute. The JP-27 experiment is one component of the Phase-IV experiments with the goal of elucidating the effects of helium in candidate engineering and model alloys and verifying the irradiation response of alloy F82H.

SUMMARY

Specimen and capsule parts fabrication for JP-27 was completed. Loading of specimens into specimen holders and assembly of the capsule was completed. The experiment was installed in the target region of HFIR and irradiation began with cycle 400, starting April 27, 2004.

PROGRESS AND STATUS

Introduction

This experiment is being carried out within the framework of the US DOE-JAERI Collaboration on Fusion Materials, Annex I, which is in its fourth phase. The goals of the experiment include the investigation of the effects of helium on microstructural evolution, the impact of helium on fracture properties, and the development of engineering data on the fusion candidate alloy F82H. The goal of this report is to provide a detailed description of the final design of the JP-27 capsule and a detailed list of specimens loaded into JP-27.

Description of JP-27 Capsule

The JP-27 capsule includes 16 specimen holders designed to accommodate 6 types of specimens and irradiate them at 3 temperatures, 300, 400, and 500°C. The specimen types are a small bend bar (deformation-fracture mini-beam, DFMB), a sheet tensile specimen (SS-J3), a subsized pre-cracked Charpy V-notch specimen (M3-PCCVN), transmission electron microscopy disks (TEM), atom probe specimens (APFIM), and small multi-purpose coupons (MMPC) that have the same overall dimensions as the APFIM specimens.

An overall layout of the JP-27 experiment is shown in Table 1, which provides the subcapsule position number, the specimen type being irradiated in that position, the design irradiation temperature, and the distance that the center of the subcapsule is from the HFIR horizontal mid-plane (HMP).

Each of the specimen holders is fabricated from oxide dispersion strengthened aluminum (DISPAL). The outside diameters of the specimen holders are sized to provide a precise helium-filled gas gap between the holder and the capsule housing tube necessary to achieve the desired irradiation temperature. Centering tabs, six at each end, are machined into the holders to help assure uniform gas gaps. The inner part of the specimen holder is machined to accommodate the type of specimens being irradiated, and therefore each has a unique geometry. Silicon carbide (SiC) passive temperature monitors are included in each specimen holder. These will be analyzed after irradiation to determine actual irradiation temperature.

Table 1. Layout of the JP-27 experiment

Position number	Specimen type	Design temp. (°C)	Distance above HMP* (in.)
1	TEM	400	9.487
2	M3-PCCVN	300	8.357
3	M3-PCCVN	300	6.783
4	SS-J3	300	5.287
5	SS-J3	400	3.869
6	SS-J3	400	2.451
7	M3-PCCVN	400	0.955
8	TEM	500	-0.175
9	DFMB	500	-0.958
10	DFMB	400	-1.838
11	M3-PCCVN	400	-3.065
12	DFMB	300	-4.292
13	M3-PCCVN	300	-5.519
14	SS-J3	300	-7.015
15	SS-J3	300	-8.433
16	TEM	300	-9.485

* HMP – Horizontal Mid-plane.

A top view and axial cross section of the specimen holders used to irradiate TEM specimens (positions 1, 8, and 16) is shown in Fig. 1 (all dimensions in Figs. 1 through 4 are in inches unless otherwise noted). A total of 100 (0.010 in. thick) specimens can be accommodated in these holders, along with a single SiC temperature monitor located at the center of the holder. To help identify in which hole the specimens are located, a 0.040-in. diameter by 0.040-in. deep hole was drilled in the top of each TEM holder, and the specimen holes are then numbered clockwise starting at this 0.040-in. hole.

The loading configuration for the tensile specimen holders is shown in Fig. 2. Eight SS-J3 tensile and eight APFIM specimens can be accommodated per layer, with two layers per holder. Six holders are located at positions 4, 5, 6, 14, and 15, each with a total of 16 tensile and APFIM specimens. A spring pin is placed in the center of the specimen array to apply pressure to the SiC temperature monitors and, in turn, on the tensile specimens to assure good thermal contact with the specimen holder. At each corner two APFIM “tuning fork” specimens are loaded with a corrugated spring to assure that they are also in good thermal contact with the holder. In some of the tensile specimen holders, two multi-purpose coupons (MMPC) and spacers that combined have the same overall dimensions as the APFIM specimens were substituted for the APFIM specimens (see loading list).

Subsized pre-cracked Charpy V-notch specimens (M3-PCCVN) are loaded into specimen holders shown in Fig. 3. Each of these holders (positions 2, 3, 7, 11, and 13) has a total of 8 specimens. Two SiC temperature monitors and corrugated springs are placed in the center of the specimen array to assure good thermal contact with the holder.

The DFMB specimens are loaded into three holders (positions 9, 10, and 12) as shown in Fig. 4. There are two layers of specimens with 16 specimens at each level. The outer row of each layer is made up of 12 specimens that are 1.68 mm square, while the inner four specimens are either 0.40 x 3.3 mm or 0.890 x 3.3 mm. A SiC temperature monitor and a corrugated spring are placed in the center of the specimen array, and two corrugated springs are placed in two of the outer rows to assure all specimens are in good thermal contact with the holder. Specimen locations are designated by a C, S, TM, M1 or M2, to more precisely identify loading locations (see loading list).

Specimen Loading

The location of each of the nearly 600 specimens in JP-27 is reported in Table 2, which contains a box for each of the 16 specimen holders and 5 dosimeter positions. Because coatings applied to some of the TEM discs required the discs to be loaded in a prescribed manner, the boxes for the TEM specimen holders (positions 1, 8, and 16) have a column labeled "Engr. Face" to indicate which way the engraved face of the specimen was loaded. A total of five neutron dosimeter packages provided by PNNL were loaded into JP-27, one each between positions 1 and 2, 3 and 4, 7 and 8, 12 and 13, and below position 16. The M3-PCCVN specimens (in positions 2, 3, 7, 11, and 13) were all loaded with the notches facing towards the center of the holders. The outer rows of specimens in the DFMB holders (positions 9, 10, and 12) were loaded with the notches facing outward toward the holder, while the inner four specimens were loaded with their notches facing inward toward the center of the holder.

FUTURE WORK

The JP-27 capsule will be irradiated to a peak fluence of 25 dpa, which will take approximately 13 HFIR cycles.

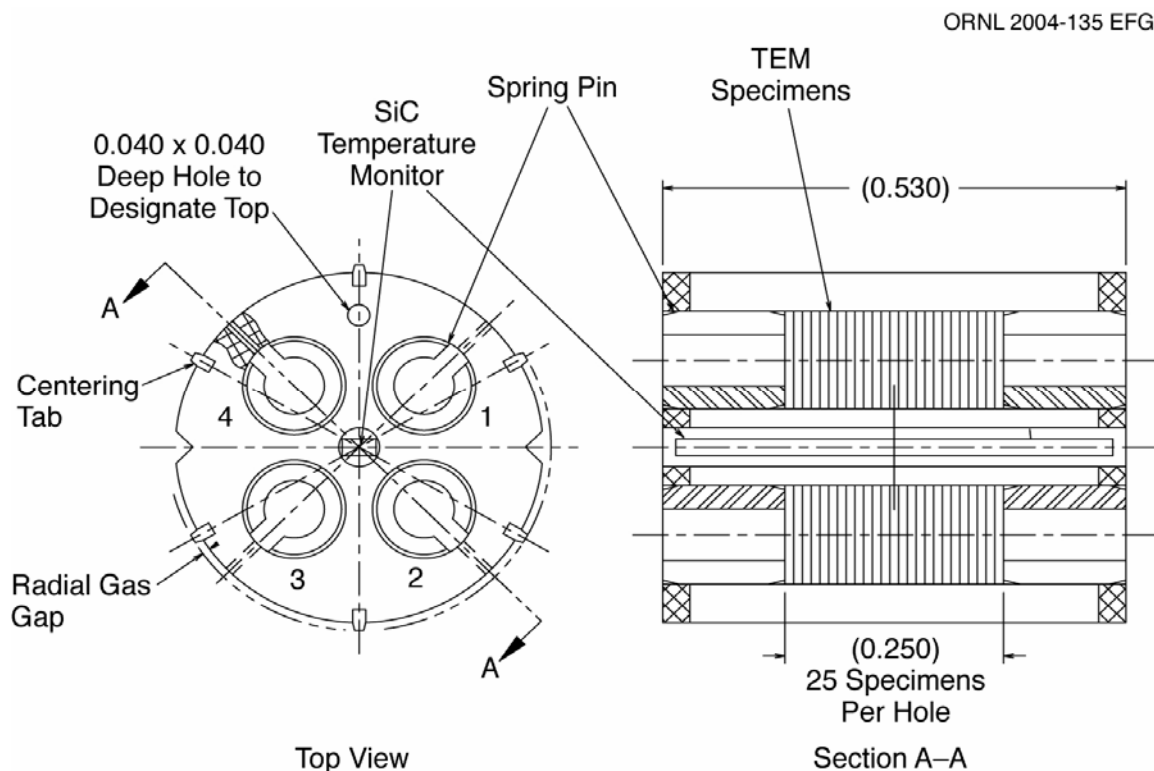


Fig. 1. Specimen holder subassembly used in JP-27 for TEM specimens.

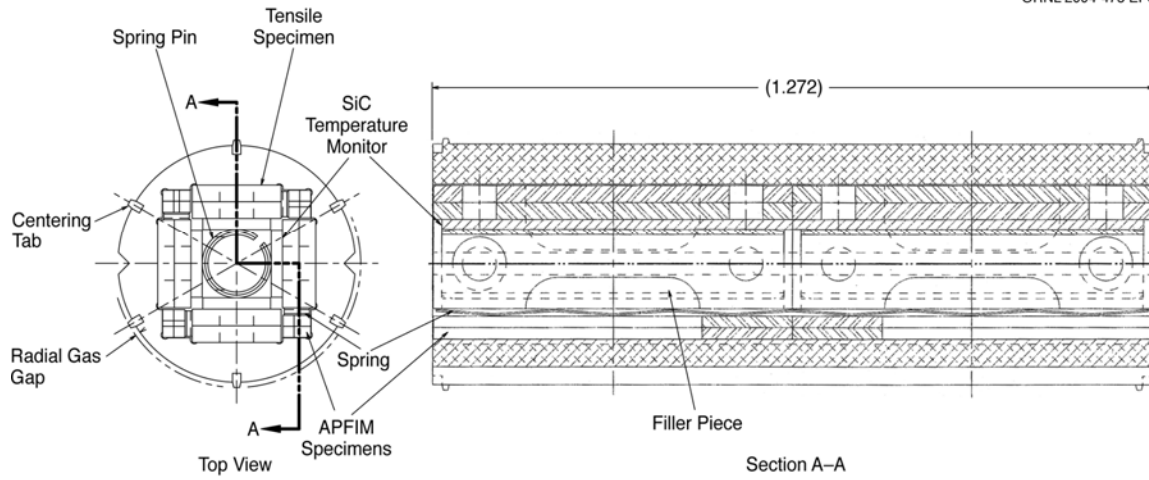


Fig. 2. Specimen holder subassembly used in JP-27 for SS-J3 tensile and APFIM specimens.

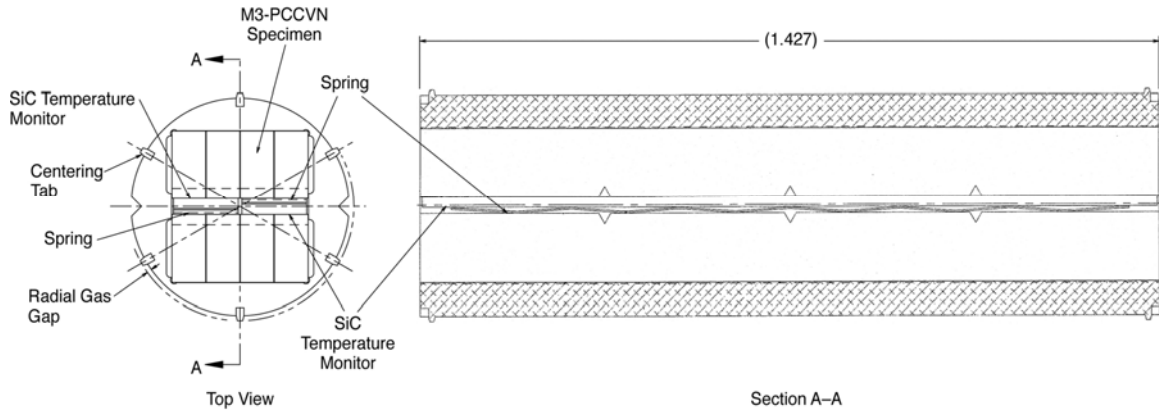


Fig. 3. Specimen holder subassembly used in JP-27 for M3-PCCVN specimens.

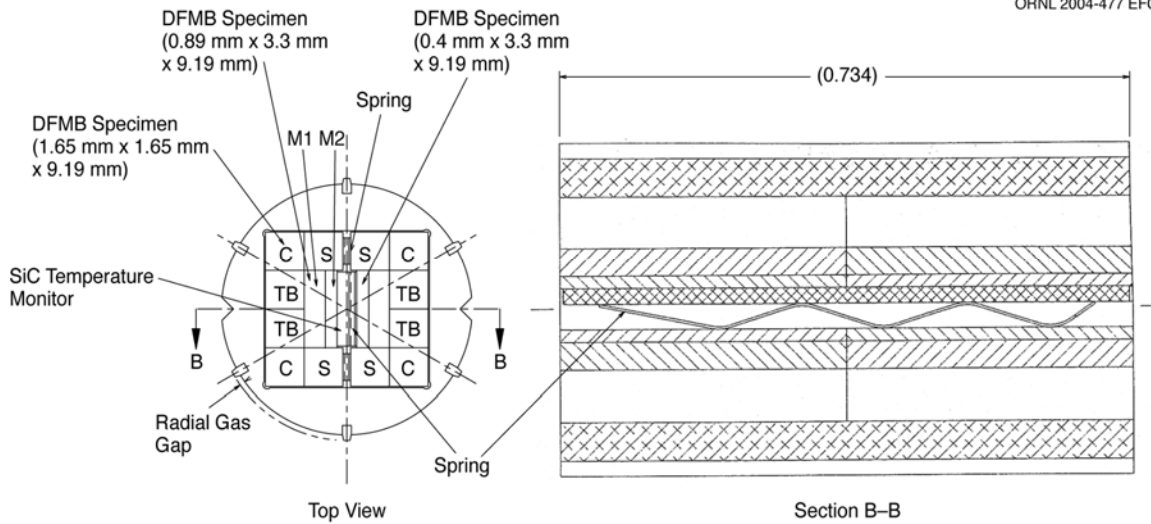


Fig. 4. Specimen holder subassembly used in JP-27 for DFMB specimens.

Table 2. JP-27 specimen and dosimetry loading list

POS. 1 JP-27	TEM specimen numbers									Passive thermometry in center hole
		Hole No.1*	Engr. face	Hole No.2*	Engr. face	Hole No.3*	Engr. face	Hole No.4*	Engr. face	
BOTTOM	1	046	Down	ZQ43	Down	042	Down	H41	Up	Ser. # 1
	2	ZA45	Up	ZK43	Up	ZA42	Up	UN40	Up	
	3	057	Down	ZH43	Down	043	Down	UN41	Up	
	4	ZF46	Up	ZK44	Up	ZF42	Up	340	Up	
	5	H46	Down	ZR46	Down	H42	Down	341	Up	
	6	ZF47	Up	ZN42	Up	ZF43	Up	R40	Up	
	7	H47	Down	ZR45	Down	H43	Down	R41	Up	
	8	UN46	Up	ZN43	Up	UN42	Up	ZG40	Up	
	9	R46	Down	044	Down	R42	Down	ZG41	Up	
	10	UN47	Up	ZA43	Up	UN43	Up	ZH40	Up	
	11	R47	Down	H44	Down	R43	Down	ZH41	Up	
	12	ZH44=	Up	ZA44	Up	ZP42	Up	ZJ40	Up	
	13	ZG42	Down	H45	Down	H58	Up	ZJ41	Up	
	14	ZP43	Up	ZF44	Up	ZB41	Up	ZK40	Up	
	15	ZG43	Down	R44	Down	ZC40	Up	ZK41	Up	
	16	ZH34+	Up	ZF45	Up	ZC41	Up	ZN40	Up	
	17	ZQ54	Down	R45	Down	ZD40	Up	ZN41	Up	
	18	ZJ42	Up	045	Up	ZD41	Up	ZS40	Up	
	19	ZS42	Down	ZR43	Down	ZE40	Up	ZS41	Up	
	20	ZJ43	Up	UN44	Up	ZE41	Up	ZQ40	Up	
	21	ZS43	Down	ZR44	Down	ZF40	Up	ZQ41	Up	
	22	ZJ44	Up	UN45	Up	ZF41	Up	ZP40	Up	
	23	ZQ42	Down	ZA40	Up	040	Up	ZP41	Up	
	24	ZK42	Up	ZA41	Up	041	Up	ZR40	Up	
	25			ZB40	Up	H40	Up	ZR41	Up	
26										
27										
28										
29										
30										
31										
TOP										

The spacer between positions number 1 and 2 contains Neutron Dosimeter Number 0

POS. 2 JP-27	M3-PCCVN specimen	Passive thermometry	
	1. outer XE34	1. Ser. #1	2. Ser. #2
	2. inner XE35		
	3. inner XE36		
	4. outer XF34		
	5. outer XF35		
	6. inner XG34		
	7. inner XG35		
8. outer XG36			
POS. 3 JP-27	M3-PCCVN specimen	Passive thermometry	
	1. outer XF36	1. Ser. #3	2. Ser. #4
	2. inner 534		
	3. inner 535		
	4. outer 634		
	5. outer 635		
	6. inner XH34		
	7. inner 536		
8. outer 636			

The spacer between positions number 3 and 4 contains Neutron Dosimeter Number V

POS. 4 JP-27	SS-J3 tensile specimen	APFIM specimen	Passive thermometry
	1. inner 531	1. 53A	1. Ser. #1
	2. outer 530	2. 53B	
	3. inner 532	3. 53C	2. Ser. #2
	4. outer 533	4. 53D	
	5. inner 031	5. 03A	3. Ser. #3
	6. outer 030	6. 03B	
	7. inner 032	7. 03C	4. Ser. #4
8. outer 033	8. 03D		
Bottom half	SS-J3 tensile specimen	APFIM specimen	Passive thermometry
	9. inner 631	9. 63A	5. Ser. #5
	10. outer 630	10. 63B	
	11. inner 632	11. 63C	6. Ser. #6
	12. outer 633	12. 63D	
	13. inner H31	13. H38	7. Ser. #7
	14. outer H30	14. H39	
	15. inner H32	15. H3A	8. Ser. #8
16. outer H33	16. H3B		

POS. 5 JP-27 Top half	SS-J3 tensile specimen	APFIM specimen	Passive thermometry
	1. inner UA17	1. R44	1. Ser. #9
	2. outer UA16	2. R45	
	3. inner R40	3. 340	2. Ser. #10
	4. outer R41	4. 341	
	5. inner XE41	5. ZQ44	3. Ser. #11
	6. outer XE40	6. ZQ45	
	7. inner XE42	7. ZQ46	4. Ser. #12
8. outer XG40	8. ZQ47		
Bottom half	SS-J3 tensile specimen	APFIM specimen	Passive thermometry
	9. inner ZP41	9. ZP42	5. Ser. #13
	10. outer ZP40	10. ZP43	
	11. inner XQ40	11. ZQ42	6. Ser. #14
	12. outer ZQ41	12. ZQ43	
	13. inner XF41	13. ZQ48	7. Ser. #15
	14. outer XF40	14. ZQ49	
	15. inner XF42	15. ZQ4A	8. Ser. #16
16. outer XG41	16. ZQ4B		
POS. 6 JP-27 Top half	SS-J3 tensile specimen	APFIM specimen	Passive thermometry
	1. inner 541	1. 54B	1. Ser. #17
	2. outer 540	2. 54C	
	3. inner 542	3. 54D	2. Ser. #18
	4. outer 543	4. 54E	
	5. inner 041	5. 04A	3. Ser. #19
	6. outer 040	6. 04B	
	7. inner 042	7. 04C	4. Ser. #20
8. outer 043	8. 04D		
Bottom half	SS-J3 tensile specimen	APFIM specimen	Passive thermometry
	9. inner 641	9. 64B	5. Ser. #21
	10. outer 640	10. 64C	
	11. inner 642	11. 64D	6. Ser. #22
	12. outer 643	12. 64E	
	13. inner H41	13. H49	7. Ser. #23
	14. outer H40	14. H4A	
	15. inner H42	15. H4B	8. Ser. #24
16. outer H43	16. H4C		

POS. 9 JP-27	Outer layer DFMB specimens (.065 x .065 x .362 in)												Inner layer DFMB (.0157x .130 x .362 in)		Inner layer DFMB (.035 x .130 x .362 in)		Passive therm.
	C	C	C	C	S	S	S	S	TB	TB	TB	TB	M2	M2	M1	M1	
Row 1 TOP	1	2	3	4	5	6	7	8	9	10	11	12	1	2	3	4	1. Ser. #1
	050a	050b	050c	050d	550a	550b	550c	550d	650a	650b	650c	650d	051	H50	R50	R51	
Row 2 BOTTOM	050e	050f	050g	050h	550e	550f	550g	550h	650e	650f	650g	650h	551	651	552	652	

POS. 10 JP-27	Outer layer DFMB specimens (.065 x .065 x .362)												Inner layer DFMB (.0157x .130 x .362 in)		Inner layer DFMB (.035 x .130 x .362 in)		Passive therm.
	C	C	C	C	S	S	S	S	TB	TB	TB	TB	M2	M2	M1	M1	
Row 1 TOP	1	2	3	4	5	6	7	8	9	10	11	12	1	2	3	4	Ser. #2
	048a	048b	048c	048d	548a	548b	548c	548d	648a	648b	648c	648d	049	H48	R42	R43	
Row 2 BOTTOM	048f	048f	048g	048h	548e	548f	548g	548h	648e	648f	648g	648h	549	649	54A	64A	

POS. 11 JP-27	M3-PCCVN specimen				Passive thermometry			
	1. outer	544			1.	Ser. #7	2.	Ser. #8
	2. inner	644						
	3. inner	645						
	4. outer	547						
	5. outer	545						
	6. inner	647						
	7. inner	646						
8. outer	546							

POS. 12 JP-27	Outer layer DFMB specimens (.065 x .065 x .362)												Inner layer DFMB (.0157x .130 x .362 in)		Inner layer DFMB (.035 x .130 x .362 in)		Passive therm.
	C	C	C	C	S	S	S	S	TB	TB	TB	TB	M2	M2	M1	M1	
Row 1 TOP	1	2	3	4	5	6	7	8	9	10	11	12	1	2	3	4	1. Ser. #3
Row 2 BOTTOM	038a	038b	038c	038d	537a	537b	537c	537d	637a	637b	637c	637d	R32	R33	039	H37	

The spacer between positions number 12 and 13 contains Neutron Dosimeter Number S

POS. 13 JP-27	M3-PCCVN specimen				Passive thermometry			
	1. outer	034			1.	Ser. #9	2.	Ser. #10
	2. inner	H34						
	3. inner	XH35						
	4. outer	037						
	5. outer	035						
	6. inner	H35						
	7. inner	H36						
8. outer	036							

POS. 14 JP-27 Top half	SS-J3 tensile specimen	APFIM specimen	Passive thermometry
	1. inner XH31	1. 330	1. Ser. #25
	2. outer XH30	2. 331	
	3. inner XH32	3. 332	2. Ser. #26
	4. outer XH33	4. 333	
	5. inner XF31	5. 334	3. Ser. #27
	6. outer XF30	6. 335	
	7. inner XF32	7. 336	4. Ser. #28
8. outer XF33	8. 337		
Bottom half	SS-J3 tensile specimen	APFIM specimen	Passive thermometry
	9. inner UA15	9. R34	5. Ser. #29
	10. outer UA14	10. R35	
	11. inner R30	11. R36	6. Ser. #30
	12. outer R31	12. R37	
	13. inner Q31	13. R38	7. Ser. #31
	14. outer Q30	14. R39	
	15. inner Q32	15. 338	8. Ser. #32
16. outer Q33	16. 339		
POS. 15 JP-27 Top half	SS-J3 tensile specimen	APFIM specimen	Passive thermometry
	1. inner XE31	1. R3A	1. Ser. #33
	2. outer XE30	2. R3B	
	3. inner XE32	3. R3C	2. Ser. #34
	4. outer XE33	4. R3D	
	5. inner XG31	5. ZQ34	3. Ser. #35
	6. outer XG30	6. ZQ35	
	7. inner XG32	7. ZQ36	4. Ser. #36
8. outer XG 33	8. ZQ37		
Bottom half	SS-J3 tensile specimen	APFIM specimen	Passive thermometry
	9. inner ZP31	9. ZP32	5. Ser. #37
	10. outer ZP30	10. ZP33	
	11. inner ZQ30	11. ZQ32	6. Ser. #38
	12. outer ZQ31	12. ZQ33	
	13. inner XJ31	13. ZQ38	7. Ser. #39
	14. outer XJ30	14. ZQ39	
	15. inner XJ32	15. ZA3A	8. Ser. #40
16. outer XJ33	16. ZQ3B		

POS. 16 JP-27		TEM specimen numbers								Passive thermometry in center hole
		Hole No.1*	Engr. face	Hole No.2*	Engr. face	Hole No.3*	Engr. face	Hole No.4*	Engr. face	
BOTTOM	1	036	Down	ZG34	Down	032	Down	H31	Up	Ser. #3
	2	ZA35	Up	ZK33	Up	ZA32	Up	UN30	Up	
	3	037	Down	ZH33	Down	033	Down	UN31	Up	
	4	ZF36	Up	ZK34	Up	ZF32	Up	330	Up	
	5	ZR36	Down	ZH44+	Down	H32	Down	331	Up	
	6	ZF37	Up	ZN32	Up	ZF33	Up	R30	Up	
	7	H37	Down	ZR35	Down	H33	Down	R31	Up	
	8	UN36	Up	ZN33	Up	UN32	Up	ZG30	Up	
	9	R36	Down	034	Down	R32	Down	ZG31	Up	
	10	UN37	Up	ZA33	Up	UN33	Up	ZH30	Up	
	11	R37	Down	H34	Down	R33	Down	ZH31	Up	
	12	ZH34=	Up	ZA3A	Up	ZP32	Up	ZJ30	Up	
	13	ZG32	Down	H35	Down	ZR32	Up	ZJ31	Up	
	14	ZP33	Up	ZF34	Up	ZB31	Up	ZK30	Up	
	15	ZG33	Down	R34	Down	ZC30	Up	ZK31	Up	
	16	ZP34	Up	ZF35	Up	ZC31	Up	ZN30	Up	
	17	ZQ33	Down	R35	Down	ZD30	Up	ZN31	Up	
	18	ZJ32	Up	035	Up	ZD31	Up	ZS30	Up	
	19	ZS32	Down	ZR33	Down	ZE30	Up	ZS31	Up	
	20	ZJ33	Up	UN34	Up	ZE31	Up	ZQ30	Up	
	21	ZS33	Down	ZR34	Down	ZF30	Up	ZQ31	Up	
	22	ZJ34	Up	UN35	Up	ZF31	Up	ZP30	Up	
	23	ZQ32	Down	ZA30	Up	030	Up	ZP31	Up	
	24	ZK32	Up	ZA31	Up	031	Up	ZR30	Up	
	25	H36	Down	ZB30	Up	H30	Up	ZR31	Up	
TOP	26									
	27									
	28									
	29									
	30									
	31									

The spacer at the bottom of position number 16 contains Neutron Dosimeter Number

7